HARVARD UNIVERSITY
Graduate School of Arts and Sciences

DISSERTATION ACCEPTANCE CERTIFICATE

The undersigned, appointed by the

Department of Earth and Planetary Sciences

have examined a dissertation entitled

"Quantifying tropospheric OH concentrations and coal methane emissions using remote sensing"

presented by Elizabeth Penn

candidate for the degree of Doctor of Philosophy and hereby
certify that it is worthy of acceptance.

Signature _____

Typed name: Prof. Daniel Jacob

Signature _____

Typed name: Prof. Steve Wofsy

Signature _____

Typed name: Prof. Zhiming Kuang

Signature _____

Typed name: Prof. Elsie Sunderland

Date: April 10, 2025

Quantifying tropospheric OH concentrations and coal methane emissions using remote sensing

A dissertation presented

by

Elizabeth Penn

to

The Department of Earth and Planetary Sciences

in partial fulfillment of the requirements

for the degree of

Doctor of Philosophy

in the subject of

Earth and Planetary Sciences

Harvard University

Cambridge, Massachusetts

April 2025

Quantifying tropospheric OH concentrations and coal methane emissions using remote sensing

Abstract

This thesis is divided into two parts. In Chapter 1, I use an analytical Bayesian inversion framework to show what we can (and cannot) learn from Thermal Infrared (TIR) and Shortwave Infrared (SWIR) satellite observations of methane. In Chapter 2, I demonstrate how to develop national coal-mine methane inventories with aircraft campaigns using high-resolution hyperspectral instruments, with a view towards recently-launched hyperspectral satellite constellations. An abstract for each chapter follows.

Chapter 1. The hydroxyl radical (OH) is the main oxidant in the troposphere and controls the lifetime of many atmospheric pollutants including methane. Global annual mean tropospheric OH concentrations ($[\overline{OH}]$) have been inferred since the late 1970s using the methyl chloroform (MCF) proxy. However, concentrations of MCF are now approaching the detection limit, and a replacement proxy is urgently needed. Previous inversions of GOSAT satellite measurements of methane in the SWIR have shown success in quantifying $[\overline{OH}]$ independently of methane emissions, and observing system simulations have suggested that TIR measurements may provide additional constraints on OH. Here we combine TIR satellite observations of methane from AIRS with SWIR observations from GOSAT in a three-year (2013-2015) analytical Bayesian inversion optimizing both methane emissions and OH concentrations. We examine how much information can be achieved on the interannual, seasonal, and latitudinal features of the OH distribution using information from MCF data as well as the ACCMIP ensemble of global atmospheric chemistry models to construct a full prior error covariance matrix for OH concentrations for use in the inversion. This is

essential to avoid overfit to observations. Our results show that GOSAT alone is sufficient to quantify $[\overline{OH}]$ and its interannual variability independently of methane emissions, and that AIRS adds little information. The ability to constrain the latitudinal variability of OH is limited by strong error correlations. There is no information on OH at mid-latitudes, but there is some information on the NH/SH interhemispheric ratio, showing this ratio to be lower than currently simulated in models. There is also some information on the seasonal variation of OH concentrations, though it mainly confirms that simulated by models. Future satellite observations of methane will continue to improve our understanding of methane emissions and consequently $[\overline{OH}]$ and its interannual variability.

Chapter 2. Underground coal mines are important global sources of methane but emission estimates are uncertain. Emission estimates for individual mines from Carbon Mapper aircraft remote sensing surveys in the U.S. agree within 20% with direct measurements used for national emission reporting (IPCC Tier 3 estimate). Such direct measurements are unavailable in most countries, which rely on estimated emission factors (EFs) applied to coal production rates. We find that EFs from IPCC Tier 1 and Model for Calculating Coal Mine Methane (MC2M) methods would overestimate U.S. emissions threefold due to incorrect dependence on mine depth. An IPCC Tier 2 method using measured basin-specific mine gas content agrees with direct emission measurements but does not account for gob well emissions and requires gas content data that are generally unavailable. We show that limited Carbon Mapper surveys successfully estimate basin-specific EFs for ventilation shafts and gob wells, enabling estimates of basin- and national-scale emissions.

Contents

List of Tables

List of Figures

Acknowledgments

It is a common joke among academics that Ph.D. students defending their theses acknowledge absolutely everyone. "To my parents, my friends, my elementary school teacher, and my pet ferret," a satirical acknowledgment might read. That's precisely what I set out to do here.

Because while it is perhaps true that students are gratuitous in their acknowledgments, it is also true that no person achieves a Ph.D. on their own. It requires the support of countless family, friends—and yes—elementary school teachers over nearly three decades of life. It is a tremendous privilege to spend 6 years studying some small corner of the universe, one afforded to only a tiny fraction of the population. Here are the people who made it happen for me.

My mentors. In particular to my Ph.D. advisor, Daniel J. Jacob, who taught me to think like a scientist, and my undergraduate advisor from the University of Wisconsin, Tracey Holloway, who continues to challenge my worldview. Thanks also to Jennifer Newman, Larry Horowitz, Vaishali Naik, and Loretta Mickley. And special thanks to Dan Cusworth and Zichong Chen, who, while not formal mentors, have provided me with unparalleled advice every day.

My collaborators, without whom this work would not have happened: James D. East, Melissa P. Sulprizio, Lori Bruhwiler, Joannes D. Maasakkers, Hannah Nesser, Zhen Qu, Yuzhong Zhang, John Worden, Kate Howell, Kelly O'Neill, Tia Scarpelli, Robert A. Field, C. Özgen Karacan, Elfie Roy.

My team at Tesla, from whom I learned nearly as much as I did in my time at Harvard: Karen Yu, Paul Deng, Adi Garg, Yutian Lei, Harshil Dadlani, Yari Lazzaro, Lisa Jiang, David Oh, and Li Zhang.

The Carbon Mapper science team, who let me work on something exciting: Dan Bon, Tia Scarpelli, Kate Howell, Kelly O'Neill, Patrick Sullivan, Deja Newton, Ralph Jiorle, Jinsol Kim, Pavel Dorovksoy, and Riley Duren.

My officemates and friends. Hannah Nesser, who taught me to teach, and who has

always been there where I need to vent. Ellie Beaudry, who is creative and smart and kind, and with whom I made many wonderful memories. Peter Sherman, with whom I mentored many wonderful students. Manish Vuyyuru who pushed me to dream bigger than a Ph.D. And Jennifer Sun and Tina Liu, who were always there for me when the world fell apart (it did, twice).

My teachers and advisors. In particular: Beth Milhans, who taught me life is not fair (a useful lesson for a Ph.D. student), Patricia Horigan, who taught me to write, Brian Núñez who has always believed in me, Michelle Young, who has supported me at every step, Daniel Leedy, who taught me to love math, Tim Lund, whose slides I still (!) use, and David Siekmann, who 15 years ago decided to get up early every morning (unpaid!) to teach algebra to his students at Roosevelt Middle School because it wasn't offered by the school.

And finally, my family, who were there from the beginning, and who were an unwavering source of support on the darkest nights of my Ph.D.: my mother Mary Jo, who worked tirelessly to ensure that I got the very best education at every step of the way, my father Tom, who first inspired me to become a scientist, and my sibling Fawn, who is taller, cooler, and more successful than me... but at least not older.

Thank you all.

Chapter 1

What can we learn about tropospheric OH from satellite observations of methane? [1] [2]

1.1 Introduction

The hydroxyl radical (OH) is the main oxidant in the troposphere. It determines the lifetimes of most atmospheric species removed by oxidation such as methane (a major greenhouse gas), non-methane volatile organic compounds (NMVOCs, important for air quality), and hydrogenated halocarbons (contributing to stratospheric ozone loss). The global OH concentration and its trend have been monitored indirectly since the 1980s by measuring the concentration of methylchloroform (MCF), an industrial solvent removed from the atmosphere by reaction with OH (Bousquet et al., 2005; Krol et al., 1998; Lovelock, 1977; Patra et al., 2020; Prinn et al., 1987). MCF was banned in the 1990s because of its contribution to stratospheric ozone depletion, and its concentration is now approaching the

detection limit where it loses its value as a proxy for OH (Liang et al., 2017). An observation system simulation experiment (OSSE) previously suggested that a combination of thermal infrared (TIR) and shortwave infrared (SWIR) satellite observations of atmospheric methane could provide a continued proxy for global OH going forward (Zhang et al., 2018). Here we evaluate this idea with a joint inversion of AIRS and GOSAT satellite measurements for 2013-2015, examining the capability of the observations to quantify global OH concentrations as well as interannual, seasonal, and latitudinal variations.

The OH concentration is controlled by complex photochemistry (Lelieveld et al., 2016; Levy, 1971; Logan et al., 1981). The primary source is UV-B photolysis of ozone in the presence of water vapor. The main sinks are reactions with carbon monoxide (CO), methane, and NMVOCs, resulting in a lifetime ~1 second, and producing peroxy radicals that can be recycled to OH by reaction with nitric oxide (NO). The global mean tropospheric OH concentration is commonly expressed as the lifetime of methane against oxidation by tropospheric OH, τ_{CH4}^{OH}. From the methylchloroform proxy one infers the tropospheric lifetime of OH $\tau_{CH4}^{OH} = 10.2_{-0.7}^{+0.9}$ years for 2000 (Prinn et al., 2005). Current atmospheric chemistry models find a methane lifetime of 8.4 ± 0.3 years, implying that OH in the models is too high (Stevenson et al., 2020).

Although models are generally consistent in their simulations of global mean OH concentrations, there are large disagreements in the regional distributions of OH concentrations driven by NO_x and NMVOC distributions (Naik et al., 2013; Zhao et al., 2020), chemical mechanisms (Murray et al., 2021), clouds (Liu et al., 2006; Voulgarakis et al., 2009), and other meteorological variables (He et al., 2021). Models consistently simulate higher OH in the Northern Hemisphere (NH) than the Southern Hemisphere (SH) (Naik et al., 2013; Stevenson et al., 2020). MCF observations, by contrast, suggest no interhemispheric gradient (Patra et al., 2014), or slightly higher OH in the SH (Montzka et al., 2000). Models may have excessive OH in the northern hemisphere because of underestimated CO (Naik et al., 2013).

Understanding year-to-year variability and decadal-scale trends in OH concentrations is important for attributing the cause of methane fluctuations (Turner et al., 2017), including the

recent acceleration of the methane trend (Laughner et al., 2021; Qu et al., 2022; Stevenson et al., 2022). Methane is emitted from a range of poorly quantified sources including wetlands, livestock, waste, fuel exploitation, rice paddies, and open fires (Saunois et al., 2020). These sources could be responsible for methane interannual variability and trends but so could OH concentrations (Turner et al., 2017). The El Nino Southern Oscillation (ENSO) drives interannual variability in model OH due to its influence on lightning (Anderson et al., 2021; Murray et al., 2013; Turner et al., 2018), water vapor (Anderson et al., 2021; Turner et al., 2018), and CO emitted from biomass burning (Zhao et al., 2020). Models and measurements show a 5% range of interannual variability of OH over the last 30 years though with no temporal correlation between the two (Szopa et al., 2021). Models find increasing OH from 1980 to present driven by increases in anthropogenic NO_x emissions (Gaubert et al., 2017; Naik et al., 2013; Stevenson et al., 2020; Zhao et al., 2019). By contrast, MCF observations indicate OH increasing from 1980 to 2005 but then flat or decreasing after 2005 (Nicely et al., 2018; Rigby et al., 2017; Stevenson et al., 2020; Turner et al., 2017).

Many studies have used satellite observations of methane to infer methane emissions using specified OH concentrations to optimize methane sources (Turner et al., 2015), while others have attempted to optimize both methane sources and OH concentrations by exploiting differences in spatial/seasonal impacts on methane concentrations (Maasakkers et al., 2016; Zhang et al., 2021) or by including in the inversion complementary information from observations of MCF (Cressot et al., 2014; Cressot et al., 2016) or formaldehyde and CO (Yin et al., 2021). Inversions of GOSAT (SWIR) satellite observations of methane alone can constrain global mean OH about as well as MCF and infer a flat interhemispheric gradient, although posterior errors may be too optimistic (Lu et al., 2021; Maasakkers et al., 2019; Zhang et al., 2021). Zhang et al., (2018) proposed that TIR satellite observations of methane, which have sensitivity to the free troposphere and broader coverage over oceans and at night, may reduce error correlation between OH and methane emissions.

Satellite-based observations of methane in the TIR have been made continuously since 2002 by several instruments: AIRS (2002-present), TES (2004-2011), IASI (2007-present),

CrIS (2011-present), and GOSAT-2 (2018-present) (Jacob et al., 2016). TIR observations have received little attention in inverse studies because they are not sensitive to methane near the surface (Wecht et al., 2012). Direct applications of TIR satellite observations have mostly focused on processes affecting the free troposphere, such as detecting stratospheric intrusions (Xiong et al., 2013), methane emissions from large wildfires (Ribeiro et al., 2018; Xiong et al., 2010), interannual variations in mid-troposphere methane in response to ENSO (Corbett et al., 2017), seasonal fluctuations of methane in response to fossil fuel and rice paddy emissions in China (X. Zhang et al., 2011), and differences of seasonality compared to surface observations (Zhou et al., 2023). The combination of SWIR and TIR observations has been used to develop lower troposphere methane products including with GOSAT+AIRS (Worden et al., 2015), GOSAT+IASI (Schneider et al., 2022), and GOSAT-2 (Kuze et al., 2022; Suto, 2022).

Here we combine TIR observations from AIRS with SWIR observations from GOSAT in a three-year 2013-2015 inversion optimizing both methane emissions and OH concentrations. We use an analytical solution that provides formal characterization of posterior error statistics (including error correlations) and information content as part of the inversion. We place particular focus on the ability of the inversion to quantify global mean OH concentrations, interannual variability, and latitudinal and seasonal variations. This involves careful characterization of prior error covariances using OH concentrations from the ACCMIP model ensemble (Naik et al., 2013).

1.2   Data and Methods

We use 3 years (2013-2015) of satellite observations from GOSAT and AIRS (Sect. 2.1), to optimize a state vector of OH distributions and annual methane emissions. The observations are assembled in an observation vector $\boldsymbol{y}$ with total dimension m. The state vector $\boldsymbol{x}$ comprises n elements describing annual gridded non-wetland methane emissions, monthly subcontinental wetland methane emissions, and mean OH concentrations for individual years in different latitudinal bands and seasons (Sect. 2.2). Optimization is done by Bayesian

inference using a prior estimate x_A for the state vector and error covariances for that prior estimate (S_A) and for the observations (S_O) (Sect. 2.3), together with the GEOS-Chem chemical transport model $y = F(x)$ expressing the sensitivity of the observations to the state vector (Sect. 2.4). We use an analytical solution for minimization of the Bayesian cost function $J(x)$ to yield the optimal value (posterior estimate) $\hat{x}$ of the state vector, the posterior error covariance matrix $\hat{S}$, and metrics of information content (Sect. 2.5). The subsections below describe these different elements of the inversion except for the prior error covariance matrix of OH concentrations, which will be presented in a dedicated Sect. 3. Throughout this paper, we refer to "OH concentrations" or [OH] for a given domain as the mass-weighted average OH number density for that domain, and the global annual mean OH concentrations as $[\overline{OH}]$.

1.2.1 Satellite data

GOSAT (Greenhouse gases Observing SATellite), launched in 2009, detects methane by solar backscatter in the SWIR using the TANSO-FTS (Thermal And Near infrared Sensor for carbon Observation - Fourier Transform Spectrometer) instrument. In its default operating mode, GOSAT provides 10.5 km-diameter nadir observations of radiance separated by about 250 km along-track and cross-track on a sun-synchronous orbit with an equatorial overpass at about 1300 local solar time (LST). We use the University of Leicester CO_2-proxy methane retrieval v9.0 (Parker and Boesch, 2020), which uses the GOSAT observations in the 1.65 m band to retrieve methane as a column-averaged dry air mixing ratio X_{CH4} with a vertical sensitivity profile (column averaging kernel) of near-unity in the troposphere.

AIRS (Atmospheric Infrared Sounder), launched in 2002, detects methane by observing TIR radiation emitted by the Earth. AIRS provides 15 km-diameter nadir observations across a 1250 km swath with equatorial overpasses at about 0130 and 1330 LST, resulting in global coverage twice per day. We use the optimal estimation MUSES-AIRS retrieval of methane in the 8 and 12 m bands, which provides 26-level profiles of dry-air methane mixing ratio (Kulawik et al., 2021). The AIRS instrument has less than two degrees of freedom for signal
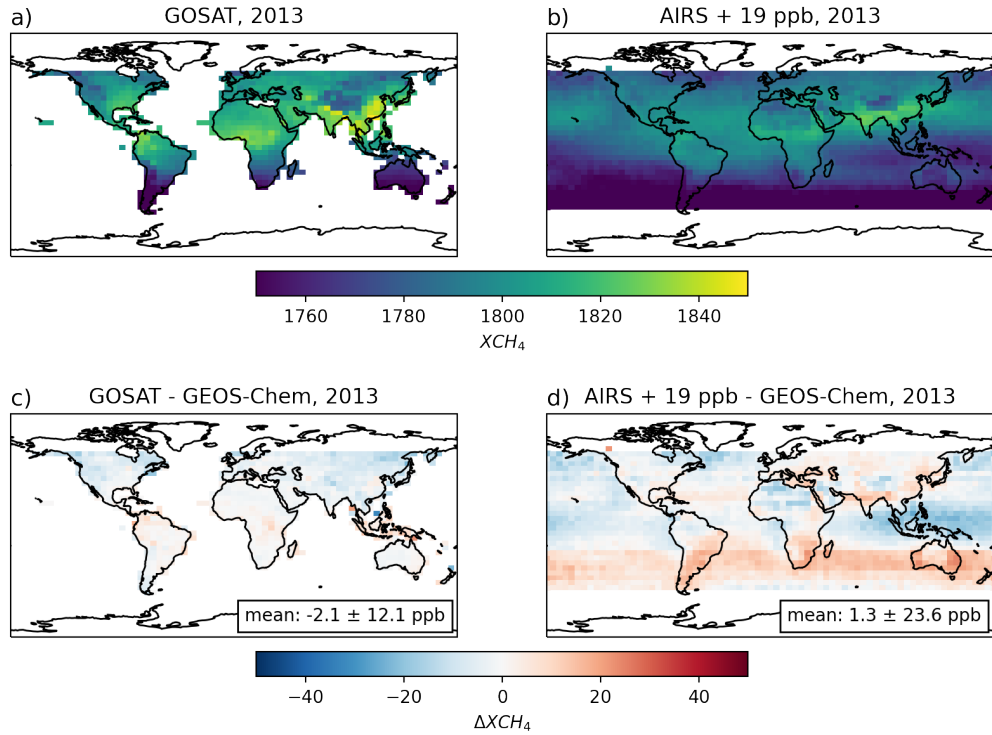
per measurement and little sensitivity to the lower troposphere. We therefore convert the vertical profiles to a column-averaged dry air mixing ratio X_{CH4} above 600 hPa, with column averaging kernels featuring maximum sensitivity to the upper troposphere. See Worden et al., (2015) for typical GOSAT and AIRS column averaging kernels.

For both AIRS and GOSAT, we remove measurements flagged for low quality, negative values, and surface pressures differing by more than 50 hPa from the local GEOS-Chem surface pressure which would indicate unresolved topography. We do not use GOSAT sunglint measurements because of their sparsity and seasonal sampling bias (Maasakkers et al., 2019). We also exclude measurements poleward of 60° due to model stratospheric bias in interpreting methane column observations in the polar vortex (Stanevich et al., 2020; Turner et al., 2015; Zhang et al., 2021). We include both daytime and nighttime measurements for AIRS, as we find no significant biases between them. This results in 600,000 successful retrievals for GOSAT and 2.5 million for AIRS.

In order to compare satellite retrievals to the GEOS-Chem simulations, we produce a model column sampled in the same manner as the satellite data. For each AIRS and GOSAT observation, we select the coincident GEOS-Chem grid cell and interpolate the GEOS-Chem methane mixing ratio profile, which is on 47 vertical levels, to the AIRS profile (26 vertical levels) and the GOSAT profile (20 vertical levels) using a mass-conserving interpolation algorithm described in Keppens et al. (2019) with Python code available on GitHub at https://github.com/pennelise/GOOPy (Penn and Nesser, 2024). We call these interpolated profiles $\mathbf{c}_m$. We then translate these profiles to column-averaged dry air mixing ratios using the column averaging kernel $\mathbf{a}$. The column averaging kernel is based on mixing ratio and does not include different pressure weights for each level (Boesch et al., 2011), so we apply the pressure weighting function ($\mathbf{h}$) provided in the GOSAT and AIRS data products. For an individual satellite X_{CH4} observation y, we derive the corresponding model value y_m using:

$$y_m = \mathbf{h}^T \left((\mathbf{I} - \mathbf{a})^T \mathbf{c}_a + \mathbf{a}^T \mathbf{c}_m \right) \tag{1.1}$$

where $\mathbf{I}$ is the unit vector and $\mathbf{c}_a$ is the prior profile provided by the GOSAT and AIRS

Figure 1.1: *GOSAT and AIRS observations of annual mean methane dry column mixing ratio (X_{CH4}) in 2013, binned by 4°x5° grid cells. GOSAT sunglint and observations poleward of 60° are not included. The bottom panels compare these observations with a GEOS-Chem simulation driven by 2013 posterior emissions from an inversion of GOSAT observations (Lu et al., 2021). A +19 ppb global bias correction is applied to AIRS on the basis of this comparison. Means and standard deviations of the differences between the satellite observations and GEOS-Chem are given inset.*

products, which come from the MACC-II methane inversion and TOMCAT stratospheric chemistry model for GOSAT and from the MOZART atmospheric chemistry model for AIRS.
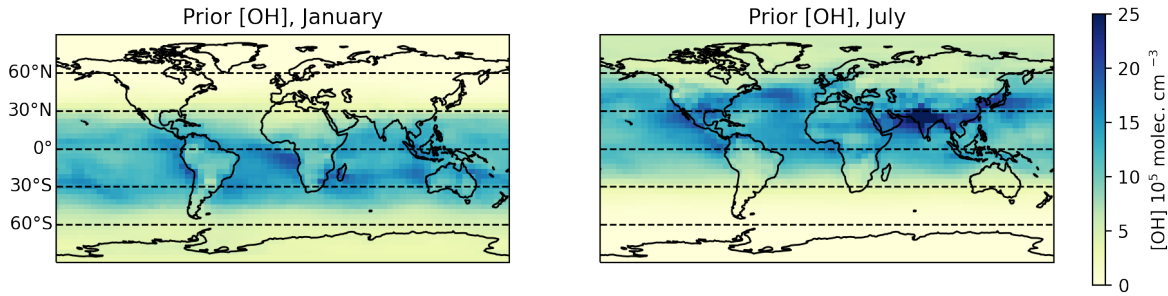
Figure 1.1 shows satellite observations from 2013 for GOSAT and AIRS compared to a 2013 GEOS-Chem simulation driven by GOSAT-optimized emissions from Lu et al. (2021). As expected, GOSAT is globally unbiased relative to this GEOS-Chem simulation (-2 ± 12 ppb), but AIRS is biased low (-19 ppb ± 24 ppb), and so we apply a correction of +19 ppb to the AIRS data to ensure consistency with GOSAT.

1.2.2 State vector and prior estimates

We optimize a state vector including annual gridded non-wetland emissions, monthly subcontinental wetland emissions, and OH distributions. Non-wetland emissions consist of 1009 4°x5° grid cells over land for each year (1009x3 = 3027 elements). Wetland emissions are optimized for each month and in 14 subcontinental regions following Bloom et al. (2017) (12x14x3 = 504 elements). OH concentrations are optimized for each season and year in four latitude bands of 30° each from 60°S to 60°N (4x4x3 = 48 elements). This results in $n = 3579$ total state vector elements.

We define $\mathbf{K} = \partial \mathbf{y}/\partial \mathbf{x}$ as the $m \times n$ Jacobian matrix describing the dependence of satellite observations on the state vector as simulated by GEOS-Chem. We calculate the Jacobian by perturbing each element of the state vector by 50% (for emissions) and 20% (for [OH]), resulting in $n + 1 = 3580$ forward model runs. The forward model is strictly linear in the relationship of concentrations to emissions, and the assumption of linearity is also acceptable for the relationship to OH concentrations in a 3-year simulation. Thus K fully defines GEOS-Chem for the purpose of the inversion.

The state vector elements are optimized in the inversion as scaling factors relative to prior estimates. We use the same prior estimates as Lu et al. (2021). Default prior anthropogenic emissions are from the EDGAR inventory v4.3.2 (Crippa et al., 2018) and are superseded for the US by the gridded EPA inventory of Maasakkers et al. (2016) and globally for oil, gas, and coal by the GFEI inventory of Scarpelli et al. (2020). Prior anthropogenic emissions are assumed constant except for manure and rice for which we apply seasonal scaling factors (Maasakkers et al., 2016; Zhang et al., 2016). Prior wetland emissions are from WetCHARTs v1.0 with 0.5°x0.5° spatial resolution and monthly temporal resolution, and including the partitioning into 14 subcontinental regions for use in inversions (Bloom et al., 2017). Additional prior emissions include the GFED inventory for fires at daily resolution (Randerson et al., 2017), and geologic sources from Etiope et al. (2019) scaled to the global total from Hmiel et al. (2020). Prior tropospheric OH concentrations (Figure 1.2) are archived monthly mean values from an older (version 5) GEOS-Chem simulation

Figure 1.2: *Mass-weighted tropospheric OH concentrations in GEOS-Chem used as prior estimates for the inversions. Monthly mean values for January and July are shown.*

on the 4°x5° grid (Wecht et al., 2014). The mass-weighted annual mean tropospheric OH concentration is $[\overline{OH}]$ = 11.2 × 10^5 molec. cm^{-3} consistent with the MCF-derived estimate from 2000 of $[\overline{OH}]$ = $10.8^{+0.77}_{-0.85}$ × 10^5 molec. cm^{-3} (Prinn et al., 2005). More recent versions of GEOS-Chem overestimate $[\overline{OH}]$ (Shah et al., 2023), consistent with the current generation of models (Stevenson et al., 2020).

1.2.3 Error estimates

The inversion requires specification of both observing system and prior error covariance matrices. The observing system error includes contributions from the measurement and from the forward model. We use the residual error method described in Heald et al. (2004) to derive it. We first split the observations into monthly 4°x5° grid cell subsets and compare observations within each subset to the GEOS-Chem simulation $F(x)$ using prior values. We then assume that the model bias ($b = \overline{F(x_A) - y}$) within each subset is due to error on the prior estimates, and that the residual represents the observing system error. We find in this manner mean observing system error standard deviations of 12 ppb for GOSAT and 22 ppb for AIRS, mostly contributed by the retrieval error with reported error standard deviations averaging 10 ppb for GOSAT and 16 ppb for AIRS. Our observing system error standard deviation for GOSAT is consistent with previous estimates (e.g. Lu et al., 2021; Qu et al., 2021; Zhang et al., 2021). We construct the observing system error covariance matrix assuming no error correlation between individual observations (diagonal matrix).

Prior error standard deviations for non-wetland emissions are assumed to be 50% of emissions for each 4°x5° grid cell with no error covariance between grid cells. For wetland emissions, we calculate the full prior error covariance matrix between all 14 regions and 36 months from the WetCHARTs model ensemble following Bloom et al. (2017), and then shrink the off-diagonal terms following Schäfer and Strimmer (2005) to ensure that the matrix is positive definite. Prior error estimates for the OH elements of the state vector are derived in Section 3.

1.2.4 Forward Model

We use the GEOS-Chem version 12.7.1 CH_4 simulation (DOI: 10.5281/zenodo.3676008) on a 4°x5° grid with 47 vertical layers as forward model for the inversion. Atmospheric transport is driven by the Modern-Era Retrospective Analysis, version 2 (MERRA-2) assimilated meteorological fields for 2013-2015 from the NASA Global Modeling and Assimilation Office. In addition to the tropospheric OH fields optimized in the inversion (Section 2.2), minor methane sinks in GEOS-Chem include stratospheric loss prescribed with 2-D oxidant fields (Murray et al., 2013), oxidation by tropospheric Cl following Wang et al. (2019), and soil uptake from the MeMo inventory (Murguia-Flores et al., 2018). Initial conditions for January 1, 2013 come from the GOSAT-optimized posterior simulation of Lu et al. (2021) and are globally unbiased with respect to GOSAT and adjusted AIRS observations as described in Section 2.1.

1.2.5 Inversion

We perform three inversions: "GOSAT-only" optimized with GOSAT observations, "AIRS-only" optimized with AIRS observations, and "GOSAT+AIRS" optimized with both. The equations below are for the inversion using both GOSAT and AIRS observations. Because we assume no error correlations between the instruments, an inversion with only one instrument can be derived by removing all terms pertaining to the other instrument.

We minimize a Bayesian cost function that accounts for the distance from the prior

estimate ($\mathbf{x}_A$) and the satellite observations ($\mathbf{y}$), weighted by the inverse of the prior ($\mathbf{S}_A$) and observing system ($\mathbf{S}_O$) error covariance matrices, and including an additional regularization factor (γ). Observing system components from GOSAT and AIRS are denoted by subscripts. Assuming normal errors, and further assuming no correlation between GOSAT and AIRS errors, the cost function is given by:

$$
\begin{aligned}
\mathbf{J}(\mathbf{x}) = {} & (\mathbf{x} - \mathbf{x}_A)^T \mathbf{S}_A^{-1} (\mathbf{x} - \mathbf{x}_A) \\
& + \gamma_{GOSAT} (\mathbf{y}_{GOSAT} - \mathbf{K}_{GOSAT}\mathbf{x})^T \mathbf{S}_{O,GOSAT}^{-1} (\mathbf{y}_{GOSAT} - \mathbf{K}_{GOSAT}\mathbf{x}) \\
& + \gamma_{AIRS} (\mathbf{y}_{AIRS} - \mathbf{K}_{AIRS}\mathbf{x})^T \mathbf{S}_{O,AIRS}^{-1} (\mathbf{y}_{AIRS} - \mathbf{K}_{AIRS}\mathbf{x})
\end{aligned}
\tag{1.2}
$$

We can then solve $\min(J(x))$ analytically by setting $\frac{\partial J}{\partial x}_{=0}$ and obtain the posterior solution $\widehat{\mathbf{x}}$ (Rodgers, 2000):

$$
\begin{aligned}
\widehat{\mathbf{S}} = \big(& \gamma_{GOSAT}\mathbf{K}_{GOSAT}^T \mathbf{S}_{O,GOSAT}^{-1} \mathbf{K}_{GOSAT} \\
& + \gamma_{AIRS}\mathbf{K}_{AIRS}^T \mathbf{S}_{O,AIRS}^{-1} \mathbf{K}_{AIRS} \\
& + \mathbf{S}_A^{-1} \big)^{-1}
\end{aligned}
\tag{1.3}
$$

where $\widehat{\mathbf{x}}$ is the posterior estimate for the state vector and $\mathbf{G}_{AIRS}$ and $\mathbf{G}_{GOSAT}$ are the gain matrices:

$$
\begin{aligned}
\mathbf{G}_{AIRS} &= \mathbf{S}_A \mathbf{K}_{AIRS}^T \left(\mathbf{K}_{AIRS} \mathbf{S}_A \mathbf{K}_{AIRS}^T + \frac{\mathbf{S}_{O,AIRS}}{\gamma_{AIRS}} \right)^{-1} \\
\mathbf{G}_{GOSAT} &= \mathbf{S}_A \mathbf{K}_{GOSAT}^T \left(\mathbf{K}_{GOSAT} \mathbf{S}_A \mathbf{K}_{GOSAT}^T + \frac{\mathbf{S}_{O,GOSAT}}{\gamma_{GOSAT}} \right)^{-1}
\end{aligned}
\tag{1.4}
$$

The analytical solution also yields a closed-form expression for the posterior error covariance matrix $\widehat{\mathbf{S}}$ characterizing the normal error on $\widehat{\mathbf{x}}$:

$$
\widehat{\mathbf{S}} = \left(\gamma_{GOSAT}\mathbf{K}_{GOSAT}^T \mathbf{S}_{O,GOSAT}^{-1} \mathbf{K}_{GOSAT} + \gamma_{AIRS}\mathbf{K}_{AIRS}^T \mathbf{S}_{O,AIRS}^{-1} \mathbf{K}_{AIRS} + \mathbf{S}_A^{-1} \right)^{-1}
\tag{1.5}
$$

We can also derive the averaging kernel matrix $\partial \widehat{\mathbf{x}}/\partial \mathbf{x}$ that describes the sensitivity of the posterior estimate to the true state:

$$\mathbf{A} = \mathbf{I_n} - \widehat{\mathbf{S}}\mathbf{S}_A^{-1} \tag{1.6}$$

The trace of the averaging kernel gives us the Degrees of Freedom for Signal (DOFS), which describes the number of pieces of independent information derived from the inversion.

For some of our applications we will aggregate state vector elements into a reduced state vector x_{red} using a summation matrix W:

$$\widehat{\mathbf{x}}_{\mathbf{red}} = \mathbf{W}\widehat{\mathbf{x}} \tag{1.7}$$

and derive the corresponding averaging kernel ($\mathbf{A_{red}}$) and posterior error covariance ($\widehat{\mathbf{S}}_{\mathbf{red}}$) for the aggregated solution:

$$\mathbf{A_{red}} = \mathbf{W}\mathbf{A}\mathbf{W}^* \tag{1.8}$$

$$\widehat{\mathbf{S}}_{\mathbf{red}} = \mathbf{W}\widehat{\mathbf{S}}\mathbf{W^T} \tag{1.9}$$

where $\mathbf{W}^*$ is the Moore-Penrose pseudoinverse of $\mathbf{W}$.

The regularization factor is intended to avoid overfitting to observations caused by not accounting for error covariance in the observing system (matrix S_O) We determine the appropriate value for γ using the technique described in Lu et al. (2021). The sum of prior terms in the posterior value of the cost function, $\mathbf{J_A}\left(\widehat{\mathbf{x}}\right) = \left(\widehat{\mathbf{x}} - \mathbf{x}_A\right)^T \mathbf{S}_A^{-1}\left(\widehat{\mathbf{x}} - \mathbf{x}_A\right)$, *should* follow a chi-square distribution with expected value $\mathbf{J_A}\left(\widehat{\mathbf{x}}\right) = n$, and we adjust γ to achieve this. We determine γ_{GOSAT} and γ_{AIRS} separately using GOSAT-only and AIRS-only inversions. We find in this manner $\gamma_{GOSAT} = 0.2$ and $\gamma_{AIRS} = 0.1$. To provide equal weight to [OH] and methane emissions in the cost function, we follow Maasakkers et al. (2019) and scale the OH prior error covariance matrix $\mathbf{S_{A,OH}}$ by the ratio of the number of emission state vector elements to OH state vector elements, or 3531/48, before inserting them into the full prior error matrix $\mathbf{S_A}$.

1.3 Construction of prior error covariance matrix for OH concentrations

GOSAT observations of methane have been used in inversions to infer the global mean tropospheric OH concentration, its interannual variability, and its interhemispheric difference (Maasakkers et al., 2019; Qu et al., 2021, 2024; Zhang et al., 2021). Here we explore how much information satellite observations can actually provide on OH concentrations by including in the state vector the OH concentrations in individual years (2013-2015), four latitudinal bands, and four seasons, for a total of 48 state vector elements (Section 2.2) for which we can diagnose posterior error correlations and information content. This requires accounting for prior error correlations between these different elements, as represented in a 48×48 matrix $S_{A,OH}$.

We construct the prior error covariance matrix for OH in the following manner. First, we specify the error statistics for global annual mean mass-weighted tropospheric OH concentrations, $[\overline{OH}]$. This includes a systematic error of 10% within the MCF constraint (Prinn et al., 2005) and an interannual variability error that we estimate to be 5% on the basis of interannual variability of model and MCF-derived $[\overline{OH}]$ reported by Holmes et al. (2013). Thus the prior error covariance matrix for $[\overline{OH}]$ in our three simulation years (2013-2015), in unit of fractional error variances and covariances, is given by a 3×3 matrix $\overline{S_{A,OH}} = (\sigma_{ij}^2)$:

$$\overline{S_{A,OH}} = \begin{bmatrix} 0.05^2 + 0.1^2 & 0.1^2 & 0.1^2 \\ 0.1^2 & 0.05^2 + 0.1^2 & 0.1^2 \\ 0.1^2 & 0.1^2 & 0.05^2 + 0.1^2 \end{bmatrix} \tag{1.10}$$

Prior error correlations between OH concentrations in different latitudinal bands and seasons should account for our current knowledge of the OH distribution. We use for this purpose monthly mean output for one year from the ensemble of 11 independent ACCMIP global atmospheric chemistry models reported in Naik et al. (2013). All ACCMIP models include the same anthropogenic emissions of NO_x, CO, and NMVOCs. They have different natural emissions, chemical mechanisms, and meteorology. Global distributions of OH
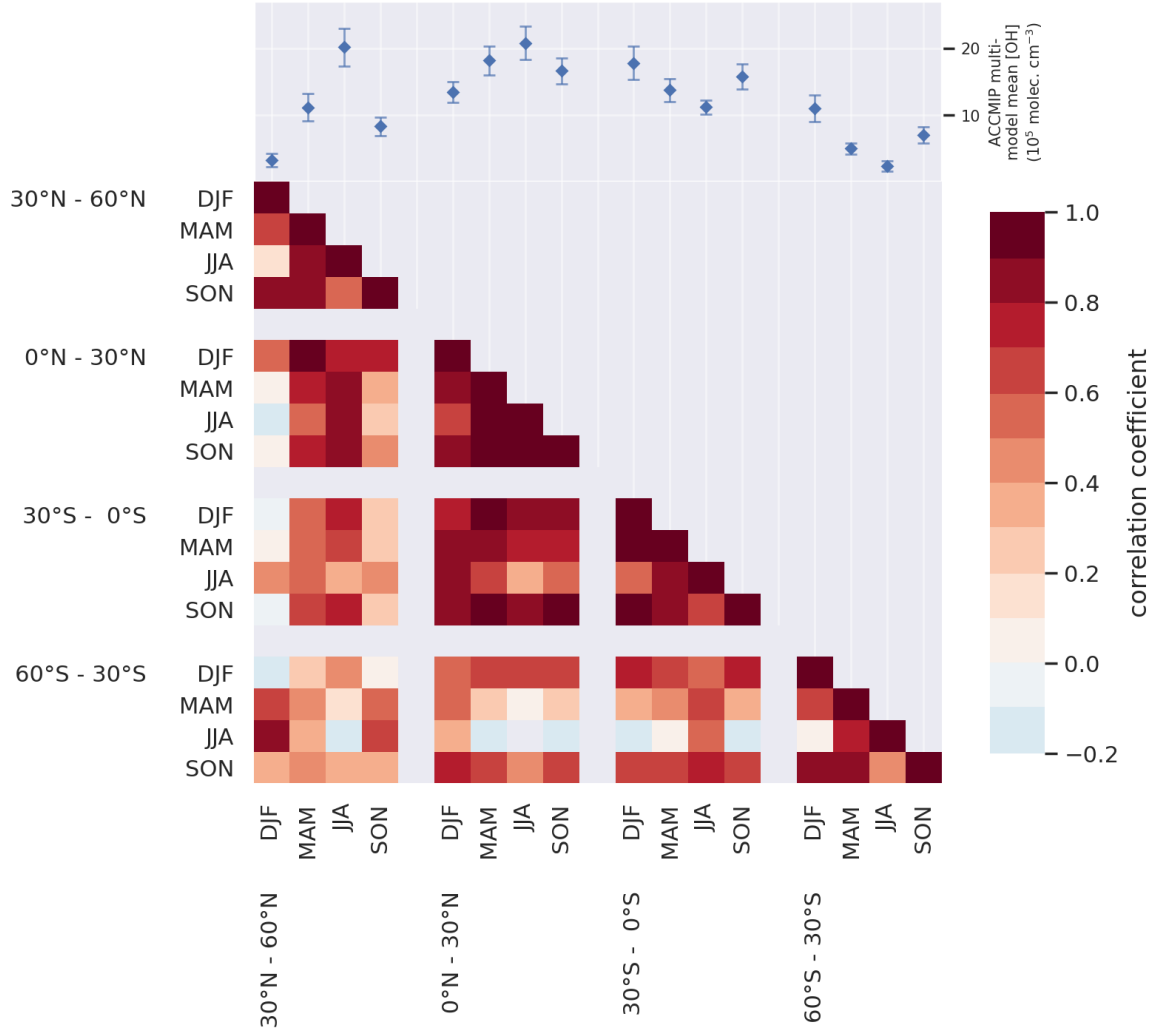
concentrations in each ACCMIP model were presented previously in Zhang et al. (2018). For each ACCMIP model, we calculate the mass-weighted integral of OH concentrations vertically up to 200 hPa for each 30° latitude band for each season. We then compute the variances and covariances between each latitude band and season across the ensemble of ACCMIP models. The resulting 16x16 covariance matrix for the ACCMIP models $\mathbf{S_{A,AM}}$ is taken as the error covariance matrix in the spatial-seasonal distribution of OH for the inversion, with error standard deviations represented by a diagonal matrix $\mathbf{D}$.

Figure 1.3 shows the spatial and seasonal error correlation matrix $\mathbf{R_{A,AM}}$ and the error standard deviations $\mathbf{D}$ calculated directly from the ACCMIP ensemble, such that $\mathbf{S_{A,AM}=DR_{A,AM}D}$. We find strong error correlations in the tropics for all seasons, indicating a commonality of effects driving [OH] differences between models. Error correlations are also strong between mid-latitudes summer and the tropics, likely for the same reasons. Mid-latitude OH concentrations in other seasons show much weaker error correlations, implying that they are driven by different photochemistry and emissions as might be expected. Northern and southern midlatitudes are highly correlated in their respective winters.

We replicate the 16×16 spatial-seasonal OH error covariance matrix $S_{A,AM}$ constructed from the ACCMIP data to create a 48×48 error covariance matrix for the three years of our analysis, resulting in the block matrix:

$$\begin{bmatrix} \mathbf{S_{A,AM}} & \mathbf{S_{A,AM}} & \mathbf{S_{A,AM}} \\ \mathbf{S_{A,AM}} & \mathbf{S_{A,AM}} & \mathbf{S_{A,AM}} \\ \mathbf{S_{A,AM}} & \mathbf{S_{A,AM}} & \mathbf{S_{A,AM}} \end{bmatrix} \tag{1.11}$$

This matrix is low rank because it was constructed with information from only 11 models to estimate 48 state vector elements. We use the method of Schäfer and Strimmer (2005) to shrink the off-diagonal errors and produce a matrix that is positive definite and invertible. Schäfer and Strimmer (2005) show that their method produces a more accurate estimate of the true error covariance matrix (where accuracy is defined by comparison of the true

Figure 1.3: *Error correlations for model OH concentrations in different latitude bands and seasons (denoted* $\mathbf{R_{A,AM}}$ *in the text). Pearson's error correlation coefficients are calculated for the ensemble of 11 different ACCMIP models. The mean and standard deviation of the ACCMIP ensemble for each latitude and season is inset above.*
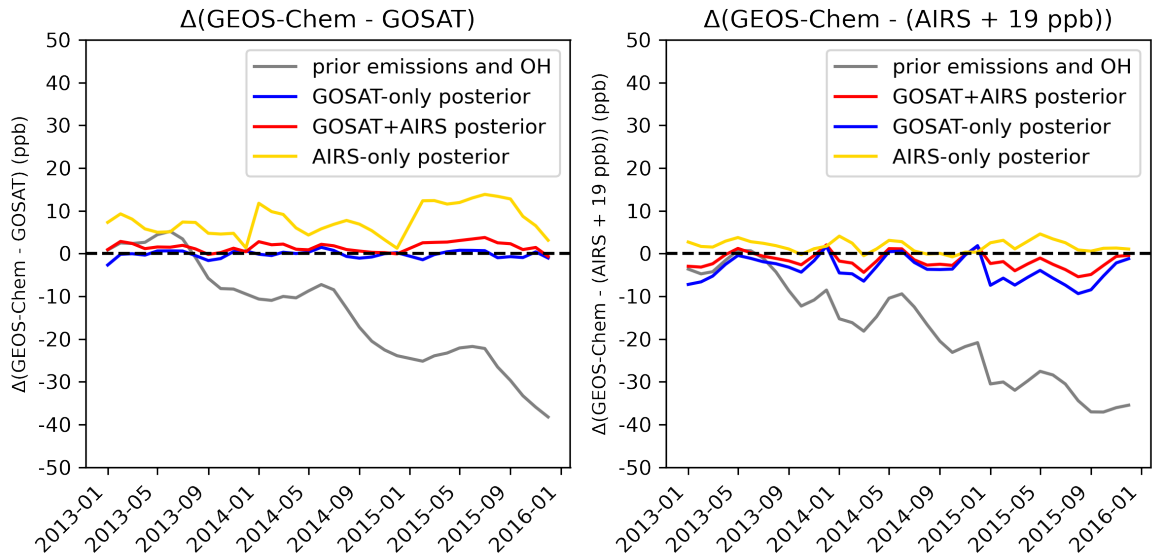
and estimated eigenvalues). After off-diagonal shrinkage, matrices along the diagonal of the block matrix differ from those off-diagonal. We refer to the resulting 16x16 covariance matrices of spatial-seasonal errors within years as $\mathbf{S_{A,AM}}''$, and between years as $\mathbf{S_{A,AM}}'$. Additionally, we refer to the error variances of the global mean $\overline{[OH]}$ for one year inferred from these matrices as $\sigma^2_{AM}{}''$ and $\sigma^2_{AM}{}'$.

We can then construct $\mathbf{S_{A,OH}}$ from the regularized ACCMIP covariance matrices $\mathbf{S_{A,AM}}''$ and $\mathbf{S_{A,AM}}'$ scaled by the annual mean error variances inferred from the MCF observations σ^2_{ij} (Eq. (10)) and the spatial-seasonal error variances inferred from the ACCMIP model $\sigma^2_{AM}{}''$ and $\sigma^2_{AM}{}'$. We can formulate $\mathbf{S_{A,\,OH}}$ as a block matrix, where each block is an appropriately scaled ACCMIP covariance matrix for one year, as shown:

$$\mathbf{S_{A,OH}} = \begin{bmatrix} \frac{\sigma^2_{11}}{\sigma^2_{AM}{}''}\mathbf{S_{A,\,AM}}'' & \frac{\sigma^2_{12}}{\sigma^2_{AM}{}'}\mathbf{S_{A,\,AM}}' & \frac{\sigma^2_{13}}{\sigma^2_{AM}{}'}\mathbf{S_{A,\,AM}}' \\ \frac{\sigma^2_{21}}{\sigma^2_{AM}{}'}\mathbf{S_{A,\,AM}}' & \frac{\sigma^2_{22}}{\sigma^2_{AM}{}''}\mathbf{S_{A,\,AM}}'' & \frac{\sigma^2_{23}}{\sigma^2_{AM}{}'}\mathbf{S_{A,\,AM}}' \\ \frac{\sigma^2_{31}}{\sigma^2_{AM}{}'}\mathbf{S_{A,\,AM}}' & \frac{\sigma^2_{32}}{\sigma^2_{AM}{}'}\mathbf{S_{A,\,AM}}' & \frac{\sigma^2_{33}}{\sigma^2_{AM}{}''}\mathbf{S_{A,\,AM}}'' \end{bmatrix} \tag{1.12}$$

This enforces error variances and covariances for annual global mean OH concentrations identical to the values σ^2_{ij} from Eq. (10).

We refer to Eq. (12) as the full-correlations error covariance matrix. We will also test the effect of simpler OH correlation assumptions on inversion results, while keeping the state vector the same. First is a no-correlations error covariance matrix that assumes diagonal errors for the OH concentration, with no error correlation between years, seasons, or latitude bands. Second is a correlated years error covariance matrix that includes error correlations between years but with no spatial-seasonal structure. We scale the correlated-years error covariance matrix such that the error (co)variances for $\overline{[OH]}$ are identical to $\overline{\mathbf{S_{A,OH}}}$ in Eq. (10). We cannot do the same for the no-correlations error covariance matrix because it is diagonal; however we scale it such that the error variance of the three-year average is identical to that represented by $\overline{\mathbf{S_{A,OH}}}$. The variance of the three-year average is therefore identical for all three error covariance matrices.

16
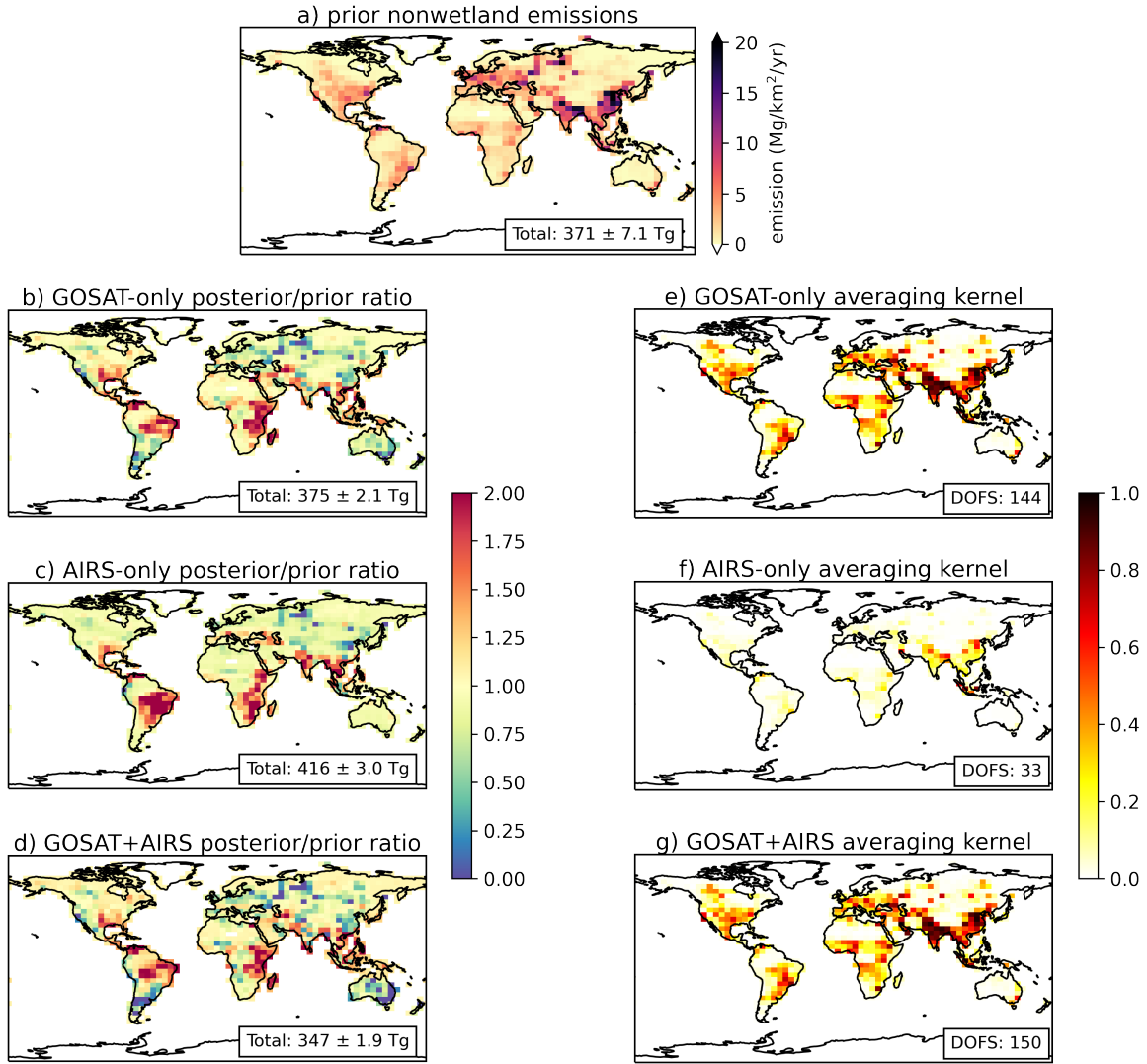
Figure 1.4: *Difference between the global mean dry column mixing ratio (X_{CH4}) simulated by GEOS-Chem and observed by GOSAT (left) and AIRS (right). Monthly mean results are shown for the 2013-2015 inversion period. The GEOS-Chem simulation is driven by either prior or posterior values for emissions and OH concentrations. Posterior values are from inversions using either GOSAT or AIRS observations or both. The 19 ppb correction applied to AIRS observations is to remove the bias with GOSAT.*

1.4 Results & discussion

1.4.1 Quantifying emissions

Figure 1.4 compares the global mean dry column mixing ratio (X_{CH4}) simulated by GEOS-Chem and observed by GOSAT and AIRS. The prior simulation shows an increasing negative bias with time because of an incorrect balance between methane sources and sinks. All inversions (posterior solutions) are successful in correcting this bias, including its seasonality.

The inversions optimize both methane emissions and OH concentrations. Figure 1.5 shows the prior non-wetland emissions and 2013-2015 posterior/prior correction factors for all three inversions, as well as the averaging kernel sensitivities. The GOSAT-only inversion (Figure 1.5b) shows upward corrections to the southern United States, Brazil, and East Africa, and downward corrections to East Asia and parts of Russia, consistent with Zhang et al. (2021) who used similar prior estimates. The AIRS-only inversion shows generally similar results but weaker averaging kernel sensitivities. Results from the AIRS-only inversion are

17

Figure 1.5: *Optimized global distributions of 2013-2015 non-wetland methane emissions using GOSAT, AIRS, and GOSAT+AIRS observations. Prior emissions are shown in (a). The average posterior/prior ratios from 2013-2015 for inversions with each set of observations are shown in (b)-(d). Total emissions are inset in (a)-(d) with their error standard deviations. Averaging kernel sensitivities (diagonal elements of the averaging kernel matrix) averaged over 2013-2015 are shown in (e)-(g). The averaging kernel sensitivities represent the ability of the inversion to constrain the posterior solution independently from the prior estimate (1= fully, 0 = not at all). The degrees of freedom for signal (DOFS) for the 1009 4°x5° grid cells averaged over 3 years are inset.*
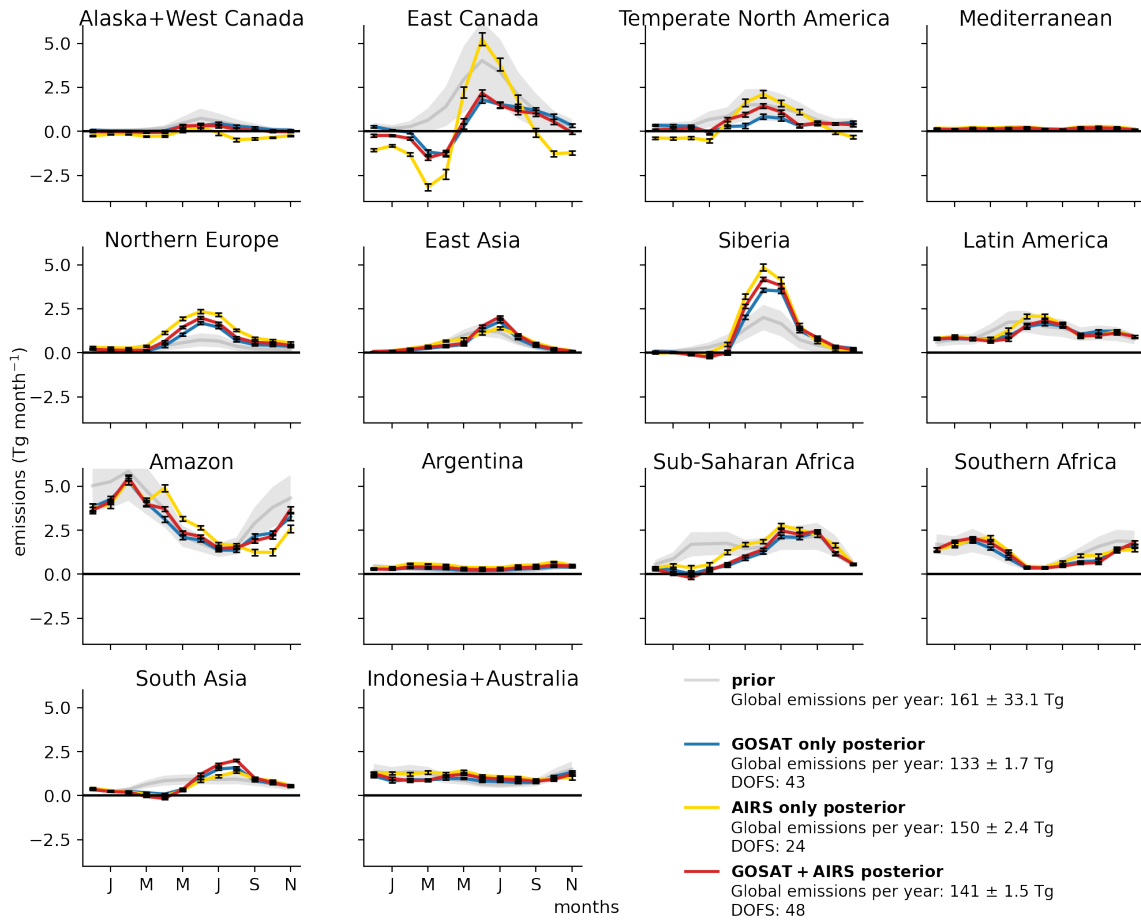
consistent with those of the GOSAT-only inversion with the exception of strong upward corrections over Brazil, Argentina, and India, which together cause much higher global methane emissions in the AIRS-only solution than the two solutions constrained by GOSAT observations. The greater power of the GOSAT data to constrain emissions on the 4°x5° grid is measured by the DOFS (144 for GOSAT, 33 for AIRS). Adding AIRS observations to GOSAT increases the DOFS by only 4% as the information on emissions from these two sensors overlaps.

We find small (<10 Tg a^{-1}) changes from year to year for methane emissions in all solutions, and most of these changes are attributed to non-wetland emissions. This is consistent with the solutions in Yin et al. (2021) who find global methane emissions changes over 2013-2015 on the order of 1-2%.

Figure 1.6 shows inversion results for the seasonality of wetland emissions in the 14 subcontinental regions of the WetCHARTs inventory used as prior estimate. The seasonality and magnitude of the GOSAT and GOSAT+AIRS posterior estimates are consistent with Zhang et al. (2021), who used a similar wetland state vector but with more years of GOSAT data. Our posterior produces negative emissions in Boreal North America in the spring, which are also seen in the solution of Zhang et al. (2021). They attribute these negative emissions to potential soil sinks in the region. Remarkably, the AIRS-only inversion shows the same feature. Remarkably, the posterior global sum of non-wetland and wetland emissions in the GOSAT and GOSAT+AIRS inversions is lower than the prior estimate, even though the prior simulation is biased low (Figure 1.4). This is because of a compensating decrease in $[\overline{OH}]$, as analyzed below.

1.4.2 Quantifying global mean OH concentrations independently of emissions

We now turn our attention to the ability of the satellite observations to constrain the global annual mean OH concentration, $[\overline{OH}]$, independently of emissions and for individual years. Let E denote the global annual mean methane emission rate. The annual rate of change in atmospheric methane mass, m/t, is given by
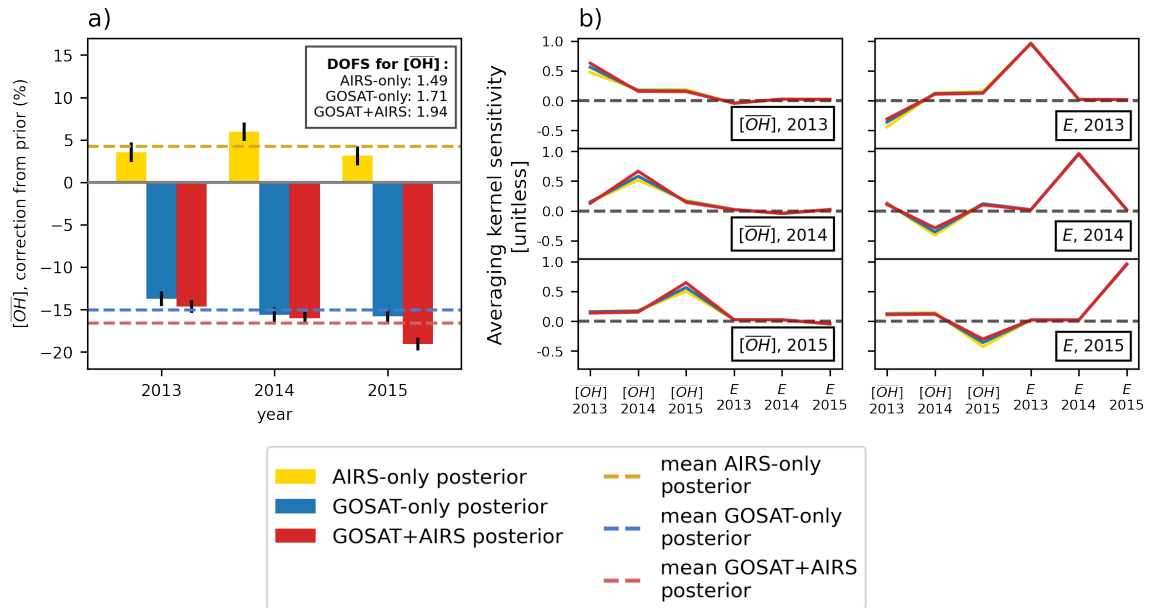
Figure 1.6: *Monthly mean 2013-2015 wetland emissions for the 14 WetCHARTs subcontinental regions as defined by Bloom et al. (2017). Prior emission estimates from the mean of the WetCHARTs inventory ensemble are compared to posterior emissions from the GOSAT, AIRS, and GOSAT+AIRS inversions. The degrees of freedom (DOFS) for signal aggregated to 14 regions x 12 months = 168 state vector elements are also given.*

$$\frac{\Delta m}{\Delta t} = E - k \left[\overline{OH} \right] m - L \tag{1.13}$$

where k is the rate constant for oxidation of methane by tropospheric OH with a suitable temperature kernel (Prather and Spivakovsky, 1990) and L is the sum of other minor sinks with $L \ll k[\overline{OH}]m$. Considering that m/t is set by the observations used in the inversion, and L is minor and not optimized, we see that corrections to E and $\left[\overline{OH} \right]$ are necessarily correlated. In order to constrain $\left[\overline{OH} \right]$ we need independent information on emissions. The lower-atmosphere gradients over land observed by GOSAT can provide that information, as pointed out by Zhang et al. (2021) and shown in Section 4.1, but the AIRS TIR measurements cannot and this is reflected in the low DOFS of Figures 1.5 and 1.6. We focus therefore on the GOSAT and GOSAT+AIRS observing configurations to evaluate their capability to constrain $\left[\overline{OH} \right]$ in individual years separately from emissions.

Figure 1.7 shows the corrections to E and $\left[\overline{OH} \right]$ for individual years from the inversions. The inversions apply a systematic correction to $\left[\overline{OH} \right]$ in all three years, reflecting bias in the prior [OH], and a smaller interannual variability. The right panels show the rows of the reduced averaging kernel matrix summing emissions globally (Eq. (8)) and diagnosing the ability of the inversion to correct separately $\left[\overline{OH} \right]$ and E in individual years. We find that the averaging kernels for $\left[\overline{OH} \right]$ in individual years are strongly peaked, with no significant aliasing from emissions and only minor aliasing with $\left[\overline{OH} \right]$ for other years. We conclude that $\left[\overline{OH} \right]$ can be optimized for individual years and independently of emissions. Some aliasing of the inverse solution to $\left[\overline{OH} \right]$ across years is to be expected in view of the long lifetime of methane but we are still able to capture individual years and thus interannual variability of $\left[\overline{OH} \right]$. GOSAT+AIRS provides only slightly more information than GOSAT alone. A similar averaging kernel analysis by (Maasakkers et al., 2019) for 2010-2015 GOSAT observations found that the observations could constrain the average $\left[\overline{OH} \right]$ over all years but not the interannual variability. In that study the emission trend was imposed to be linear, which would strongly detract from the ability to independently constrain interannual variability of $\left[\overline{OH} \right]$.

21
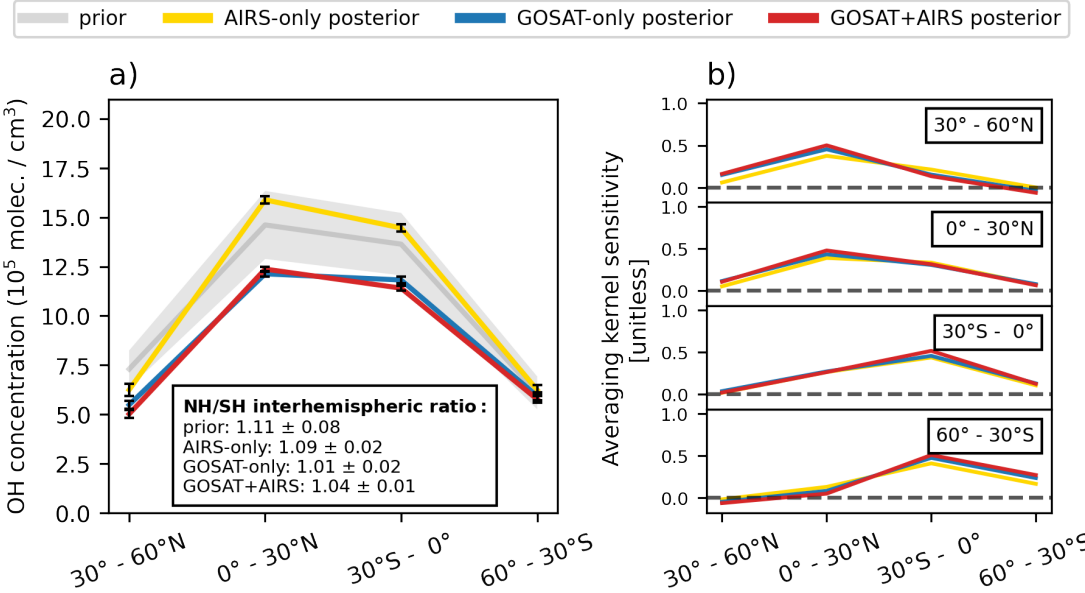
Figure 1.7: *Ability of inversions using GOSAT and GOSAT+AIRS methane observations to quantify global annual mean tropospheric* $\boxed{\overline{\text{OH}}}$ *for individual years and independently from emissions. (a) 2013-2015 percentage corrections to the* $\boxed{\overline{\text{OH}}}$ *prior estimate. Prior and posterior error standard deviations are shown as error bars. DOFS are shown inset (DOFS = 3 would imply perfect separate quantification of* $\boxed{\overline{\text{OH}}}$ *in individual years). (b) Rows of the reduced averaging kernel matrix describing the ability of the observing system to separately quantify emissions (E) and* $\boxed{\overline{\text{OH}}}$ *for the individual years. A perfect observing system would have an averaging kernel sensitivity of 1 for the reduced state vector element of interest (perfect characterization) and 0 for other elements (no sensitivity of the solution to other elements).*

1.4.3 Resolving spatial and seasonal patterns in OH concentrations

We now investigate the ability of the methane observations to constrain the spatial and seasonal variations of OH concentrations. Figure 1.8 shows the corrections to OH concentrations from the inversion as a function of latitude, along with the corresponding rows of the averaging kernel matrix. We find that GOSAT and GOSAT+AIRS provide only weak constraints on the OH latitudinal distribution because prior errors from the ACCMIP ensemble are highly correlated (Figure 1.3). We are unable to resolve the midlatitudes, where averaging kernel rows show higher sensitivity to the adjacent tropical latitude band, and almost no sensitivity to the midlatitudes themselves. There is some information on the interhemispheric ratio of OH concentrations, with the inversion decreasing the NH/SH ratio from 1.11±0.08 in the prior estimate to 1.01±0.02 (for GOSAT) and 1.04±0.01 (for GOSAT+AIRS). This is consistent with previous inversions of methane observations showing downward corrections in the NH/SH ratio (Zhang et al., 2021) and independent evidence from MCF observations that current model NH/SH ratios are too high (Naik et al., 2013; Patra et al., 2014). Nevertheless, we see from the averaging kernels that there is significant aliasing of the information between the northern and southern tropics, because errors are highly correlated across models (Figure 1.3). It could be that the ensemble of ACCMIP models exaggerates the error correlation on account of using the same anthropogenic emissions, but OH in the tropics is more sensitive to lightning, fires, and clouds which vary across the models.
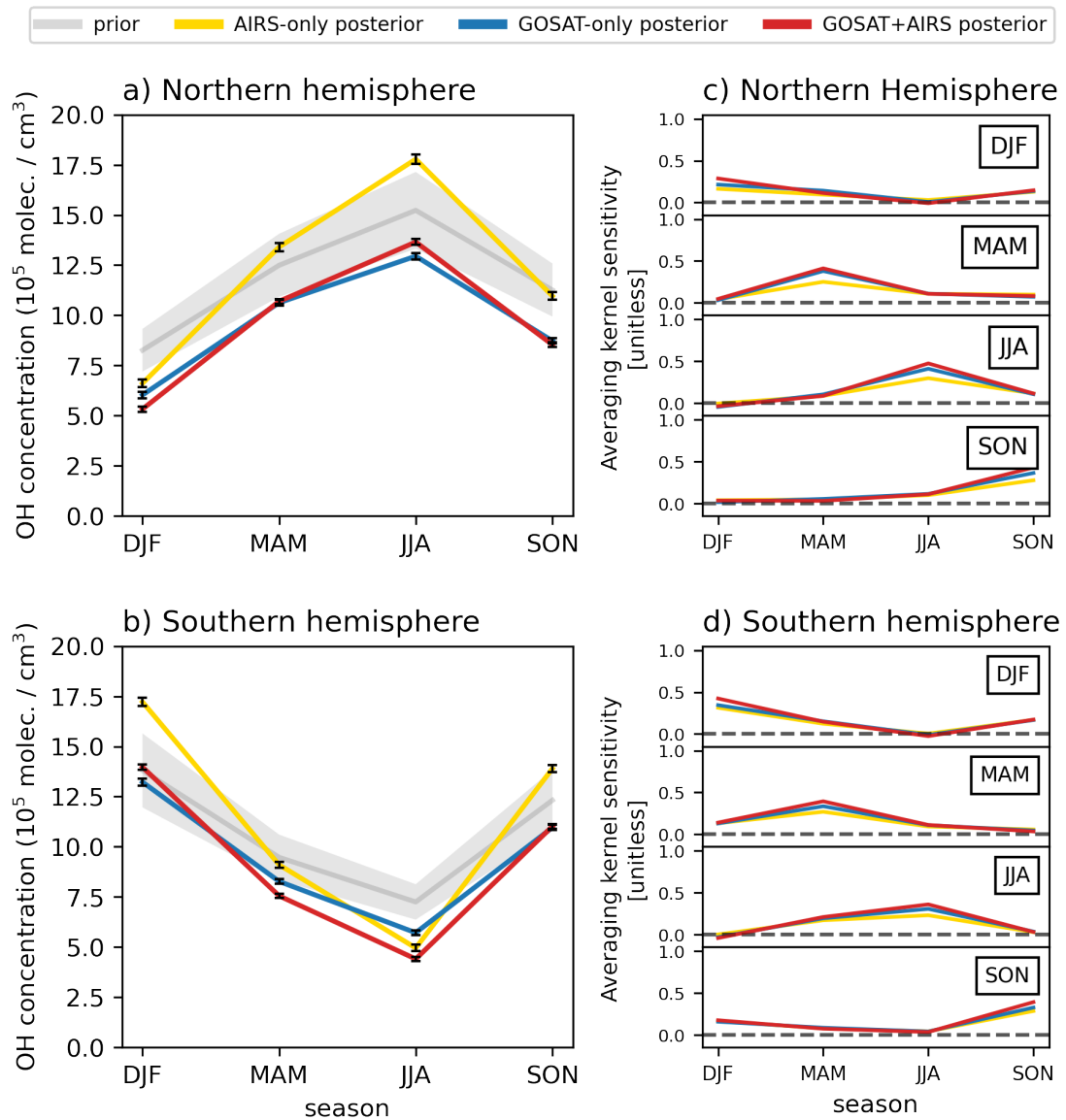
The seasonal cycle for [OH] is shown in Figure 1.9. We find from the averaging kernel matrix that the inversion provides significant information on the seasonality of [OH] in the two hemispheres, despite the smearing across latitudinal bands found in Figure 1.8. There is some aliasing between adjacent seasons but winter and summer are well separated, mainly for the tropics since there is little information from mid-latitudes (Figure 1.8). The GOSAT+AIRS inversion increases the amplitude of the seasonal cycle in both hemispheres. The posterior seasonal patterns from the GOSAT and GOSAT+AIRS inversions do not differ significantly from the prior, which demonstrates a good understanding of the OH

Figure 1.8: *Ability of inversions of GOSAT and GOSAT+AIRS methane observations to resolve the latitudinal variability of OH concentrations. (a) Latitudinal distribution of mass-weighted tropospheric [OH] in the prior estimate (prior error standard deviation in shading) and in the posterior estimates. The NH/SH interhemispheric ratio and its error standard deviation are inset. (b) Rows of the reduced averaging kernel matrix describing the ability of the observing system to separately quantify [OH] in different latitudinal bands. A perfect observing system would have an averaging kernel sensitivity of 1 for the reduced state vector element of interest (perfect characterization) and 0 for other elements (no error correlation).*

seasonality on the hemispheric scale.

We have found that the ability of the inversion to optimize spatial and temporal features of the OH distribution is limited by prior error correlations from the independent knowledge expressed by the ACCMIP models. We examined the effect of these prior error correlations in sensitivity simulations for GOSAT-only inversions in which we either assumed no error correlations between OH state vector elements, or error correlations only for the interannual variability of $\overline{OH}$ as described by Eq. (10). Aggregated errors on $\overline{OH}$ were scaled to be the same in all inversions as described in Sect. 3. Fig. 1.10 shows the results for the GOSAT-only inversion. Constraints on $\overline{OH}$ are similar across all inversions, as would be expected since our base full-correlations inversion can effectively constrain that quantity for individual years. The inversions without error correlations show larger perturbations to the latitudinal distribution of [OH], with higher values at mid-latitudes and lower in the tropics,

Figure 1.9: *Same as Figure 1.8 but for the seasonality of OH concentrations in each hemisphere.*
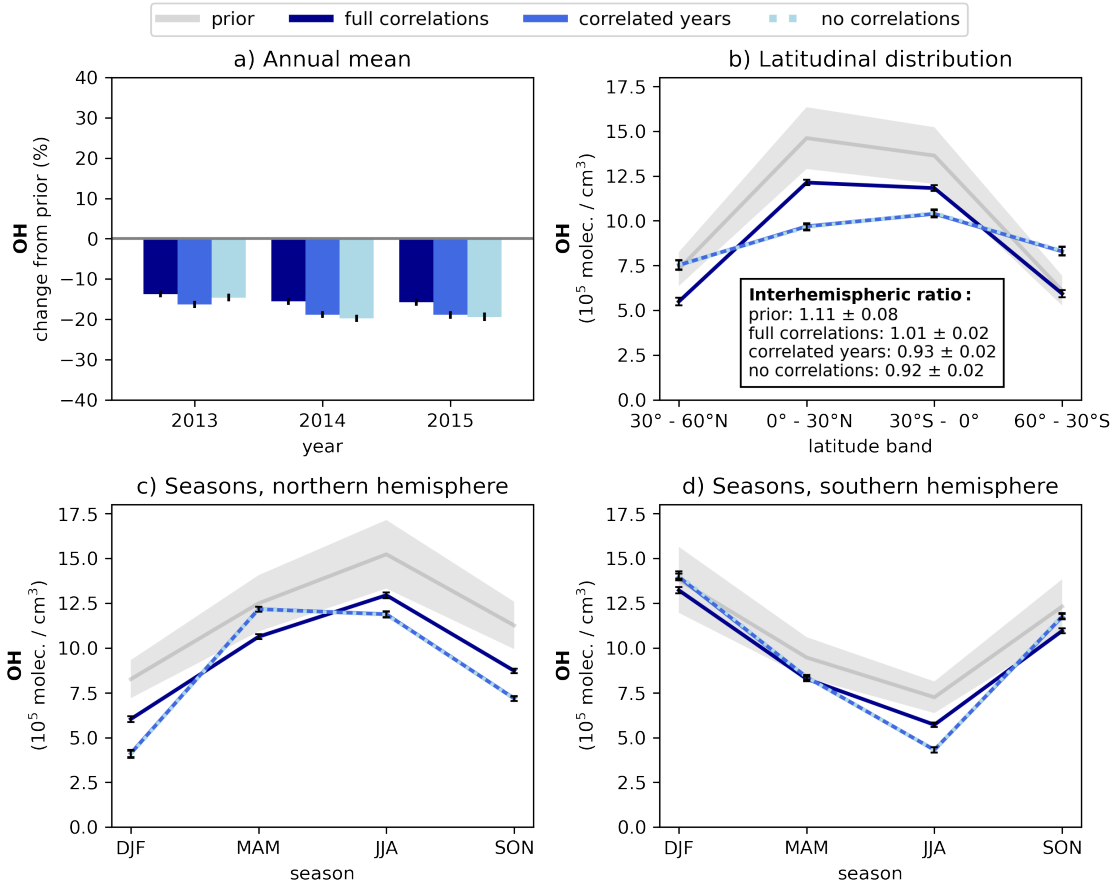
and a greater shift to the southern hemisphere. The spatial error correlations imposed by the ACCMIP models (Figure 1.3) suppress these changes in the base inversion. To the extent that the ACCMIP ensemble fairly represents error correlations on the OH distribution, ignoring that prior information results in overfit to observations. The seasonality in each hemisphere is better constrained by the observing system because there is more contrast between summer and winter, with northern and southern tropics being opposite in seasonal phase. However, we find that ignoring seasonal error correlations in the no-correlation and correlated-years inversions results in opposite corrections to OH concentrations in spring and summer of the northern hemisphere which are in fact highly correlated in the ACCMIP models (Figure 1.3).

1.5   Conclusions

We examined the ability of satellite observations of atmospheric methane to quantify different features of the tropospheric OH distribution including global multi-year mean, interannual variability in the global mean, interhemispheric ratio, intra-hemispheric latitudinal variation, and seasonality. The work was motivated by the need to find a replacement proxy for tropospheric OH as methylcholoroform (MCF) concentrations fall below detectable levels, and to explore how much information can be extracted from the satellite observations.

We used for this purpose a 3-year (2013-2015) analytical inversion of GOSAT (SWIR) and AIRS (TIR) satellite observations. SWIR observations have near-unit sensitivity for the whole atmospheric column but are limited to daytime and (mainly) land. TIR observations are sensitive mainly to the middle/upper troposphere but include nighttime and oceans.

Several previous inversions investigated the ability of satellite observations of methane to quantify the OH distribution but did not properly account for prior error correlations in that distribution. Here we provide detailed accounting of this error correlation including for global mean OH and interannual variability using MCF, and for spatial and seasonal

Figure 1.10: *Sensitivity of [OH] inversion results to the prior error correlations imposed for interannual, seasonal, and latitudinal variability. Results are shown for the 2013-2015 GOSAT-only inversion, for our base inversion with full error correlations from the ACCMIP ensemble (same results as in Figures 1.7-1.9) and for inversions with no [OH] error correlations or with [OH] error correlations for individual years only. Panels show (a) annual mean $\overline{\mathbf{OH}}$ for individual years, (b) 2013-2015 latitudinal distribution, and (c, d) 2013-2015 seasonal variations for the northern and southern hemispheres. Prior error standard deviations are shown as vertical bars and shading. The correlated-years and no-correlation inversions show the same latitudinal and seasonal variations of [OH].*

variations using the ACCMIP ensemble of 11 global atmospheric chemistry models. We find strong prior error correlations between latitude bands and seasons.

Optimizing OH concentrations from satellite observations of methane requires independent information on emissions and the SWIR observations are essential for that purpose. We find that a GOSAT-only inversion can effectively constrain global mean OH and its interannual variability independently of emissions, thus providing information comparable to MCF. Adding AIRS observations to the inversion does not significantly improve the constraint.

The ability of the inversion to resolve the latitudinal variability of OH is very limited because of strong error correlation across latitudes in the ACCMIP ensemble. Not accounting for this error correlation would result in overfit to observations. There is in particular no information on OH at mid-latitudes. The inversion provides some information on the interhemispheric OH ratio, and this is important for interpreting the corresponding gradient in methane observations (East et al., 2024). There is also some information on seasonality of OH concentrations, and the inversion confirms the prior seasonality from the ACCMIP models.

TROPOMI observations starting in May 2018 provide much denser SWIR data for methane than GOSAT (Lorente et al., 2021), allowing finer-grained quantification of emissions, but for coarse global-scale inversions as presented here the GOSAT observations offer similar information content as TROPOMI (Qu et al., 2021) and are of higher quality (Balasus et al., 2023). Beyond GOSAT and TROPOMI, the constellation of satellite observations of methane is rapidly expanding (Jacob et al., 2022), providing an effective vehicle to monitor tropospheric OH and its interannual variability in the future. This will be important for interpreting future methane trends and for improving our understanding of the factors controlling tropospheric OH. Improving the ability of the inversions to constrain the spatial variability of OH will require partnership with atmospheric chemistry models to resolve error correlations, possibly through observations of other trace gases such as CO.

1.6 Funding

Chapter 2

Remote sensing enables basin-scale inventories of coal mine methane [1]

2.1 Main

2.1.1 Introduction

Methane is a potent greenhouse gas responsible for approximately 30% of the anthropogenic warming since pre-industrial time (Szopa et al., 2021). It is emitted from a variety of sources including wetlands, agriculture, waste, oil, gas, and coal mines (Saunois et al., 2020) and is removed primarily by oxidation on a timescale of 9.1 ± 0.9 years (Szopa et al., 2021). Reducing methane emissions is a key component of climate policy including with the Global Methane Pledge (Global Methane Pledge, 2023). Global estimates of coal methane emissions range from 29 to 61 Tg a^{-1}, accounting for approximately 10% of total anthropogenic emissions (Saunois et al., 2020). Here we show the potential for remote sensing data to improve current estimates of coal mine emissions, using observations over the United States (U.S.) for demonstration.

Underground coal mines emit methane co-present with coal in sufficient quantity that it

---

[1]Co-authors: Daniel J. Jacob, Kate Howell, Kelly O'Neill, Tia Scarpelli, Zichong Chen, Robert A. Field, C. Özgen Karacan, Elfie Roy, Daniel Cusworth

must be forcibly ventilated to ensure safety (Karacan et al., 2024). While emissions from surface mining may be underreported (Borchardt et al., 2025), underground mines are generally recognized as the most important source of coal methane emissions (Kirchgessner et al., 2000). Methane emissions from underground mining result from both the coal seam being actively mined and the gob (caved and fractured strata above and below the seam), together known as the gas emission zone (GEZ) (Creedy, 1993). Methane is emitted from ventilation shafts and gob wells. Ventilation shafts exhaust mine air with relatively dilute methane (concentrations generally <1%). Gob wells capture methane still in the strata above gassy mines and emit concentrated methane that can be flared or recovered (Karacan et al., 2024).

There are 187 active underground coal mines in the U.S.; of these, 62 emit >700 t a^{-1} and are required to report to the EPA GHGRP (U.S. Environmental Protection Agency Greenhouse Gas Reporting Program). The EPA national GHGI (Greenhouse Gas Inventory) compiles measured emissions on a quarterly (ventilation shafts) and weekly (gob wells) basis at all active underground coal mines in the U.S., either from the GHGRP for reporting mines (96% of emissions) or directly from MSHA (Mine Safety and Health Administration) inspections for non-reporting mines (4%) (U.S. EPA, 2024). All of these mines have ventilation shaft emissions, while only 13 mines report gob well emissions. According to the 2022 GHGI, 77% of underground coal mine emissions in the U.S. are from ventilation shafts, 13% are from gob wells, and 10% are from post-mine processing (U.S. EPA, 2024). Temporal variability of ventilation shaft emissions is relatively small, so that the instantaneous measurements are estimated to capture the quarterly mean emissions within 20-30% (Mutmansky and Wang, 2000; Swolkień et al., 2024).

Individual countries must report their annual methane emissions to the United Nations Framework Convention on Climate Change (UNFCCC). But most countries lack direct measurements of emissions from underground coal mines, and instead rely on bottom-up methods recommended by the IPCC (International Panel on Climate Change) to develop inventories. Emissions depend on coal production rates (Kissell et al., 1973) but may also

31
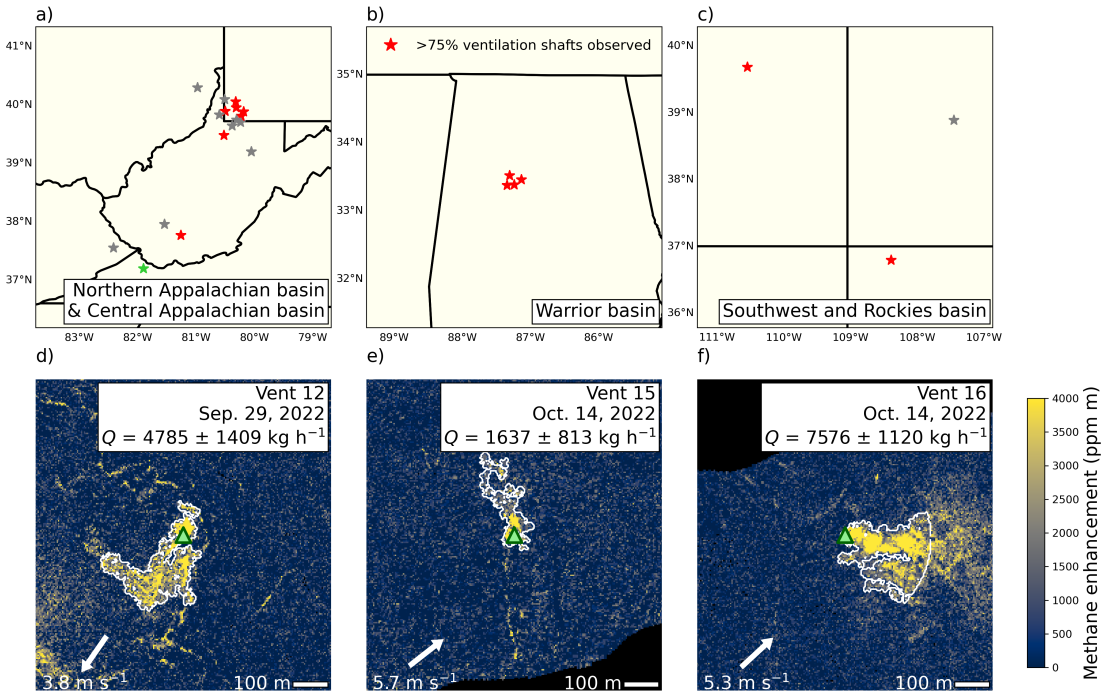
depend on mine gas content, mine depth, and operations (Karacan, 2023; Karacan et al., 2024; Swolkień et al., 2022). The IPCC recommends that countries estimate their emissions using emission factors applied to coal production. These recommendations range from Tier 1 (simplified) to Tier 3 (more detailed and greater accuracy). Tier 1 uses default global emission factors based on mine depth, Tier 2 uses country- or basin-specific emission factors, and Tier 3 (such as the US GHGI) uses direct, mine-specific measurements (IPCC, 2006). The Global Coal Mine Tracker inventory of the Global Energy Monitor (2024) uses an alternative method, MC2M (Model for Calculating Coal Mine Methane), which uses mine depth and coal rank to estimate emission factors for coal mine methane worldwide (Kholod et al., 2020).

Coal can be classified, with increasing rank, as lignite, sub-bituminous, bituminous, or anthracite. Higher rank coals are associated with greater gas content. However, the gas content of coal can vary to a greater extent between basins than between different mine depths or coal rank, leading to biases in inventories where basin-specific gas content is not accounted for (Irving and Tailakov, 2019). Broad rank classifications do not reflect the observed compositional complexity of coal (Karacan et al., 2024).

Aircraft and satellite remote sensing has been widely used to quantify methane emissions from point sources (Duren et al., 2019; Jacob et al., 2022). It is well-suited for quantifying emissions from underground coal mines, where methane is released at a small number of large point sources (Cusworth et al., 2022). Several studies have inferred coal mine emissions from satellite observations of methane plumes (Han et al., 2024; Karacan et al., 2025; Sadavarte et al., 2021; Varon et al., 2020).

In this paper we demonstrate the potential of remote sensing for improving bottom-up inventory estimates of coal mine emissions on regional/national scales, using the U.S. as a test case. We use a Carbon Mapper aircraft survey of 24 underground mines in the U.S. (representing 39% of underground mine emissions reported to the GHGRP) with the Next-Generation Airborne Visible Infrared Imaging Spectrometer (AVIRIS-NG) and the Global Airborne Observatory (GAO). We first compare the Carbon Mapper survey data to

Figure 2.1: *Carbon Mapper aircraft surveys of coal mine methane plumes in the U.S., 2020-2022. The top row (a-c) shows the surveyed mines. Red stars indicate mines for which >75% of ventilation shafts were observed in any one quarter, and gray stars indicate mines where at least one ventilation shaft or gob well was observed. Panels d-f show three plumes from individual vents (green triangles) of a mine in Central Appalachia (green star), with source rates Q (best estimates and error standard deviations) inferred from the plumes; white contours indicate the plume boundaries used for quantification (see Materials and Methods), with wind direction and speed from HRRR (NOAA High Resolution Rapid Refresh Model; NOAA, n.d.). White arrows show direction of air flow. See Figure B.1 for comparison of these plumes to daily in-mine measurements and GHGRP. As a condition of our data agreement with this mine, we cannot name the mine.*

the GHGRP data, based on direct measurements. We then use the GHGRP data to evaluate the IPCC Tier 1, IPCC Tier 2, and MC2M estimation methods, and develop an improved IPCC Tier 2 method informed by Carbon Mapper observations.

2.1.2 Results and Discussion
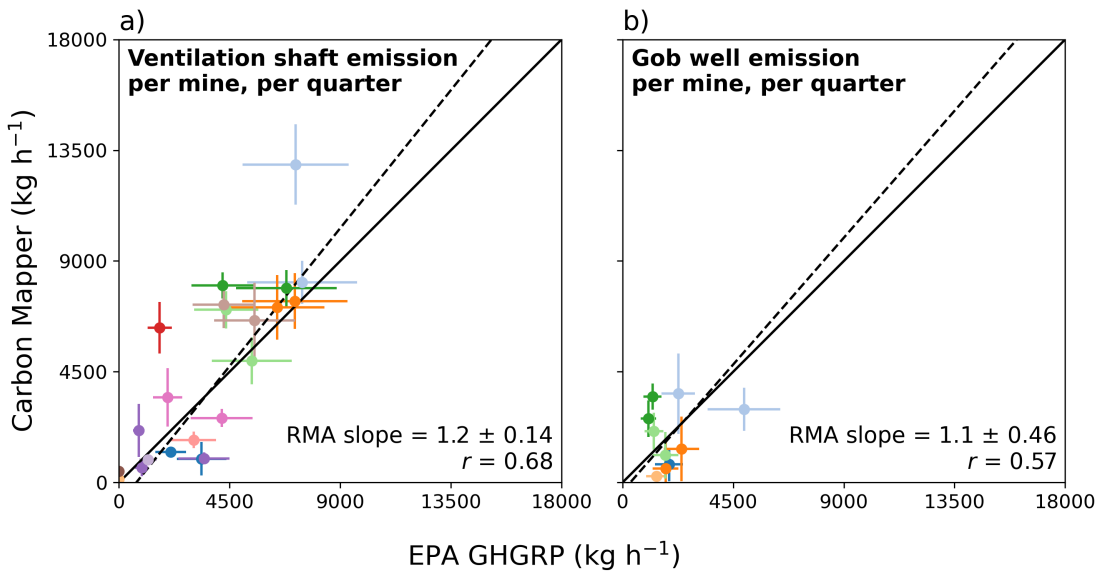
Figure 2.1 shows the locations of Carbon Mapper aircraft surveys of coal mine methane plumes. These surveys observed over 75% of ventilation shafts for 13 of the mines in a given quarter, enabling comparisons with the EPA GHGRP. Illustrative plumes are shown from

individual ventilation shafts for a Central Appalachia mine in Buchanan County, Virginia. We quantify source rates from the plumes using the Integrated Mass Enhancement (IME) method (see Data and Methods). Carbon Mapper aircraft surveys detect 90% of plumes from point sources of magnitude 10-45 kg h^{-1} in controlled release experiments (Ayasse et al., 2024).

Figure 2.2 compares total emissions measured from the aircraft surveys at each mine for which > 75% of the ventilation shafts listed in the GHGRP were surveyed in the same quarter to the corresponding quarterly GHGRP data. 1-3 quarters between 2020-2022 were compared for each mine (Table B.1). We find good agreement with the GHGRP (within 20%) for ventilation shafts, even when not all shafts were observed, because emissions are concentrated at one or two methane bleeder shafts (ventilation shafts located over the active part of the mine). Only 6 of the mines vent methane from gob wells; at the remaining mines, either there are no gob wells, or the methane from gob wells is recovered and sent to market. Consistent with the GHGRP, we find that gob wells account for about 25% of emissions from mines which vent gob well methane, and we find no emissions at mines reporting 100% gob gas recovery.

The good consistency between the GHGRP and Carbon Mapper emission estimates gives us more confidence in both. We proceed to use the GHGRP data (IPCC Tier 3) to evaluate the IPCC Tier 1, IPCC Tier 2, and MC2M bottom-up inventory methods as they would be applied to the U.S. Countries following IPCC Tier 1 select from a low, medium, or high emission factor based on the depth of the mine (IPCC, 2006). Countries following IPCC Tier 2 use country- or basin-specific emission factors, and here for application to the U.S. we will use basin-specific measurements of gas content to derive emission factors.

Table 1 shows the methodologies used by the ten countries with the largest amount of coal methane emissions reported to the UNFCCC. These ten countries account for 94% of coal emissions in the UNFCCC reports (Scarpelli et al., 2022). Four countries, including the U.S., use a Tier 3 methodology (directly measured emissions), and one country (Kazakhstan) uses Tier 1. Five countries use a Tier 2 methodology, including China, the largest emitter of

Figure 2.2: *Emissions from individual U.S. mines. Carbon Mapper emission estimates from aircraft remote sensing taken over 2020-2022 are compared to the quarterly GHGRP data. For each mine, we first average all Carbon Mapper emission measurements taken at each piece of infrastructure (ventilation shaft or gob well), and sum emissions at each mine. We only include the 13 mines for which > 75% of the ventilation shafts listed in the GHGRP were surveyed in the same quarter. We propagate errors on Carbon Mapper mine-level estimates from the errors on individual plumes and assume a 30% error for the EPA GHGRP quarterly measurement (Mutmansky and Wang, 2000). The 1:1 line and reduced-major-axis (RMA) regression lines are shown, with Pearson's correlation coefficient (r) and RMA slopes given inset, and error standard deviation on the slopes from bootstrap resampling.*

coal mine methane. Collectively, Tier 2 methodologies account for over 80% of the Global Stocktake of coal mine methane.

While there is a wide variation in the contribution of underground mining to total production in Table 1, underground mining is generally accepted as the dominant source of emissions in most countries (United Nations Economic Commission for Europe, 2016). However, there are large uncertainties on surface coal mine emissions, as there is no Tier 3 method for surface mines. Recent airborne research has shown emissions 3-8x higher than those reported for the Hail Creek mine in Australia (Borchardt et al., 2025).

The IPCC Tier 1 and Tier 2 recommendations assume that emissions (E) are proportional to coal production:

$$E = EF \times P \qquad (2.1)$$

where EF is the emission factor (kg methane / t coal) and P is the coal production in metric tons (t). IPCC Tier 1 specifies emissions factors (EF) for three mine depth ranges (IPCC, 2006) as shown in Figure 2.3. We consider two configurations of Tier 2 inventories derived from the gas content of the mines, MC2M and a basin-specific estimate, with emission factors (EF):

$$EF = C_{EF} \times G \qquad (2.2)$$

where G is the methane gas content of the mined coal (kg methane / t coal) and C_{EF} is the emission factor coefficient, or the fraction of methane in mined coal that is emitted. A C_{EF} value of 1 indicates that 100% of the methane within the mined coal is emitted. C_{EF} is typically greater than 1 because of methane emitted from the gob (Ju et al., 2016; Kholod et al., 2020; Kirchgessner et al., 2000). We use $C_{EF} = 1.9$ after Kholod et al. (2020), who inferred C_{EF} for the U.S. from the average ratio of $G \times P$ to mine emissions from the GHGRP. Globally, C_{EF} is thought to range from 1.3 to 2.0 (Ju et al., 2016), and the Global Energy Monitor (2024) uses a C_{EF} of 1.6.

The two Tier 2 inventories considered here differ only in their choice of G. For the

Table 2.1: *IPCC Reporting Method for Top 10 Coal Mine Methane Emitting Countries*

Country	Coal Emission (Tg a^{-1})[1]	Coal Production (Tg a^{-1})[2]	Underground Production (%)[3]	IPCC Method[6]
China	21	3846	75%[4]	Tier 2 (Country)[7]
Russia	2.73	437	24%	Tier 2 (Basin)[8]
US	2.13	641	38%	Tier 3
South Africa	1.18	258	63%	Tier 2 (Country)[9]
Australia	0.90	512	17%	Tier 3
India	0.88	730	6%[5]	Tier 2 (Gassiness)[10]
Poland	0.58	112	55%	Tier 3
Ukraine	0.50	26	100%	Tier 3
Colombia	0.35	87	9%	Tier 2 (Basin)[11]
Kazakhstan	0.28	98	10%	Tier 1
Total	**30.53**	**6747**		
Global Total	**32.4**	**8014**		

[1] Emission for 2019 as reported to the UNFCCC (Scarpelli et al., 2022). Includes all coal emissions (underground mines, surface mines, and post-mine processing) as most countries do not separate contributions in their final reporting. Emissions are mainly from underground mines.

[2] Production data for 2019 (U.S. Energy Information Administration, 2025). Includes both underground and surface mines.

[3] Fraction of total national production contributed by underground mines. Data from 2024 UNFCCC National Inventory Reports (NIR) for Annex I countries or 2022 Biennial Update Reports (BUR) for non-Annex I countries, unless otherwise noted.

[4] Per Gao et al. (2021) for 2019.

[5] Indian Ministry of Coal, 2023.

[6] Method used for underground coal mines in a country's NIR (Annex I) or BUR (non-Annex I). Tier 2 emission factors may be basin-specific, country-specific, or based on some other classification chosen by the country. Countries use separate underground and surface mine calculations, but not all countries report them separately.
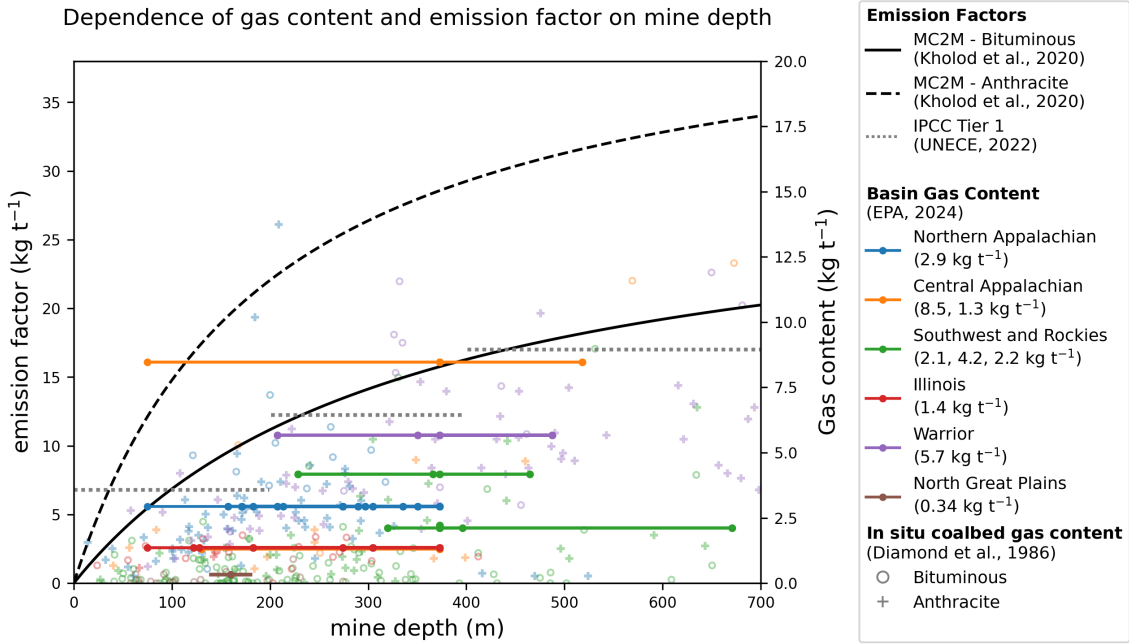
[7] China uses one country-wide emission factor estimated from the State Administration of Coal Mine Safety classification of mines (Gao et al., 2020).

[8] Emission factors from Tailakov et al., 2009.

[9] Emission factors from Lloyd, 2008.

[10] Emission factors for mines in India are based on gassiness of the mine, from Singh et al. (2022).
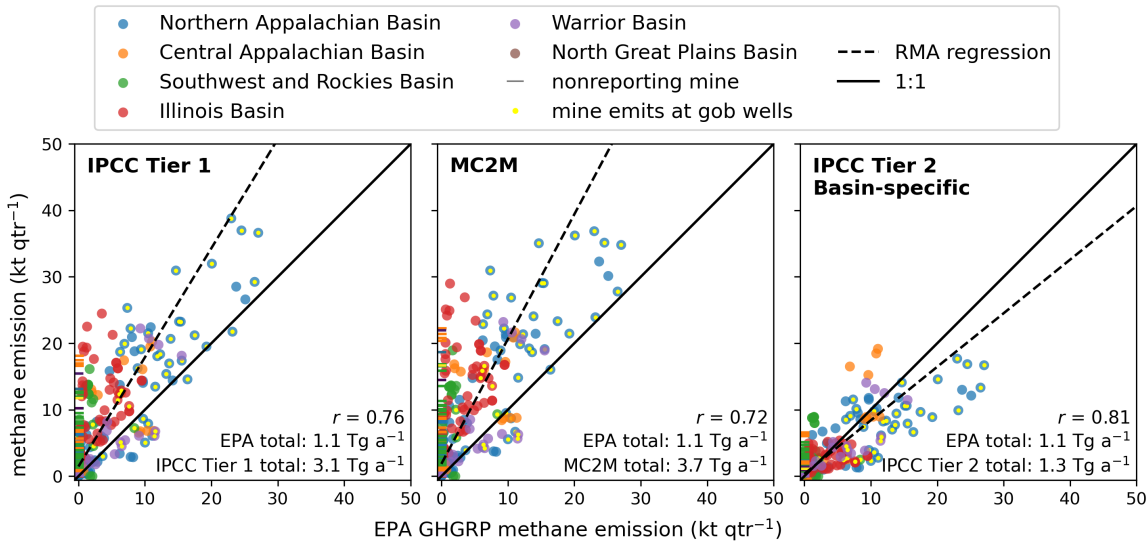
[11] Emission factors from Amell et al. (2016).

Figure 2.3: *Coal mine emission factors and gas content in U.S. coalbeds as a function of mine depth. Gas content and emission factor are related by the emission factor coefficient C_{EF} (equation (2)), which we take here to be 1.9. Values are shown for (1) the IPCC Tier 1 method (United Nations Economic Commission for Europe, 2022), (2) the MC2M method (Kholod et al., 2020), (3) 1460 individual coal-bed measurements colored by basin and averaged by 200 m depth intervals from Diamond et al. (1986), and (4) the average basin-scale gas content of mined coal (U.S. Environmental Protection Agency, 2024) represented as thick horizontal lines with dots representing the depths of individual mines.*

basin-specific inventory, we use *G* from the average measured gas content of mined coals for each basin as given by the U.S. EPA (2024) and compiled from measurements by Diamond et al. (1986) and others (U.S. Department of Energy, 1983), shown in Figure 2.3. MC2M estimates gas content as a function of mine depth and coal rank using a Langmuir saturation profile derived from a global database of coal gas content, rank, and depth (Kholod et al., 2020). Emission factors and gas contents from the different methods are shown in Figure 2.3 as a function of mine depth. All but 6 underground mines in the U.S. produce bituminous rank coal.

Figure 2.3 shows that the gas contents implied by the Langmuir profile (MC2M) and the IPCC Tier 1 emission factors are systematically too high. High variability between the gas contents of individual coal beds in the direct measurements is observed, and no significant

Figure 2.4: *Comparison of IPCC Tier 1, MC2M, and IPCC Tier 2 bottom-up inventory methods applied to the U.S. to the actual emissions reported to the GHGRP in 2022 for individual mines labeled by basins. Inventory estimates are calculated using Eq. 2.1 and Eq. 2.2 with emission factors in Fig 2.3. Each symbol represents quarterly emissions as reported to the GHGRP. The mines emitting less than 0.7 kt a^{-1} are not required to report to the GHGRP and are shown as colored dashes on the y axis. RMA (reduced major axis) regressions for GHG-reporting mines are shown as dashed lines. Total emissions and correlation coefficients are inset.*

dependence on mine depth is evident, unlike the IPCC Tier 1 and MC2M methods.
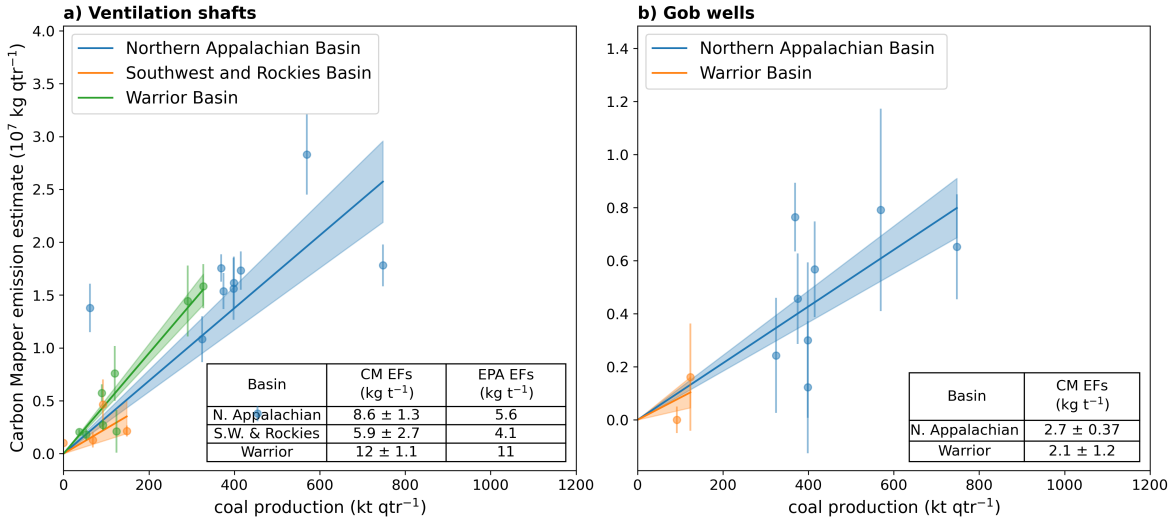
Figure 2.4 compares the three bottom-up inventory methods to the GHGRP for individual U.S. mines. IPCC Tier 1 and MC2M overestimate U.S. methane emissions by a factor of three, primarily due to large overestimates of gas content in the Illinois basin and the Southwest and Rocky Mountain basin, where mines are relatively deep (in many cases more than 300 m), but the coal has a low gas content (Table B.1, Fig 2.3). Using a lower C_{EF} for these inventories could correct the national-scale bias, but at the cost of predictive power, especially if coal production shifts towards gassier basins, a trend already underway in the U.S. (U.S. EPA, 2018). The basin-specific Tier 2 method using mean measured gas content for individual basins largely avoids the bias from the Tier 1 and MC2M methods. Emissions for mines with gob wells are underestimated by 30%, but this underestimation reduces to 3% if we compare only to ventilation shafts (Figure B.3). The strata drained by gob wells are different from the mined strata included in the basin-scale gas content database. This implies that different emission factors are needed for gob wells and ventilation shafts.

Based on the comparison of these different bottom-up inventory methods with the GHGRP data, we conclude that 1) it is important to use basin-specific gas content based on representative measurements, and 2) it is important to use separate emission factors for ventilation shafts and gob wells. However, direct measurements of gas content may not be available in all cases. Additionally, gob wells may represent a larger portion of emissions outside the U.S., where recovery rates at gob gas wells are lower; for example, recovery rates are below 50% in China and 30% in Poland, as compared to 83% for the U.S. (Ju et al., 2016; Swolkień et al., 2022; U.S. Environmental Protection Agency, 2018). In regions where gob wells contribute more to national emissions, there is potential for greater biases using emission estimates which ignore the contribution from gob wells.

We propose here an alternative Tier 2 method for underground coal mine emissions by inferring individual basin gas contents from remote sensing of methane plumes (as from Carbon Mapper) and including separate emission factors (kg t^{-1}) for ventilation shafts and gob wells. We estimate coal mine emissions using separate emission factors (kg t^{-1}) for ventilation shafts and gob wells:

$$E = (EF_V + \delta_W EF_W) \times P \tag{2.3}$$

where EF_V is for ventilation shafts, EF_W is for gob wells, and δ_W (0 or 1) indicates whether gob well methane is recovered. In the U.S., mines typically collect methane from gob wells unless the concentration is too low to flare or send to market. This occurs when the roof of the mine caves completely (known as supercritical conditions), which allows mine air to mix with gob well air (Karacan et al., 2024). Supercritical conditions in the U.S. typically occur when the ratio of longwall width (W) over mine depth (D) is greater than 1.2 (Karmis et al., 1990). We use W and D for the U.S. from the U.S. Longwall census (Coal Age, 2024) to classify mines as super- and subcritical, and find that gob well emissions from supercritical mines are much higher than subcritical mines. We therefore classify δ_W for the U.S. as follows:

Figure 2.5: *Derivation of emission factors (EFs) for ventilation shafts and gob wells (supercritical conditions) in U.S. basins using Carbon Mapper (CM) aircraft remote sensing observations. The EFs are obtained by linear regression of observed emissions versus coal production for individual mines in a given quarter (symbols), with error standard deviations on the regression slope obtained by bootstrap sampling. Only mines where >75% of ventilation shafts were observed are included. Ventilation shaft EFs are compared inset to EPA EFs based on gas content from U.S. EPA (2024) as shown in Figure 2.3 and assuming $C_{EF} = 1.9$. For the Southwest and Rockies basin we include only the average emission factor of mines in New Mexico and Utah, where Carbon Mapper fully surveyed mines (see Table B.1 for all gas contents).*

$$\delta_W = \begin{cases} 1, & \text{if } \dfrac{W}{D} > 1.2 \text{ and } N_W > 0 \\ 0, & \text{otherwise} \end{cases} \qquad (2.4)$$

where N_W is the number of gob wells at the mine. Application outside the U.S. would require knowledge of gob well gas recovery practices. Alternatively, it could be assumed as a conservative estimate that there is no gas recovery from gob wells so that $\delta_W = 1$.

Figure 2.5 shows the derivation of ventilation shaft (EF_V) and gob well (EF_W) emission factors for the 13 mines in three U.S. basins where Carbon Mapper had extensive aircraft surveys. These observations can be applied to determine emission factors for our alternative Tier 2 method, as demonstrated here with the U.S. where we have ample surveys. We find that the basin-level emission factors for ventilation shafts derived from Carbon Mapper observations are generally consistent with the basin-level emission factors based on gas content of mined coal (U.S. EPA, 2024). This is despite surveying only a fraction of

41

underground mines in the Northern Appalachian (5%), Warrior (67%), and Southwest and Rockies (18%) basins. This success in estimating emission factors with relatively few mines reflects two characteristics of coal mine methane emissions: first, the majority of coal mine emissions come from the largest emitters (these 13 mines accounted for 22% of all U.S. underground coal emissions in 2022), and second, emission factors are similar for mines within the same basin (Figure 2.3). We apply these remote-sensing derived emission factors via Equation 2.3 to estimate mine-level and basin level emissions. We find that this remote-sensing informed approach shows closer agreement with basin-specific IPCC Tier 2 estimates (10-54%) than IPCC Tier 1 (24-53%) or MC2M (27-60%) estimates (Figure B.2).

In summary, we showed that quarterly Carbon Mapper emission estimates for 13 U.S. mines from aircraft remote sensing are consistent, within 20%, with direct measurements reported to the U.S. EPA GHGRP, for both ventilation shafts and gob wells. Most coal-emitting nations do not have the direct measurements like those in GHGRP and instead rely on estimates of emission factors per unit of coal production. We evaluated the IPCC Tier 1, IPCC Tier 2 (basin-specific gas content information), and MC2M methods in comparison with GHGRP data for the U.S. and found that the IPCC Tier 1 and MC2M overestimate emissions by a factor of three due to erroneous dependence on mine depth. The IPCC Tier 2 method using observed basin-scale mine gas content successfully reproduces the GHGRP observations, albeit with a 30% low bias for gob well emissions, but it requires gas content information that may not be locally available. We proposed a new basin-scale Tier 2 method to quantify gas content on the basis of remote sensing of methane plumes, with separate emission factors for ventilation shaft and gob well emissions. We showed how Carbon Mapper aircraft surveys can infer basin-scale gas contents for this new Tier 2 method by sampling a small fraction of the mines. Coal mine emissions are sufficiently high to be detected from satellite point source imagers such as Tanager-1 (Carbon Mapper) and GHGsat (Jervis et al., 2021). These next-generation satellite datasets have the potential to provide remote sensing-informed inventories of coal mine emissions.

2.1.3 Data and Methods

Carbon Mapper surveyed 24 underground coal mines using AVIRIS-NG and GAO from 2020 to 2022 in Southwest Pennsylvania, West Virginia, Virginia, Alabama, New Mexico, and Colorado. AVIRIS-NG and GAO measure solar backscatter in the 380 - 2500 nm wavelength range at 5 nm spectral resolution. Methane enhancements over background are retrieved in the 2100 - 2500 nm spectral range at approximately 3x3 m^2 spatial resolution using a dynamic unit absorption spectrum matched filter described in Foote et al. (2021). Emission rates and corresponding uncertainties are calculated from the integrated mass enhancements (IME) in the plumes following the approach described by Ayasse et al. (2024). Controlled release experiments indicate a minimum detection limit of 9-10 kg h^{-1} (90% probability of detection 10-45 kg h^{-1}) depending on the local observing conditions (Ayasse et al., 2023). We apply Carbon Mapper's standard quality control process, which eliminates plumes that cannot be accurately quantified by IME (Cusworth et al., 2025). 20% of detected plumes were removed by this process.

We attribute coal mine methane plumes to specific mines using maps of permits as available from state agencies. We classify each plume location as a ventilation shaft or gob well based on imagery from Google Earth. Plumes with origins within 150 m of a well or shaft are attributed to that piece of infrastructure; when we observe the same location multiple times in the same quarter, we average emission rates and propagate error estimates assuming that each detection is independent. In 70% of cases, there were either 1 or 2 Carbon Mapper observations at a single ventilation shaft or well in a single quarter. Surveys at each mine took place during 1-3 quarters in 2020-2022. See Table B.3 for a dates of aircraft surveys at each basin, and Table B.4 for all quantified plumes.

To estimate mine-level emissions, we sum the quarterly ventilation shaft and gob well emissions at each mine. We only report emissions at mines where more than 75% of the ventilation shafts at the mine were observed by the aircraft survey in a single quarter. Missing ventilation shafts will bias our estimate low; however, coal mine emissions are typically concentrated at one or two main shafts. We determine the number of ventilation

shafts from the EPA GHGRP, and at mines where measurements for a single shaft are split across multiple locations, we find the number of ventilation shafts by using the names of each measurement location. Each emission rate quantified by Carbon Mapper has an associated uncertainty. We propagate these measurement uncertainties to the mine-level emission estimate, assuming each plume detection is independent.

We compare the Carbon Mapper measurements for individual mines (separately for ventilation shafts and gob wells) to the U.S. EPA GHGRP measurements reported in the same quarter. GHGRP emissions from ventilation shafts are estimated by multiplying the measured concentration in the ventilation shaft (from an instantaneous vacuum bottle sample) by the air flow velocity (from a vane anemometer in the airway). The combined instrument error and error incurred from using instantaneous measurements to estimate quarterly mean emissions is estimated at 30% (Mutmansky and Wang, 2000). We access the 2011-2023 GHGRP data for ventilation shafts and gob wells at 62 individual mines from the Envirofacts API (https://www.epa.gov/enviro/envirofacts-data-service-api, accessed December 2024).

Our calculations of coal mine emissions using bottom-up inventory methods require information on coal production, mine depth, and coal rank for each mine. We obtain quarterly coal production for individual mines from the MSHA Mines Dataset (https://www.msha.gov/data-and-reports/mine-data-retrieval-system, accessed August 2024), mine depths from the U.S. Longwall Census (Coal Age, 2024), and coal rank and mine depths not available in the longwall census for each mine from Global Energy Monitor's (GEM) Global Coal Mine Tracker (GCMT) (https://globalenergymonitor.org/projects/global-coal-mine-tracker/, accessed April 2024). We estimate emissions at all 187 active and producing underground mines in the MSHA Mines Dataset in 2023. Four mines are in the MSHA mines dataset but missing from both the Longwall Census and the Global Energy Monitor Global Coal Mine Tracker; for these mines we assume the average mine depth in the U.S. (373 m) and bituminous coal rank.

To classify gob well emission conditions as super- or subcritical, our new Tier 2 method

44

requires longwall width and mine depth, as well as whether there are gob wells at the mine. We get width and depth from the U.S. Longwall Census (Coal Age, 2024), which has data on 14 of the 17 mines with gob wells in the basins we where we estimate emissions. The remaining 3 mines (Heilwood, Lowry, and Beckley Pocahontas) are in the Northern Appalachian basin; because all other mines with gob wells in the Northern Appalachian basin are supercritical, we assume these mines are as well. We determine whether there are gob wells at the mine using the gob well count reported to the GHGRP.

In our comparisons between inventories and the GHGRP, we use RMA regression and bootstrap resampling. RMA regression accounts for uncertainty on both the independent and dependent variables (McArdle, 1988). To calculate errors, we perform RMA on 1000 bootstrapped (resampled with replacement) datasets and take the standard deviation of the resulting slopes.

2.2 Data Availability

Carbon Mapper emission estimates for each plume and ventilation shaft and gob well locations are available in the Supplementary Information of this paper. Code is available upon request. GHGRP data is available at https://www.epa.gov/enviro/envirofacts-data-service-api (accessed December 2024).

2.3 Acknowledgments.

References

[1] Amell Arrieta, A., Janna, F. C., Lopez, D. L., Forero, C., Herrera, B., Torres, P. A., Marin, C. M. C., Restrepo, S. Y. G., and Lopez, J. P.: Consultoria tecnica para el fortalecimiento y mejora de la base de datos de Factores de Emisios de los Combustibles Colombianos (FECOC), 2016.

[2] Anderson, D. C., Duncan, B. N., Fiore, A. M., Baublitz, C. B., Follette-Cook, M. B., Nicely, J. M., and Wolfe, G. M.: Spatial and temporal variability in the hydroxyl (OH) radical: understanding the role of large-scale climate features and their influence on OH through its dynamical and photochemical drivers, Atmos. Chem. Phys., 21, 64816508, https://doi.org/10.5194/acp-21-6481-2021, 2021.

[3] Ayasse, A. K., Cusworth, D. H., Howell, K., ONeill, K., Conrad, B. M., Johnson, M. R., Heckler, J., Asner, G. P., and Duren, R.: Probability of Detection and Multi-Sensor Persistence of Methane Emissions from Coincident Airborne and Satellite Observations, Environ. Sci. Technol., 58, 2153621544, https://doi.org/10.1021/acs.est.4c06702, 2024.

[4] Ayasse, A. K., Cusworth, D., ONeill, K., Fisk, J., Thorpe, A. K., and Duren, R.: Performance and sensitivity of column-wise and pixel-wise methane retrievals for imaging spectrometers, Atmos. Meas. Tech., 16, 60656074, https://doi.org/10.5194/amt-16-6065-2023, 2023.

[5] Bloom, A. A., Bowman, K. W., Lee, M., Turner, A. J., Schroeder, R., Worden, J. R., Weidner, R. J., McDonald, K. C., and Jacob, D. J.: CMS: Global 0.5-deg Wetland Methane Emissions and Uncertainty (WetCHARTs v1.0), , https://doi.org/10.3334/ORNLDAAC/1502, 2017.

[6] Boesch, H., Baker, D., Connor, B., Crisp, D., and Miller, C.: Global Characterization of CO2 Column Retrievals from Shortwave-Infrared Satellite Observations of the Orbiting Carbon Observatory-2 Mission, Remote Sensing, 3, 270304, https://doi.org/10.3390/rs3020270, 2011.

[7] Borchardt, J., Harris, S. J., Hacker, J. M., Lunt, M., Krautwurst, S., Bai, M., Bosch, H., Bovensmann, H., Burrows, J. P., Chakravarty, S., Field, R. A., Gerilowski, K., Huhs, O., Junkermann, W., Kelly, B. F. J., Kumm, M., Lieff, W., McGrath, A., Murphy, A., Schindewolf, J., and Thoboll, J.: Insights into Elevated Methane Emissions from an Australian Open-Cut Coal Mine Using Two Independent Airborne Techniques, Environ. Sci. Technol. Lett., acs.estlett.4c01063, https://doi.org/10.1021/acs.estlett.4c01063, 2025.

[8] Bousquet, P., Hauglustaine, D. A., Peylin, P., Carouge, C., and Ciais, P.: Two decades of OH variability as inferred by an inversion of atmospheric transport and chemistry of methyl chloroform, Atmospheric Chemistry and Physics, 5, 26352656, https://doi.org/10.5194/acp-5-2635-2005, 2005.

[9] Coal Age: US Longwall Census, 2024.

[10] Corbett, A., Jiang, X., Xiong, X., Kao, A., and Li, L.: Modulation of midtropospheric methane by El Nino: Modulation of Methane by El Nino, Earth and Space Science, 4, 590596, https://doi.org/10.1002/2017EA000281, 2017.

[11] Creedy, D. P.: Methane emissions from coal related sources in Britain: Development of a methodology, Chemosphere, 26, 419439, https://doi.org/10.1016/0045-6535(93)90435-8, 1993.

[12] Crippa, M., Guizzardi, D., Muntean, M., Schaaf, E., Dentener, F., van Aardenne, J. A., Monni, S., Doering, U., Olivier, J. G. J., Pagliari, V., and Janssens-Maenhout, G.: Gridded Emissions of Air Pollutants for the period 1970-2012 within EDGAR v4.3.2, Data, Algorithms, and Models, https://doi.org/10.5194/essd-2018-31, 2018.

[13] Cusworth, D. H., Thorpe, A. K., Ayasse, A. K., Stepp, D., Heckler, J., Asner, G. P., Miller, C. E., Yadav, V., Chapman, J. W., Eastwood, M. L., Green, R. O., Hmiel, B., Lyon, D. R., and Duren, R. M.: Strong methane point sources contribute a disproportionate fraction of total emissions across multiple basins in the United States, Proc. Natl. Acad. Sci. U.S.A., 119, e2202338119, https://doi.org/10.1073/pnas.2202338119, 2022.

[14] Cusworth, D., Ayasse, A. K., Duren, R., Lai-Norling, J., Huffman, M., and Diamond, A.: Carbon Mapper Quality Control Description Document v1.0.1, 2025.

[15] Diamond, W. P., LaScola, J. C., and Hyman, D. M.: Results of Direct- Method Determination of the Gas Content of U.S. Coalbeds, Bureau sf Mines Information Circular, 1986.

[16] Duren, R. M., Thorpe, A. K., Foster, K. T., Rafiq, T., Hopkins, F. M., Yadav, V., Bue, B. D., Thompson, D. R., Conley, S., Colombi, N. K., Frankenberg, C., McCubbin, I. B., Eastwood, M. L., Falk, M., Herner, J. D., Croes, B. E., Green, R. O., and Miller, C. E.: Californias methane super-emitters, Nature, 575, 180184, https://doi.org/10.1038/s41586-019-1720-3, 2019.

[17] East, J. D., Jacob, D. J., Balasus, N., Bloom, A. A., Bruhwiler, L., Chen, Z., Kaplan, J. O., Mickley, L. J., Mooring, T. A., Penn, E., Poulter, B., Sulprizio, M. P., Worden, J. R., Yantosca, R. M., and Zhang, Z.: Interpreting the Seasonality of Atmospheric Methane, Geophysical Research Letters, 51, e2024GL108494, https://doi.org/10.1029/2024GL108494, 2024.

[18] Etiope, G., Ciotoli, G., Schwietzke, S., and Schoell, M.: Gridded maps of geological methane emissions and their isotopic signature, Earth System Science Data, 11, https://doi.org/10.5194/essd-11-1-2019, 2019.

[19] Foote, M. D., Dennison, P. E., Sullivan, P. R., ONeill, K. B., Thorpe, A. K., Thompson, D. R., Cusworth, D. H., Duren, R., and Joshi, S. C.: Impact of scene-specific enhancement spectra on matched filter greenhouse gas retrievals from imaging spectroscopy, Remote Sensing of Environment, 264, 112574, https://doi.org/10.1016/j.rse.2021.112574, 2021.

[20] Gao, J., Guan, C., and Zhang, B.: Chinas CH4 emissions from coal mining: A review of current bottom-up inventories, Science of The Total Environment, 725, 138295, https://doi.org/10.1016/j.scitotenv.2020.138295, 2020.

[21] Gao, J., Guan, C., Zhang, B., and Li, K.: Decreasing methane emissions from Chinas coal mining with rebounded coal production, Environ. Res. Lett., 16, 124037, https://doi.org/10.1088/1748-9326/ac38d8, 2021.

[22] Gaubert, B., Worden, H. M., Arellano, A. F. J., Emmons, L. K., Tilmes, S., Barre, J., Martinez Alonso, S., Vitt, F., Anderson, J. L., Alkemade, F., Houweling, S., and Edwards, D. P.: Chemical Feedback From Decreasing Carbon Monoxide Emissions, Geophys. Res. Lett., 44, 99859995, https://doi.org/10.1002/2017GL074987, 2017.

[23] Global Energy Monitor: Estimating methane emissions from coal mines, 2024.

[24] Global Methane Pledge: Global Methane Pledge, 2023.

[25] Han, G., Pei, Z., Shi, T., Mao, H., Li, S., Mao, F., Ma, X., Zhang, X., and Gong, W.: Unveiling Unprecedented Methane Hotspots in Chinas Leading Coal Production Hub: A Satellite Mapping Revelation, Geophysical Research Letters, 51, e2024GL109065, https://doi.org/10.1029/2024GL109065, 2024.

[26] He, J., Naik, V., and Horowitz, L. W.: Hydroxyl Radical (OH) Response to Meteorological Forcing and Implication for the Methane Budget, Geophysical Research Letters, 48, https://doi.org/10.1029/2021GL094140, 2021.

[27] Heald, C. L., Jacob, D. J., Jones, D. B. A., Palmer, P. I., Logan, J. A., Streets, D. G., Sachse, G. W., Gille, J. C., Hoffman, R. N., and Nehrkorn, T.: Comparative inverse analysis of satellite (MOPITT) and aircraft (TRACE-P) observations to estimate Asian sources of carbon monoxide, Journal of Geophysical Research D: Atmospheres, 109, 117, https://doi.org/10.1029/2004JD005185, 2004.

[28] Hmiel, B., Petrenko, V. V., Dyonisius, M. N., Buizert, C., Smith, A. M., Place, P. F., Harth, C., Beaudette, R., Hua, Q., Yang, B., Vimont, I., Michel, S. E., Severinghaus, J. P., Etheridge, D., Bromley, T., Schmitt, J., Fain, X., Weiss, R. F., and Dlugokencky, E.: Preindustrial 14CH4 indicates greater anthropogenic fossil CH4 emissions, Nature, 578, 409412, https://doi.org/10.1038/s41586-020-1991-8, 2020.

[29] Holmes, C. D., Prather, M. J., Svde, O. A., and Myhre, G.: Future methane, hydroxyl, and their uncertainties: key climate and emission parameters for future predictions, Atmos. Chem. Phys., 13, 285302, https://doi.org/10.5194/acp-13-285-2013, 2013.

[30] Indian Ministry of Coal: Provisional Coal Statistics, 2022-23, 2023.

[31] IPCC: Chapter 4: Fugitive Emissions, in: 2006 IPCC Guidelines for National Greenhouse Gas Inventories: Fugitive Emissions, vol. 2, 4.1-4.78, 2006.

[32] Irving, W. and Tailakov, O.: Good Practice Guidance and Uncertainty Management in National Greenhouse Gas Inventories: CH4 Emissions: Coal Mining and Handling, 2019.

[33] Jacob, D. J., Turner, A. J., Maasakkers, J. D., Sheng, J., Sun, K., Liu, X., Chance, K., Aben, I., McKeever, J., and Frankenberg, C.: Satellite observations of atmospheric methane and their value for quantifying methane emissions, Atmospheric Chemistry and Physics, 16, 1437114396, https://doi.org/10.5194/acp-16-14371-2016, 2016.

[34] Jacob, D. J., Varon, D. J., Cusworth, D. H., Dennison, P. E., Frankenberg, C., Gautam, R., Guanter, L., Kelley, J., McKeever, J., Ott, L. E., Poulter, B., Qu, Z., Thorpe, A. K., Worden, J. R., and Duren, R. M.: Quantifying methane emissions from the global scale down to point sources using satellite observations of atmospheric methane, Atmos. Chem. Phys., 22, 96179646, https://doi.org/10.5194/acp-22-9617-2022, 2022.

[35] Jacob, D. J.: Introduction to Atmospheric Chemistry, Princeton University Press, Princeton, NJ, 1999.

[36] Jervis, D., McKeever, J., Durak, B. O. A., Sloan, J. J., Gains, D., Varon, D. J., Ramier, A., Strupler, M., and Tarrant, E.: The GHGSat-D imaging spectrometer, Atmos. Meas. Tech., 14, 21272140, https://doi.org/10.5194/amt-14-2127-2021, 2021.

[37] Ju, Y., Sun, Y., Sa, Z., Pan, J., Wang, J., Hou, Q., Li, Q., Yan, Z., and Liu, J.: A new approach to estimate fugitive methane emissions from coal mining in China, Science of The Total Environment, 543, 514523, https://doi.org/10.1016/j.scitotenv.2015.11.024, 2016.

[38] Karacan, C. O., Field, R. A., Olczak, M., Kasprzak, M., Ruiz, F. A., and Schwietzke, S.: Mitigating climate change by abating coal mine methane: A critical review of status and opportunities, International Journal of Coal Geology, 295, 104623, https://doi.org/10.1016/j.coal.2024.104623, 2024.

[39] Karacan, C. O., Irakulis-Loitxate, I., Field, R. A., and Warwick, P. D.: Temporal and spatial comparison of coal mine ventilation methane emissions and mitigation quantified using PRISMA satellite data and on-site measurements, Science of The Total Environment, 975, 179268, https://doi.org/10.1016/j.scitotenv.2025.179268, 2025.

[40] Karacan, C. O.: Predicting methane emissions and developing reduction strategies for a Central Appalachian Basin, USA, longwall mine through analysis and modeling of geology and degasification system performance, International Journal of Coal Geology, 270, 104234, https://doi.org/10.1016/j.coal.2023.104234, 2023.

[41] Karmis, M., Agioutantis, Z., and Jarosz, A.: Recent developments in the application of the influence function method for ground movement predictions in the U.S., Mining Science and Technology, 10, 233245, https://doi.org/10.1016/0167-9031(90)90439-Y, 1990.

[42] Keppens, A., Compernolle, S., Verhoelst, T., Hubert, D., and Lambert, J.-C.: Harmonization and comparison of vertically resolved atmospheric state observations: methods, effects, and uncertainty budget, Atmos. Meas. Tech., 12, 43794391, https://doi.org/10.5194/amt-12-4379-2019, 2019.

[43] Kholod, N., Evans, M., Pilcher, R. C., Roshchanka, V., Ruiz, F., Cote, M., and Collings, R.: Global methane emissions from coal mining to continue growing even with declining coal production, Journal of Cleaner Production, 256, 120489, https://doi.org/10.1016/j.jclepro.2020.120489, 2020.

[44] Kirchgessner, D. A., Piccot, S. D., and Masemore, S. S.: An Improved Inventory of Methane Emissions from Coal Mining in the United States, Journal of the Air Waste Management Association, 50, 19041919, https://doi.org/10.1080/10473289.2000.10464227, 2000.

[45] Kissell, F. N., McCulloch, C. M., and Elder, C. H.: The Direct Method of Determining Methane Content of Coalbeds for Ventilation Design, 1973.

[46] Krol, M., van Leeuwen, P. J., and Lelieveld, J.: Global OH trend inferred from methylchloroform measurements, J. Geophys. Res., 103, 1069710711, https://doi.org/10.1029/98JD00459, 1998.

[47] Kulawik, S. S., Worden, J. R., Payne, V. H., Fu, D., Wofsy, S. C., McKain, K., Sweeney, C., Daube Jr., B. C., Lipton, A., Polonsky, I., He, Y., Cady-Pereira, K. E., Dlugokencky, E. J., Jacob, D. J., and Yin, Y.: Evaluation of single-footprint AIRS CH4 profile retrieval uncertainties using aircraft profile measurements, Atmos. Meas. Tech., 14, 335354, https://doi.org/10.5194/amt-14-335-2021, 2021.

[48] Kuze, A., Nakamura, Y., Oda, T., Yoshida, J., Kikuchi, N., Kataoka, F., Suto, H., and Shiomi, K.: Examining partial-column density retrieval of lower-tropospheric CO2 from GOSAT target observations over global megacities, Remote Sensing of Environment, 273, 112966, https://doi.org/10.1016/j.rse.2022.112966, 2022.

[49] Laughner, J. L., Neu, J. L., Schimel, D., Wennberg, P. O., Barsanti, K., Bowman, K. W., Chatterjee, A., Croes, B. E., Fitzmaurice, H. L., Henze, D. K., Kim, J., Kort, E. A., Liu, Z., Miyazaki, K., Turner, A. J., Anenberg, S., Avise, J., Cao, H., Crisp, D., De Gouw, J., Eldering, A., Fyfe, J. C., Goldberg, D. L., Gurney, K. R., Hasheminassab, S., Hopkins, F., Ivey, C. E., Jones, D. B. A., Liu, J., Lovenduski, N. S., Martin, R. V., McKinley, G. A., Ott, L., Poulter, B., Ru, M., Sander, S. P., Swart, N., Yung, Y. L., Zeng, Z.-C., and the rest of the Keck Institute for Space Studies COVID-19: Identifying Unique Opportunities for Earth System Science study team: Societal shifts due to COVID-19 reveal large-scale complexities and feedbacks between atmospheric chemistry and climate change, Proc. Natl. Acad. Sci. U.S.A., 118, e2109481118, https://doi.org/10.1073/pnas.2109481118, 2021.

[50] Lelieveld, J., Gromov, S., Pozzer, A., and Taraborrelli, D.: Global tropospheric hydroxyl distribution, budget and reactivity, Atmospheric Chemistry and Physics, 16, 1247712493, https://doi.org/10.5194/acp-16-12477-2016, 2016.

[51] Levy, H.: Normal Atmosphere: Large Radical and Formaldehyde Concentrations Predicted, Science, 173, 141143, https://doi.org/10.1126/science.173.3992.141, 1971.

[52] Liang, Q., Chipperfield, M. P., Fleming, E. L., Abraham, N. L., Braesicke, P., Burkholder, J. B., Daniel, J. S., Dhomse, S., Fraser, P. J., Hardiman, S. C., Jackman, C. H., Kinnison, D. E., Krummel, P. B., Montzka, S. A., Morgenstern, O., McCulloch, A., Muhle, J., Newman, P. A., Orkin, V. L., Pitari, G., Prinn, R. G., Rigby, M., Rozanov, E., Stenke, A., Tummon, F., Velders, G. J. M., Visioni, D., and Weiss, R. F.: Deriving Global OH Abundance and Atmospheric Lifetimes for Long-Lived Gases: A Search for CH3CCl3 Alternatives, Journal of Geophysical Research: Atmospheres, 122, 11,914-11,933, https://doi.org/10.1002/2017JD026926, 2017.

[53] Liu, H., Crawford, J. H., Pierce, R. B., Norris, P., Platnick, S. E., Chen, G., Logan, J. A., Yantosca, R. M., Evans, M. J., Kittaka, C., Feng, Y., and Tie, X.: Radiative effect of clouds on tropospheric chemistry in a global three-dimensional chemical transport model, J. Geophys. Res., 111, D20303, https://doi.org/10.1029/2005JD006403, 2006.

[54] Lloyd, P.: Fugitive Emissions from Coal Mines: A Report Underpinning the National Inventory, 2008.

[55] Logan, J. A., Prather, M. J., Wofsy, S. C., and McElroy, M. B.: Tropospheric chemistry: A global perspective, J. Geophys. Res., 86, 7210, https://doi.org/10.1029/JC086iC08p07210, 1981.

[56] Lovelock, J. E.: Methyl chloroform in the troposphere as an indicator of OH radical abundance, Nature, 267, 32, 1977.

[57] Lu, X., Jacob, D. J., Zhang, Y., Maasakkers, J. D., Sulprizio, M. P., Shen, L., Qu, Z., Scarpelli, T. R., Nesser, H., Yantosca, R. M., Sheng, J., Andrews, A., Parker, R. J., Boesch, H., Bloom, A. A., and Ma, S.: Global methane budget and trend, 20102017: complementarity of inverse analyses using in situ (GLOBALVIEWplus CH4 ObsPack) and satellite (GOSAT) observations, Atmos. Chem. Phys., 21, 46374657, https://doi.org/10.5194/acp-21-4637-2021, 2021.

[58] Maasakkers, J. D., Jacob, D. J., Sulprizio, M. P., Scarpelli, T. R., Nesser, H., Sheng, J. X., Zhang, Y., Hersher, M., Anthony Bloom, A., Bowman, K. W., Worden, J. R., Janssens-Maenhout, G., and Parker, R. J.: Global distribution of methane emissions, emission trends, and OH concentrations and trends inferred from an inversion of GOSAT satellite data for 2010-2015, Atmospheric Chemistry and Physics, 19, 78597881, https://doi.org/10.5194/acp-19-7859-2019, 2019.

[59] Maasakkers, J. D., Jacob, D. J., Sulprizio, M. P., Turner, A. J., Weitz, M., Wirth, T., Hight, C., DeFigueiredo, M., Desai, M., Schmeltz, R., Hockstad, L., Bloom, A. A., Bowman, K. W., Jeong, S., and Fischer, M. L.: Gridded National Inventory of U.S. Methane Emissions, Environ. Sci. Technol., 50, 1312313133, https://doi.org/10.1021/acs.est.6b02878, 2016.

[60] McArdle, B. H.: The structural relationship: regression in biology, Can. J. Zool., 66, 23292339, https://doi.org/10.1139/z88-348, 1988.

[61] Montzka, S. A., Spivakovsky, C. M., Butler, J. H., Elkins, J. W., Lock, L. T., and Mondeel, D. J.: New Observational Constraints for Atmospheric Hydroxyl on Global and Hemispheric Scales, Science, 288, 500503, https://doi.org/10.1126/science.288.5465.500, 2000.

[62] Murguia-Flores, F., Arndt, S., Ganesan, A. L., Murray-Tortarolo, G., and Hornibrook, E. R. C.: Soil Methanotrophy Model (MeMo v1.0): a process-based model to quantify global uptake of atmospheric methane by soil, Geosci. Model Dev., 11, 20092032, https://doi.org/10.5194/gmd-11-2009-2018, 2018.

[63] Murray, L. T., Fiore, A. M., Shindell, D. T., Naik, V., and Horowitz, L. W.: Large uncertainties in global hydroxyl projections tied to fate of reactive nitrogen and carbon, Proc Natl Acad Sci USA, 118, e2115204118, https://doi.org/10.1073/pnas.2115204118, 2021.

[64] Murray, L. T., Logan, J. A., and Jacob, D. J.: Interannual variability in tropical tropospheric ozone and OH: The role of lightning, J. Geophys. Res. Atmos., 118, 11,468-11,480, https://doi.org/10.1002/jgrd.50857, 2013.

[65] Mutmansky, J. M. and Wang, Y.: Analysis of potential errors in determination of coal mine annual methane emissions, Mineral Resources Engineering, 9, 465474, 2000.

[66] Naik, V., Voulgarakis, A., Fiore, A. M., Horowitz, L. W., Lamarque, J. F., Lin, M., Prather, M. J., Young, P. J., Bergmann, D., Cameron-Smith, P. J., Cionni, I., Collins, W. J., Dalsren, S. B., Doherty, R., Eyring, V., Faluvegi, G., Folberth, G. A., Josse, B., Lee, Y. H., MacKenzie, I. A., Nagashima, T., Van Noije, T. P. C., Plummer, D. A., Righi, M., Rumbold, S. T., Skeie, R., Shindell, D. T., Stevenson, D. S., Strode, S., Sudo, K., Szopa, S., and Zeng, G.: Preindustrial to present-day changes in tropospheric hydroxyl radical and methane lifetime from the Atmospheric Chemistry and Climate Model Intercomparison Project (ACCMIP), Atmospheric Chemistry and Physics, 13, 52775298, https://doi.org/10.5194/acp-13-5277-2013, 2013.

[67] National Oceanic and Atmospheric Administration: NOAA High-Resolution Rapid Refresh (HRRR) Model, n.d. Sadavarte, P., Pandey, S., Maasakkers, J. D., Lorente, A., Borsdorff, T., Denier Van Der Gon, H., Houweling, S., and Aben, I.: Methane Emissions from Superemitting Coal Mines in Australia Quantified Using TROPOMI Satellite Observations, Environ. Sci. Technol., 55, 1657316580, https://doi.org/10.1021/acs.est.1c03976, 2021.

[68] Nicely, J. M., Canty, T. P., Manyin, M., Oman, L. D., Salawitch, R. J., Steenrod, S. D., Strahan, S. E., and Strode, S. A.: Changes in Global Tropospheric OH Expected as a Result of Climate Change Over the Last Several Decades, JGR Atmospheres, 123, https://doi.org/10.1029/2018JD028388, 2018.

[69] Parker, R. and Boesch, H.: University of Leicester GOSAT Proxy XCH4 v9.0. Centre for Environmental Data Analysis, 2020.

[70] Patra, P. K., Krol, M. C., Montzka, S. A., Arnold, T., Atlas, E. L., Lintner, B. R., Stephens, B. B., Xiang, B., Elkins, J. W., Fraser, P. J., Ghosh, A., Hintsa, E. J., Hurst, D. F., Ishijima,

K., Krummel, P. B., Miller, B. R., Miyazaki, K., Moore, F. L., Muhle, J., ODoherty, S., Prinn, R. G., Steele, L. P., Takigawa, M., Wang, H. J., Weiss, R. F., Wofsy, S. C., and Young, D.: Observational evidence for interhemispheric hydroxyl-radical parity, Nature, 513, 219223, https://doi.org/10.1038/nature13721, 2014.

[71] Patra, P. K., Krol, M. C., Prinn, R. G., Takigawa, M., Muhle, J., Montzka, S. A., Lal, S., Yamashita, Y., Naus, S., Chandra, N., Weiss, R. F., Krummel, P. B., Fraser, P. J., ODoherty, S., and Elkins, J. W.: Methyl Chloroform Continues to Constrain the Hydroxyl (OH) Variability in the Troposphere, Journal of Geophysical Research, 2020.

[72] Penn, E. and Nesser, H.: General Observation Operator for Python (GOOPy), 2024. https://github.com/pennelise/GOOPy Pimlott, M. A., Pope, R. J., Kerridge, B. J., Latter, B. G., Knappett, D. S., Heard, D. E., Ventress, L. J., Siddans, R., Feng, W., and Chipperfield, M. P.: Investigating the Global OH Radical Distribution Using Steady-State Approximations and Satellite Data, Gases/Remote Sensing/Troposphere/Chemistry (chemical composition and reactions), https://doi.org/10.5194/acp-2022-79, 2022.

[73] Prather, M. and Spivakovsky, C. M.: Tropospheric OH and the lifetimes of hydrochlorofluorocarbons, J. Geophys. Res., 95, 1872318729, https://doi.org/10.1029/JD095iD11p18723, 1990.

[74] Prather, M. J., Holmes, C. D., and Hsu, J.: Reactive greenhouse gas scenarios: Systematic exploration of uncertainties and the role of atmospheric chemistry, Geophys. Res. Lett., 39, n/a-n/a, https://doi.org/10.1029/2012GL051440, 2012.

[75] Prinn, R. G., Huang, J., Weiss, R. F., Cunnold, D. M., Fraser, P. J., Simmonds, P. G., McCulloch, A., Harth, C., Reimann, S., Salameh, P., ODoherty, S., Wang, R. H. J., Porter, L. W., Miller, B. R., and Krummel, P. B.: Evidence for variability of atmospheric hydroxyl radicals over the past quarter century, Geophysical Research Letters, 32, 2004GL022228, https://doi.org/10.1029/2004GL022228, 2005.

[76] Prinn, R., Cunnold, D., Rasmussen, R., Simmonds, P., Alyea, F., Crawford, A., Fraser, P., and Rosen, R.: Atmospheric Trends in Methylchloroform and the Global Average for the Hydroxyl Radical, Science, 238, 945950, https://doi.org/10.1126/science.238.4829.945, 1987.

[77] Qu, Z., Jacob, D. J., Shen, L., Lu, X., Zhang, Y., Scarpelli, T. R., Nesser, H., Sulprizio, M. P., Maasakkers, J. D., Bloom, A. A., Worden, J. R., Parker, R. J., and Delgado, A. L.: Global distribution of methane emissions: a comparative inverse analysis of observations from the TROPOMI and GOSAT satellite instruments, Atmos. Chem. Phys., 17, 2021.

[78] Qu, Z., Jacob, D. J., Zhang, Y., Shen, L., Varon, D. J., Lu, X., Scarpelli, T., Bloom, A., Worden, J., and Parker, R. J.: Attribution of the 2020 surge in atmospheric methane by inverse analysis of GOSAT observations, Environ. Res. Lett., 17, 094003, https://doi.org/10.1088/1748-9326/ac8754, 2022.

[79] Qu, Z., Jacob, D., Bloom, A., Worden, J., Parker, R., and Boesch, H.: Inverse modeling of satellite observations shows that the wet tropics drive the 2010-2022 methane increase, https://doi.org/10.31223/X5WD6W, 6 January 2024.

[80] Randerson, J. T., van der Werf, G. R., Giglio, L., Collatz, G. J., and Kasibhalta, P. S.: Global Fire Emissions Database, Version 4.1 (GFEDv4), ORNL Distributed Active Archive Center, https://doi.org/10.3334/ORNLDAAC/1293, 2017.

[81] Ribeiro, I. O., Andreoli, R. V., Kayano, M. T., de Sousa, T. R., Medeiros, A. S., Guimaraes, P. C., Barbosa, C. G. G., Godoi, R. H. M., Martin, S. T., and de Souza, R. A. F.: Impact of the biomass burning on methane variability during dry years in the Amazon measured from an aircraft and the AIRS sensor, Science of The Total Environment, 624, 509516, https://doi.org/10.1016/j.scitotenv.2017.12.147, 2018.

[82] Rigby, M., Montzka, S. A., Prinn, R. G., White, J. W. C., Young, D., ODoherty, S., Lunt, M. F., Ganesan, A. L., Manning, A. J., Simmonds, P. G., Salameh, P. K., Harth, C. M., Muhle, J., Weiss, R. F., Fraser, P. J., Steele, L. P., Krummel, P. B., McCulloch, A., and Park, S.: Role of atmospheric oxidation in recent methane growth, Proc Natl Acad Sci USA, 114, 53735377, https://doi.org/10.1073/pnas.1616426114, 2017.

[83] Rodgers, C. D.: Inverse Methods for Atmospheric Sounding, World Scientific Publishing Co. Pte. Ltd., 2000.

[84] Saunois, M., Stavert, A. R., Poulter, B., Bousquet, P., Canadell, J. G., Jackson, R. B., Raymond, P. A., Dlugokencky, E. J., Houweling, S., Patra, P. K., Ciais, P., Arora, V. K., Bastviken, D., Bergamaschi, P., Blake, D. R., Brailsford, G., Bruhwiler, L., Carlson, K. M., Carrol, M., Castaldi, S., Chandra, N., Crevoisier, C., Crill, P. M., Covey, K., Curry, C. L., Etiope, G., Frankenberg, C., Gedney, N., Hegglin, M. I., Hoglund-Isaksson, L., Hugelius, G., Ishizawa, M., Ito, A., Janssens-Maenhout, G., Jensen, K. M., Joos, F., Kleinen, T., Krummel, P. B., Langenfelds, R. L., Laruelle, G. G., Liu, L., Machida, T., Maksyutov, S., McDonald, K. C., McNorton, J., Miller, P. A., Melton, J. R., Morino, I., Muller, J., Murguia-Flores, F., Naik, V., Niwa, Y., Noce, S., ODoherty, S., Parker, R. J., Peng, C., Peng, S., Peters, G. P., Prigent, C., Prinn, R., Ramonet, M., Regnier, P., Riley, W. J., Rosentreter, J. A., Segers, A., Simpson, I. J., Shi, H., Smith, S. J., Steele, L. P., Thornton, B. F., Tian, H., Tohjima, Y., Tubiello, F. N., Tsuruta, A., Viovy, N., Voulgarakis, A., Weber, T. S., Van Weele, M., Van Der Werf, G. R., Weiss, R. F., Worthy, D., Wunch, D., Yin, Y., Yoshida, Y., Zhang, W., Zhang, Z., Zhao, Y., Zheng, B., Zhu, Q., Zhu, Q., and Zhuang, Q.: The Global Methane Budget 20002017, Earth Syst. Sci. Data, 12, 15611623, https://doi.org/10.5194/essd-12-1561-2020, 2020.

[85] Scarpelli, T. R., Jacob, D. J., Grossman, S., Lu, X., Qu, Z., Sulprizio, M. P., Zhang, Y., Reuland, F., Gordon, D., and Worden, J. R.: Updated Global Fuel Exploitation Inventory (GFEI) for methane emissions from the oil, gas, and coal sectors: evaluation with inversions of atmospheric methane observations, Atmos. Chem. Phys., 22, 32353249, https://doi.org/10.5194/acp-22-3235-2022, 2022.

[86] Scarpelli, T. R., Jacob, D. J., Maasakkers, J. D., Sulprizio, M. P., Sheng, J.-X., Rose, K., Romeo, L., Worden, J. R., and Janssens-Maenhout, G.: A global gridded (0.1 0.1) inventory of methane emissions from oil, gas, and coal exploitation based on national reports to the United Nations Framework Convention on Climate Change, 13, 2020.

[87] Schafer, J. and Strimmer, K.: A Shrinkage Approach to Large-Scale Covariance Matrix Estimation and Implications for Functional Genomics, Statistical Applications in Genetics and Molecular Biology, 4, https://doi.org/10.2202/1544-6115.1175, 2005.

[88] Schneider, M., Ertl, B., Tu, Q., Diekmann, C. J., Khosrawi, F., Rohling, A. N., Hase, F., Dubravica, D., Garcia, O. E., Sepulveda, E., Borsdorff, T., Landgraf, J., Lorente, A., Butz, A., Chen, H., Kivi, R., Laemmel, T., Ramonet, M., Crevoisier, C., Pernin, J., Steinbacher, M., Meinhardt, F., Strong, K., Wunch, D., Warneke, T., Roehl, C., Wennberg, P. O., Morino, I., Iraci, L. T., Shiomi, K., Deutscher, N. M., Griffith, D. W. T., Velazco, V. A., and Pollard, D. F.: Synergetic use of IASI profile and TROPOMI total-column level 2 methane retrieval products, Atmos. Meas. Tech., 15, 43394371, https://doi.org/10.5194/amt-15-4339-2022, 2022.

[89] Singh, A. K., Singh, U., Panigrahi, D. C., and Singh, J.: Updated greenhouse gas inventory estimates for Indian underground coal mining based on the 2019 IPCC refinements, iScience, 25, 104946, https://doi.org/10.1016/j.isci.2022.104946, 2022.

[90] Stanevich, I., Jones, D. B. A., Strong, K., Parker, R. J., Boesch, H., Wunch, D., Notholt, J., Petri, C., Warneke, T., Sussmann, R., Schneider, M., Hase, F., Kivi, R., Deutscher, N. M., Velazco, V. A., Walker, K. A., and Deng, F.: Characterizing model errors in chemical transport modeling of methane: Impact of model resolution in versions v9-02 of GEOS-Chem and v35j of its adjoint model, https://doi.org/10.5194/gmd-2019-248, 2020.

[91] Stevenson, D. S., Derwent, R. G., Wild, O., and Collins, W. J.: COVID-19 lockdown emission reductions have the potential to explain over half of the coincident increase in global atmospheric methane, Atmos. Chem. Phys., 22, 1424314252, https://doi.org/10.5194/acp-22-14243-2022, 2022.

[92] Stevenson, D. S., Zhao, A., Naik, V., OConnor, F. M., Tilmes, S., Zeng, G., Murray, L. T., Collins, W. J., Griffiths, P. T., Shim, S., Horowitz, L. W., Sentman, L. T., and Emmons, L.: Trends in global tropospheric hydroxyl radical and methane lifetime since 1850 from AerChemMIP, Atmos. Chem. Phys., 20, 1290512920, https://doi.org/10.5194/acp-20-12905-2020, 2020.

[93] Suto, H.: Joint Submission to the first Global Stocktake: The JAXA/GOSAT GHG product for tracking city-level emission changes, 2022.

[94] Swolkien, J., Fix, A., and Gakowski, M.: Factors influencing the temporal variability of atmospheric methane emissions from Upper Silesia coal mines: a case study from the CoMet mission, Atmos. Chem. Phys., 22, 1603116052, https://doi.org/10.5194/acp-22-16031-2022, 2022.

[95] Swolkien, J., Necki, J., Szlazak, N., Field, R., Korzec, M., Jagoda, P., Bartyzel, J., and Bezyk, Y.: Latest developments in on the ground methane monitoring, 2024.

[96] Szopa, S., Naik, V., Adhikary, P., Artaxo, T., Berntsen, B., Collins, W. D., Fuzzi, S., Gallardo, L., Kiendler-Scharr, A., Klimont, Z., Liao, H., Unger, N., and Zanis, P.: Short-Lived Climate Forcers, 1st ed., Cambridge University Press, https://doi.org/10.1017/9781009157896, 2021.

[97] Tailakov, O. P., Kormin, A. N., Tailakov, V. O., and Gytarsky, M. L.: Methane Emissions from Coal Mining in Russia, Problems of Ecological Monitoring and Modeling of Ecosystems, 22, 216226, 2009.

[98] Turner, A. J., Frankenberg, C., Wennberg, P. O., and Jacob, D. J.: Ambiguity in the causes for decadal trends in atmospheric methane and hydroxyl, Proceedings of the National Academy of Sciences, 114, 53675372, https://doi.org/10.1073/pnas.1616020114, 2017.

[99] Turner, A. J., Jacob, D. J., Benmergui, J., Brandman, J., White, L., and Randles, C. A.: Assessing the capability of different satellite observing configurations to resolve the distribution of methane emissions at kilometer scales, Atmospheric Chemistry and Physics, 18, 82658278, https://doi.org/10.5194/acp-18-8265-2018, 2018.

[100] Turner, A. J., Jacob, D. J., Wecht, K. J., Maasakkers, J. D., Lundgren, E., Andrews, A. E., Biraud, S. C., Boesch, H., Bowman, K. W., Deutscher, N. M., Dubey, M. K., Griffith, D. W. T., Hase, F., Kuze, A., Notholt, J., Ohyama, H., Parker, R., Payne, V. H., Sussmann, R., Sweeney, C., Velazco, V. A., Warneke, T., Wennberg, P. O., and Wunch, D.: Estimating global and North American methane emissions with high spatial resolution using GOSAT satellite data, Atmospheric Chemistry and Physics, 15, 70497069, https://doi.org/10.5194/acp-15-7049-2015, 2015.

[101] U.S. Department of Energy: Methane Recovery from Coalbeds, 1983.

[102] U.S. Energy Information Administration: U.S. Energy Information Administration (EIA) International Coal and Coke Production, 2025.

[103] U.S. Environmental Protection Agency: Coal Mine Methane Developments in the United States, 2018.

[104] U.S. Environmental Protection Agency: Inventory of US Greenhouse Gas Emissions and Sinks: 1990-2022, 2024.

[105] U.S. Mine Safety and Heath Administration: MSHA Operator Employment and Production Data Set - Quarterly, 2024.

[106] United Nations Economic Commission for Europe: Best Practice Guidance for Effective Management of Coal Mine Methane at National Level: Monitoring, Reporting, Verification and Mitigation, United Nations, https://doi.org/10.18356/9789210012454, 2022.

[107] United Nations Economic Commission for Europe: Best Practice Guidance for Effective Methane Drainage and Use in Coal Mines, United Nations, https://doi.org/10.18356/8c636627-en, 2016.

[108] Varon, D. J., Jacob, D. J., Jervis, D., and McKeever, J.: Quantifying Time-Averaged Methane Emissions from Individual Coal Mine Vents with GHGSat-D Satellite Observations, Environ. Sci. Technol., 54, 1024610253, https://doi.org/10.1021/acs.est.0c01213, 2020.

[109] Voulgarakis, A., Wild, O., Savage, N. H., Carver, G. D., and Pyle, J. A.: Clouds, photolysis and regional tropospheric ozone budgets, Atmos. Chem. Phys., 2009.

[110] Wang, X., Jacob, D. J., Eastham, S. D., Sulprizio, M. P., Zhu, L., Chen, Q., Alexander, B., Sherwen, T., Evans, M. J., Lee, B. H., Haskins, J. D., Lopez-Hilfiker, F. D., Thornton, J. A., Huey, G. L., and Liao, H.: The role of chlorine in global tropospheric chemistry, Atmos. Chem. Phys., 19, 39814003, https://doi.org/10.5194/acp-19-3981-2019, 2019.

[111] Wecht, K. J., Jacob, D. J., Frankenberg, C., Jiang, Z., and Blake, D. R.: Mapping of North American methane emissions with high spatial resolution by inversion of SCIAMACHY satellite data, J. Geophys. Res. Atmos., 119, 77417756, https://doi.org/10.1002/2014JD021551, 2014.

[112] Wecht, K. J., Jacob, D. J., Wofsy, S. C., Kort, E. A., Worden, J. R., Kulawik, S. S., Henze, D. K., Kopacz, M., and Payne, V. H.: Validation of TES methane with HIPPO aircraft observations: Implications for inverse modeling of methane sources, Atmospheric Chemistry and Physics, 12, 18231832, https://doi.org/10.5194/acp-12-1823-2012, 2012.

[113] Worden, J. R., Turner, A. J., Bloom, A., Kulawik, S. S., Liu, J., Lee, M., Weidner, R., Bowman, K., Frankenberg, C., Parker, R., and Payne, V. H.: Quantifying lower tropospheric methane concentrations using GOSAT near-IR and TES thermal IR measurements, Atmospheric Measurement Techniques, 8, 34333445, https://doi.org/10.5194/amt-8-3433-2015, 2015.

[114] Xiong, X., Barnet, C. D., Zhuang, Q., MacHida, T., Sweeney, C., and Patra, P. K.: Mid-upper tropospheric methane in the high Northern Hemisphere: Spaceborne observations by AIRS, aircraft measurements, and model simulations, Journal of Geophysical Research Atmospheres, 115, 116, https://doi.org/10.1029/2009JD013796, 2010.

[115] Xiong, X., Barnet, C., Maddy, E., Wofsy, S. C., Chen, L., Karion, A., and Sweeney, C.: Detection of methane depletion associated with stratospheric intrusion by atmospheric infrared sounder (AIRS), Geophys. Res. Lett., 40, 24552459, https://doi.org/10.1002/grl.50476, 2013.

[116] Yin, Y., Chevallier, F., Ciais, P., Bousquet, P., Saunois, M., Zheng, B., Worden, J., Bloom, A. A., Parker, R. J., Jacob, D. J., Dlugokencky, E. J., and Frankenberg, C.: Accelerating methane growth rate from 2010 to 2017: leading contributions from the tropics and East Asia, Atmos. Chem. Phys., 21, 1263112647, https://doi.org/10.5194/acp-21-12631-2021, 2021.

[117] Zhang, B., Tian, H., Ren, W., Tao, B., Lu, C., Yang, J., Banger, K., and Pan, S.: Methane emissions from global rice fields: Magnitude, spatiotemporal patterns, and environmental controls: Methane Emissions From Global Rice Field, Global Biogeochem. Cycles, 30, 12461263, https://doi.org/10.1002/2016GB005381, 2016.

[118] Zhang, X., Bai, W., Zhang, P., and Wang, W.: Spatiotemporal variations in mid-upper tropospheric methane over China from satellite observations, Chin. Sci. Bull., 56, 3321, https://doi.org/10.1007/s11434-011-4666-x, 2011.

[119] Zhang, Y., Jacob, D. J., Lu, X., Maasakkers, J. D., Scarpelli, T. R., Sheng, J.-X., Shen, L., Qu, Z., Sulprizio, M. P., Chang, J., Bloom, A. A., Ma, S., Worden, J., Parker, R. J., and Boesch, H.: Attribution of the accelerating increase in atmospheric methane during 20102018 by inverse analysis of GOSAT observations, https://doi.org/10.5194/acp-2020-964, 2021.

[120] Zhang, Y., Jacob, D. J., Maasakkers, J. D., Sulprizio, M. P., Sheng, J. X., Gautam, R., and Worden, J.: Monitoring global tropospheric OH concentrations using satellite observations of atmospheric methane, Atmospheric Chemistry and Physics, 18, 1595915973, https://doi.org/10.5194/acp-18-15959-2018, 2018.

[121] Zhao, Y., Saunois, M., Bousquet, P., Lin, X., Berchet, A., Hegglin, M. I., Canadell, J. G., Jackson, R. B., Deushi, M., Jockel, P., Kinnison, D., Kirner, O., Strode, S., Tilmes, S., Dlugokencky, E. J., and Zheng, B.: On the role of trend and variability in the hydroxyl radical (OH) in the global methane budget, Atmos. Chem. Phys., 20, 1301113022, https://doi.org/10.5194/acp-20-13011-2020, 2020.

[122] Zhao, Y., Saunois, M., Bousquet, P., Lin, X., Berchet, A., Hegglin, M. I., Canadell, J. G., Jackson, R. B., Hauglustaine, D. A., Szopa, S., Stavert, A. R., Abraham, N. L., Archibald, A. T., Bekki, S., Deushi, M., Jockel, P., Josse, B., Kinnison, D., Kirner, O., Marecal, V., Oamp;apos;Connor, F. M., Plummer, D. A., Revell, L. E., Rozanov, E., Stenke, A., Strode, S., Tilmes, S., Dlugokencky, E. J., and Zheng, B.: Inter-model comparison of global hydroxyl radical (OH) distributions and their impact on atmospheric methane over the 2000-2016 period, Atmospheric Chemistry and Physics, 19, 1370113723, https://doi.org/10.5194/acp-19-13701-2019, 2019.

[123] Zhou, L., Warner, J., Nalli, N. R., Wei, Z., Oh, Y., Bruhwiler, L., Liu, X., Divakarla, M., Pryor, K., Kalluri, S., and Goldberg, M. D.: Spatiotemporal Variability of Global Atmospheric Methane Observed from Two Decades of Satellite Hyperspectral Infrared Sounders, Remote Sensing, 15, 2992, https://doi.org/10.3390/rs15122992, 2023.

Appendix A

Supplementary Material: Chapter 1
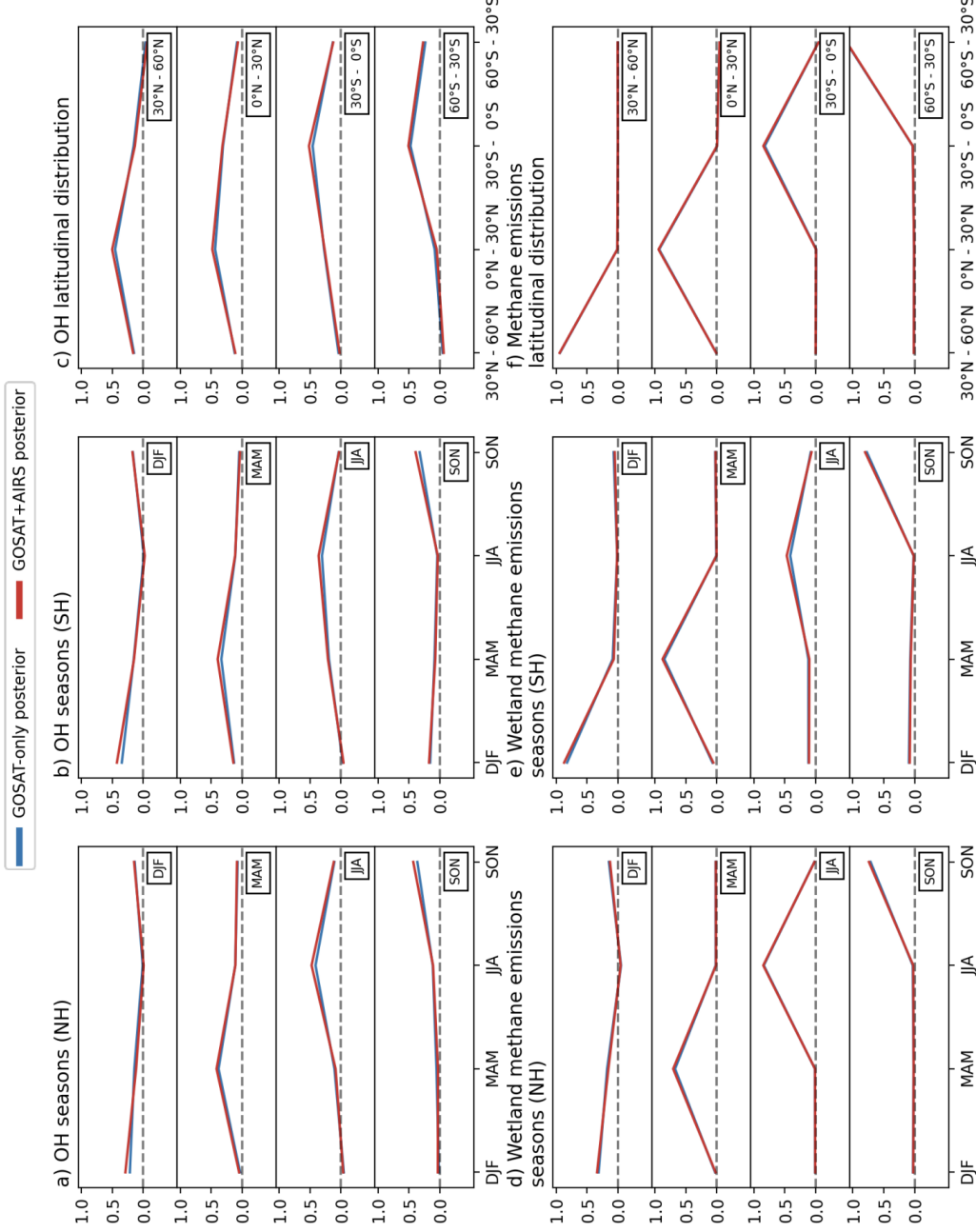
Figure A.1: .
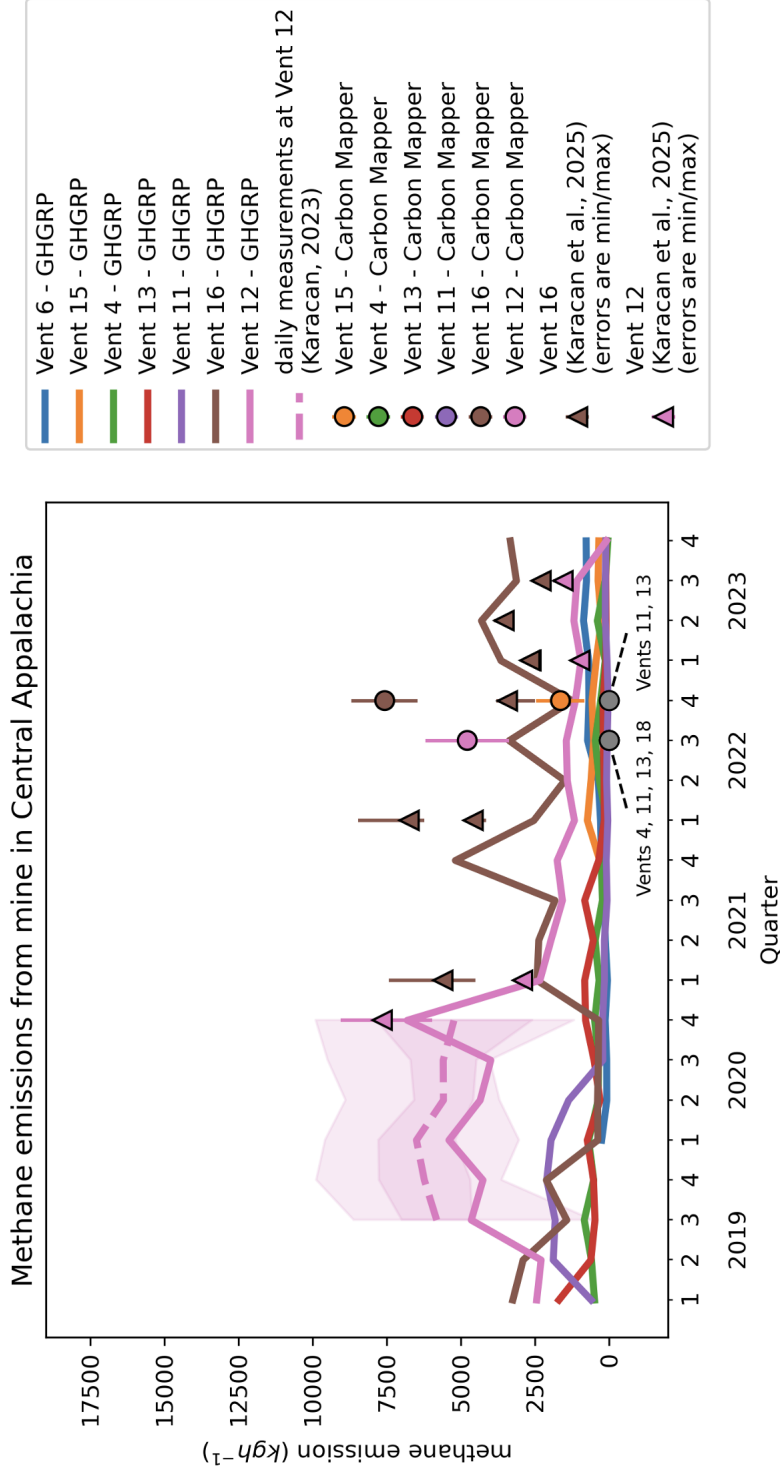
]Ability of inversions using GOSAT and GOSAT+AIRS methane column retrievals to quantify seasonal and latitudinal variabilities of both methane emissions and [OH]. All plots show rows of the reduced averaging kernel matrix, which describe the ability of the observing system to separately quantify [OH] in different latitudinal bands. A perfect observing system would have an averaging kernel sensitivity of 1 for the reduced state vector element of interest (perfect characterization) and 0 for other elements (no error correlation). Because we find posterior emissions and [OH] in terms of relative correction to the prior, all averaging kernel elements are unitless, including off-diagonals.

Appendix B
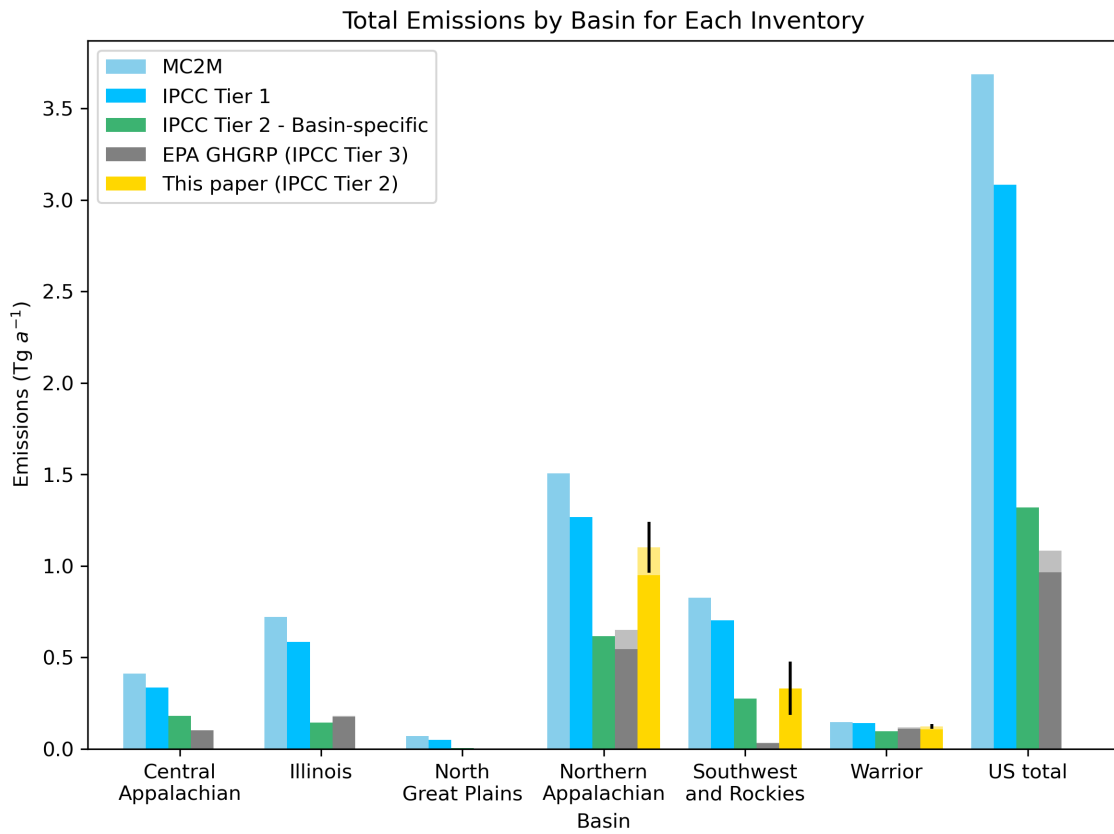
Supplementary Material: Chapter 2

Figure B.1 shows a comparison of daily measurements, Carbon Mapper emission estimates, and quarterly reported EPA GHGRP (https://www.epa.gov/enviro/envirofacts-data-service-api, accessed December 2024) at individual ventilation shaft at one mine in Central Appalachia. Quarterly emissions reported to GHGRP for Vent 16 are within the range of daily measured emissions for each quarter but underestimate average of daily emissions. The standard deviation of daily emissions from this Vent 12 is on average 24% per quarter, consistent with previous estimates for daily mine-level emissions at ventilation shafts (Mutmansky and Wang, 2000; Swolkień et al., 2022; United Nations Economic Commission for Europe, 2022). Although only a few daily measurements are available for Vent 16, a similar pattern emerges; emissions reported to the GHGRP are consistent with the range of emissions but lower than the average of daily emissions.

Carbon Mapper observations of Vents 12 and 16 are both higher than the EPA GHGRP quarterly measurements. Vents 11, 13, 4, and 18 are recorded as 0 emissions, either because the ventilation shafts are not emitting methane or because the emissions fall below the detection limit for this region. The longwall mine in Central Appalachia is not shown in Figure 2 because only 4 of 7 ventilation shafts were successfully quantified in a given quarter. If it were included on this figure, it would appear as an outlier, as the aircraft observations are much higher than GHGRP, beyond the margin of error. However, these higher emissions
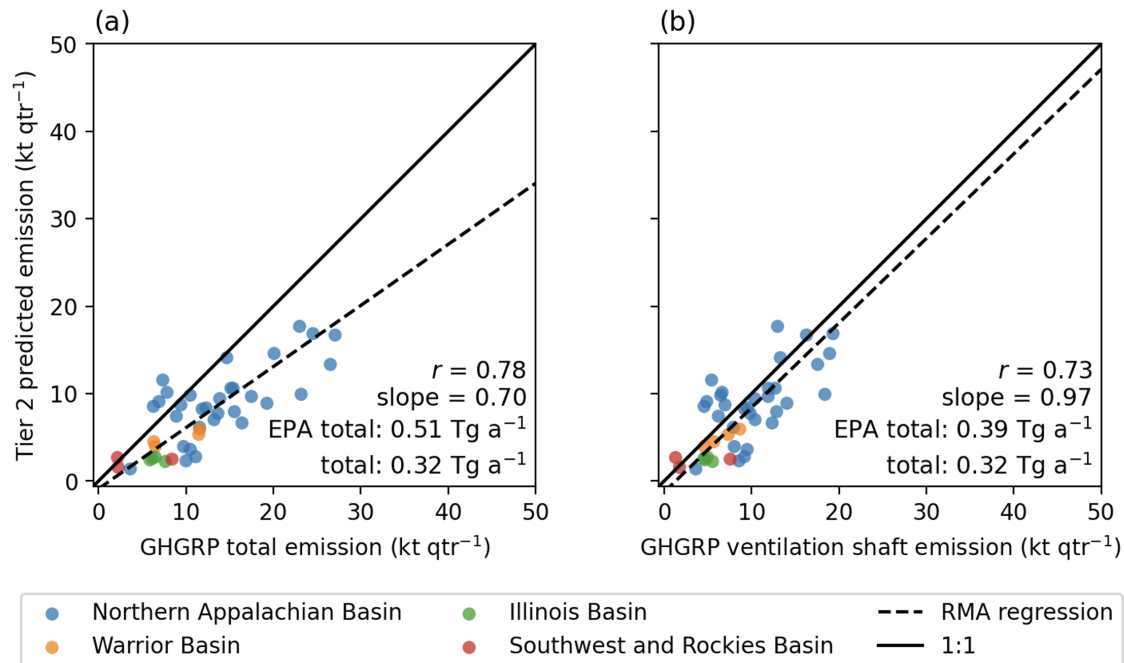
Figure B.1: *Methane emissions from individual ventilation shafts of a longwall coal mine in the Central Appalachian basin using four different quantification techniques: 1) emissions reported to U.S. EPA GHGRP (U.S. Environmental Protection Agency Greenhouse Gas Reporting Program) carried out at least once per quarter, 2) quarterly mean of daily measurements at Vent 12 from Karacan (2023) with standard deviation (dark pink shading) and range (light pink shading), 3) daily average of 1-minute measurements from Karacan et al. (2025) with minimum (min) and maximum (max) 1-minute value indicated by the bars, and 4) Carbon Mapper's emission estimate from the AVIRIS-NG flights with errors indicated by the bars.*

Figure B.2: *Total emissions for each basin predicted by each inventory methodology tested in this paper. The Carbon Mapper inventory is only used in basins where there were sufficient aircraft surveys. For the GHGRP and Carbon Mapper inventories, translucent bars indicate degasification well emissions, while solid bars indicate ventilation shaft emissions or total emissions. Black bars indicate bootstrapped error on the prediction.*

observed by Carbon Mapper are consistent with the distribution of the daily measurements, which suggests a bias could exist in quarterly GHGRP measurements at this mine.

Figure B.3: *Comparison of IPCC Tier 2 basin-specific to GHGRP reported emissions at mines emitting methane from gob wells. Comparison to total mine emissions, including both ventilations shafts and gob wells (a) and mine emissions from ventilation shafts only (b) are shown. RMA (reduced major axis) regressions for GHG-reporting mines are shown as dashed lines. Total emissions and correlation coefficients are inset.*

Table B.1: *Coal basins of the United States.*

Basin	Production (Mt)[1]	Carbon Mapper Surveys	States	Gas content (kg t^{-1})[2]
Northern Appalachian	83.5	05/21, 08/21, 10/22, 11/22	PA, WV (North), MD, OH	2.9
Warrior	9.5	04/22, 09/22	AL, MS	5.7
Central Appalachian	23.9	10/22	KY (East), TN	1.3
		-	WV (South)	2.9
		09/22, 11/22	VA	8.5
Southwest and Rockies	24.0	07/21	UT	2.1
		07/21, 08/21, 10/21	NM	2.2
		08/20, 03/22, 05/22	CO	4.2
Illinois	43.7	-	IL, IN, KY (West)	1.4
North Great Plains	4.8	-	MT, ND, WY	0.34
Northwest	0.0	-	WA	1.0
		-	AK	3.4
West Interior	0.0	-	IA, KS, MO	1.4
		-	AR, LA, TX	2.7

[1] Production is for 2019 at underground mines only (U.S. MSHA, 2024).
[2] Gas content values are based on measurements compiled by the U.S. EPA (2024).

Table B.2: *Locations for ventilation shafts and gob wells.*

Unit ID	Mine Name	Type	Latitude (°)	Longitude (°)
1	MARSHALL COUNTY MINE	Well	39.866371	-80.577396
2	MARSHALL COUNTY MINE	Ventilation Shaft	39.844505	-80.599479
4	IRON EMERALD, LLC	Ventilation Shaft	39.879259	-80.170787
5	MONONGALIA COUNTY MINE	Ventilation Shaft	39.767995	-80.375864
6	IRON CUMBERLAND, LLC	Ventilation Shaft	39.773754	-80.215722
8	ENLOW FORK MINE	Ventilation Shaft	40.095427	-80.297493
9	ENLOW FORK MINE	Ventilation Shaft	40.061145	-80.314815
10	ENLOW FORK MINE	Ventilation Shaft	40.057111	-80.365587
11	ENLOW FORK MINE	Ventilation Shaft	40.035182	-80.326922
12	ENLOW FORK MINE	Ventilation Shaft	39.997644	-80.225111
13	ENLOW FORK MINE	Ventilation Shaft	40.021452	-80.274072
14	MARSHALL COUNTY MINE	Ventilation Shaft	39.813159	-80.517232
15	BAILEY MINE-CRABAPPLE PORTAL	Ventilation Shaft	39.897895	-80.432267
16	BAILEY MINE-CRABAPPLE PORTAL	Ventilation Shaft	39.872069	-80.445644
17	BAILEY MINE-CRABAPPLE PORTAL	Well	39.860630	-80.422418
18	BAILEY MINE-CRABAPPLE PORTAL	Well	39.861577	-80.405690
19	BAILEY MINE-CRABAPPLE PORTAL	Ventilation Shaft	39.859267	-80.400153
20	HARVEY MINE	Well	39.950278	-80.254769

Continued on next page

66

Unit ID	Mine Name	Type	Latitude (°)	Longitude (°)
21	HARVEY MINE	Ventilation Shaft	39.954082	-80.307350
22	HARVEY MINE	Ventilation Shaft	39.943314	-80.320342
23	HARVEY MINE	Ventilation Shaft	39.964069	-80.363207
25	ENLOW FORK MINE	Ventilation Shaft	40.096152	-80.396934
26	HARVEY MINE	Ventilation Shaft	39.954161	-80.248326
27	BAILEY MINE-CRABAPPLE PORTAL	Well	39.856633	-80.408488
28	ENLOW FORK MINE	Ventilation Shaft	40.113908	-80.382086
29	TUNNEL RIDGE, LLC	Ventilation Shaft	40.075378	-80.496263
30	TUNNEL RIDGE, LLC	Ventilation Shaft	40.089321	-80.489205
31	IRON EMERALD, LLC	Ventilation Shaft	39.888574	-80.194406
33	IRON CUMBERLAND, LLC	Well	39.798978	-80.236135
34	IRON CUMBERLAND, LLC	Well	39.795566	-80.245608
35	IRON CUMBERLAND, LLC	Ventilation Shaft	39.792216	-80.245310
36	IRON CUMBERLAND, LLC	Ventilation Shaft	39.836036	-80.273721
37	IRON CUMBERLAND, LLC	Well	39.842053	-80.262605
38	IRON CUMBERLAND, LLC	Ventilation Shaft	39.795825	-80.173632
42	MARION COUNTY MINE	Ventilation Shaft	39.648108	-80.419026
47	MARION COUNTY MINE	Ventilation Shaft	39.631888	-80.360021
48	MARION COUNTY MINE	Ventilation Shaft	39.650818	-80.360446
50	MARSHALL COUNTY MINE	Ventilation Shaft	39.803400	-80.662624

Continued on next page

67

Unit ID	Mine Name	Type	Latitude (°)	Longitude (°)
51	MARSHALL COUNTY MINE	Ventilation Shaft	39.816291	-80.558584
52	MARSHALL COUNTY MINE	Ventilation Shaft	39.833018	-80.553444
53	MARSHALL COUNTY MINE	Ventilation Shaft	39.821036	-80.606546
54	MARSHALL COUNTY MINE	Ventilation Shaft	39.872506	-80.637313
55	BAILEY MINE-CRABAPPLE PORTAL	Well	39.882836	-80.555265
56	BAILEY MINE-CRABAPPLE PORTAL	Ventilation Shaft	39.886076	-80.538844
57	BAILEY MINE-CRABAPPLE PORTAL	Ventilation Shaft	39.912853	-80.524981
58	BAILEY MINE-CRABAPPLE PORTAL	Ventilation Shaft	39.929379	-80.569041
59	UNKNOWN MINE	Ventilation Shaft	39.962691	-80.612623
60	MARSHALL COUNTY MINE	Ventilation Shaft	39.843512	-80.649801
61	HARRISON COUNTY MINE	Ventilation Shaft	39.475493	-80.496131
62	LEER SOUTH MINING COMPLEX	Ventilation Shaft	39.197895	-80.050793
64	BLACK EAGLE DEEP MINE	Ventilation Shaft	37.956638	-81.538951
65	UNKNOWN MINE	Ventilation Shaft	37.737374	-81.723108
66	ICG BECKLEY, LLC	Ventilation Shaft	37.768614	-81.256489
67	HARRISON COUNTY MINE	Ventilation Shaft	39.487681	-80.545664
68	TUNNEL RIDGE, LLC	Ventilation Shaft	40.111814	-80.542291
69	MONONGALIA COUNTY MINE	Ventilation Shaft	39.714135	-80.260894
70	FEDERAL 2 MINE	Ventilation Shaft	39.705071	-80.234735
71	MONONGALIA COUNTY MINE	Ventilation Shaft	39.749678	-80.286107

Continued on next page

68

Unit ID	Mine Name	Type	Latitude (°)	Longitude (°)
72	BAILEY MINE-CRABAPPLE PORTAL	Well	39.859012	-80.416672
73	MARSHALL COUNTY MINE	Well	39.890320	-80.648866
74	BAILEY MINE-CRABAPPLE PORTAL	Ventilation Shaft	39.894785	-80.584081
75	IRON CUMBERLAND, LLC	Well	39.844648	-80.251433
76	IRON CUMBERLAND, LLC	Ventilation Shaft	39.815727	-80.283446
77	IRON CUMBERLAND, LLC	Ventilation Shaft	39.827164	-80.235384
78	ENLOW FORK MINE	Ventilation Shaft	40.005579	-80.284497
80	ENLOW FORK MINE	Well	40.030239	-80.325395
81	ENLOW FORK MINE	Well	40.023446	-80.319955
82	HARVEY MINE	Well	39.973531	-80.325169
87	IRON CUMBERLAND, LLC	Well	39.838655	-80.258728
88	IRON CUMBERLAND, LLC	Well	39.833917	-80.246503
89	IRON CUMBERLAND, LLC	Ventilation Shaft	39.829324	-80.166710
90	MONONGALIA COUNTY MINE	Well	39.746433	-80.359847
92	IRON CUMBERLAND, LLC	Well	39.772788	-80.218423
94	IRON CUMBERLAND, LLC	Well	39.847615	-80.267672
95	IRON CUMBERLAND, LLC	Well	39.839194	-80.271163
96	IRON CUMBERLAND, LLC	Well	39.840962	-80.269723
97	BAILEY MINE-CRABAPPLE PORTAL	Well	39.857709	-80.428003
98	ENLOW FORK MINE	Well	39.999959	-80.227206

Unit ID	Mine Name	Type	Latitude (°)	Longitude (°)
99	HARVEY MINE	Well	39.957112	-80.275746
100	HARVEY MINE	Well	39.953122	-80.263457
101	BAILEY MINE-CRABAPPLE PORTAL	Well	39.848072	-80.415786
102	BAILEY MINE-CRABAPPLE PORTAL	Well	39.851580	-80.408763
105	HARVEY MINE	Well	39.958343	-80.262876
108	ENLOW FORK MINE	Well	40.021099	-80.309687
113	SHOAL CREEK MINE	Ventilation Shaft	33.510509	-87.287191
114	OAK GROVE MINE	Ventilation Shaft	33.486643	-87.094623
115	OAK GROVE MINE	Ventilation Shaft	33.452468	-87.138146
118	OAK GROVE MINE	Ventilation Shaft	33.447673	-87.159241
119	OAK GROVE MINE	Ventilation Shaft	33.440771	-87.140290
120	WARRIOR MET COAL, LLC	Ventilation Shaft	33.403186	-87.199129
121	WARRIOR MET COAL, LLC	Ventilation Shaft	33.421313	-87.239867
122	WARRIOR MET COAL, LLC	Ventilation Shaft	33.377948	-87.232949
123	WARRIOR MET COAL, LLC	Ventilation Shaft	33.370511	-87.218515
124	WARRIOR MET COAL, LLC	Ventilation Shaft	33.376772	-87.251733
125	WARRIOR MET COAL, LLC	Ventilation Shaft	33.394296	-87.265322
126	WARRIOR MET COAL MINE 4	Ventilation Shaft	33.366382	-87.335101
127	WARRIOR MET COAL MINE 4	Ventilation Shaft	33.407931	-87.336669
131	WARRIOR MET COAL MINE 4	Ventilation Shaft	33.329318	-87.330156

70

Unit ID	Mine Name	Type	Latitude (°)	Longitude (°)
132	WARRIOR MET COAL, LLC	Ventilation Shaft	33.322037	-87.241989
133	WARRIOR MET COAL MINE 4	Ventilation Shaft	33.371081	-87.307160
135	WARRIOR MET COAL MINE 4	Ventilation Shaft	33.338877	-87.332319
137	WARRIOR MET COAL MINE 4	Ventilation Shaft	33.381546	-87.375255
140	WARRIOR MET COAL MINE 4	Ventilation Shaft	33.384657	-87.376123
142	WARRIOR MET COAL MINE 4	Ventilation Shaft	33.406386	-87.341514
144	SHOAL CREEK MINE	Ventilation Shaft	33.484071	-87.274153
145	OAK GROVE MINE	Ventilation Shaft	33.481522	-87.141373
146	OAK GROVE MINE	Well	33.480491	-87.100865
147	OAK GROVE MINE	Well	33.485676	-87.099219
148	OAK GROVE MINE	Well	33.492507	-87.096696
149	OAK GROVE MINE	Well	33.475202	-87.131040
151	OAK GROVE MINE	Well	33.434505	-87.104128
152	OAK GROVE MINE	Ventilation Shaft	33.437514	-87.109838
153	OAK GROVE MINE	Well	33.437215	-87.104119
154	OAK GROVE MINE	Well	33.435500	-87.163817
155	OAK GROVE MINE	Well	33.435156	-87.166492
156	OAK GROVE MINE	Well	33.457126	-87.144466
157	OAK GROVE MINE	Well	33.457090	-87.141761
158	OAK GROVE MINE	Well	33.457365	-87.141068

71

Unit ID	Mine Name	Type	Latitude (°)	Longitude (°)
159	OAK GROVE MINE	Ventilation Shaft	33.451223	-87.136441
161	SHOAL CREEK MINE	Ventilation Shaft	33.543877	-87.308449
162	SHOAL CREEK MINE	Ventilation Shaft	33.535882	-87.333631
163	DEER RUN MINE	Ventilation Shaft	39.137856	-89.474890
164	DEER RUN MINE	Ventilation Shaft	39.136240	-89.414764
165	DEER RUN MINE	Ventilation Shaft	39.127395	-89.465667
166	DEER RUN MINE	Ventilation Shaft	39.119356	-89.408750
167	GALATIA MINE	Ventilation Shaft	37.832335	-88.671022
168	GALATIA MINE	Ventilation Shaft	37.847175	-88.664043
169	GALATIA MINE	Ventilation Shaft	37.882108	-88.670653
170	GALATIA MINE	Ventilation Shaft	37.843628	-88.706232
171	POND CREEK NO. 1 MINE	Ventilation Shaft	37.814429	-88.800169
172	POND CREEK NO. 1 MINE	Ventilation Shaft	37.847713	-88.832131
173	POND CREEK NO. 1 MINE	Ventilation Shaft	37.847715	-88.832961
174	SUGAR CAMP ENERGY, LLC	Ventilation Shaft	38.059842	-88.762125
175	SHAY 1 MINE	Ventilation Shaft	39.205917	-89.862177
176	SHAY 1 MINE	Ventilation Shaft	39.217267	-89.859970
180	PRAIRIE STATE GENERATING STATION	Ventilation Shaft	38.285558	-89.652563
181	PRAIRIE STATE GENERATING STATION	Ventilation Shaft	38.285551	-89.655322
182	WHITE OAK RESOURCES MINE NO. 1/HAMILTON COUNTY COAL	Ventilation Shaft	38.171068	-88.601610

Continued on next page

72

Unit ID	Mine Name	Type	Latitude (°)	Longitude (°)
183	GATEWAY NORTH MINE	Ventilation Shaft	38.191678	-89.619395
184	GATEWAY NORTH MINE	Ventilation Shaft	38.190936	-89.616595
185	PRAIRIE STATE GENERATING STATION	Ventilation Shaft	38.351152	-89.647030
186	PRAIRIE STATE GENERATING STATION	Ventilation Shaft	38.352468	-89.647043
187	VIPER MINE	Ventilation Shaft	39.952967	-89.500484
188	VIPER MINE	Ventilation Shaft	39.951695	-89.499428
189	BUCHANAN MINE 1	Ventilation Shaft	37.250378	-81.898450
190	BUCHANAN MINE 1	Ventilation Shaft	37.233797	-81.850962
191	BUCHANAN MINE 1	Ventilation Shaft	37.175346	-81.927226
192	BUCHANAN MINE 1	Ventilation Shaft	37.174391	-81.879132
193	BUCHANAN MINE 1	Ventilation Shaft	37.223978	-81.887419
195	BUCHANAN MINE 1	Ventilation Shaft	37.172423	-81.955442
196	BUCHANAN MINE 1	Ventilation Shaft	37.209930	-81.854707
198	BUCHANAN MINE 1	Ventilation Shaft	37.144688	-81.926050
200	MCCOY ELKHORN COAL	Ventilation Shaft	37.551287	-82.410673
204	WEST ELK MINE	Ventilation Shaft	38.880612	-107.462605
205	DUGOUT CANYON MINE	Ventilation Shaft	39.682741	-110.545329
207	SAN JUAN MINE	Ventilation Shaft	36.792764	-108.389156
210	HOPEDALE MINE	Ventilation Shaft	40.294107	-80.972540
211	IRON EMERALD, LLC	Well	39.878251	-80.170647

73

Unit ID	Mine Name	Type	Latitude (°)	Longitude (°)
214	WEST ELK MINE	Ventilation Shaft	38.899951	-107.440703

Table B.3: *Carbon Mapper plumes.*

Unit ID	Scene ID[1]	Plume[2]	Latitude[3] (°)	Longitude[4] (°)	Emission (kg h^{-1})[5]	Uncertainty (kg h^{-1})[5]	Quality[6]
1	ang20221009t162340				0.0	50.0	
1	ang20221003t181100				0.0	50.0	
1	ang20221003t160932				0.0	50.0	
1	GAO20210813t152451p0000	A	39.866352	-80.577424	1605.0	298.0	hide
2	ang20221103t164406				0.0	50.0	
2	ang20221009t162340				0.0	50.0	
2	ang20221003t181100				0.0	50.0	
2	GAO20210813t152451p0000	B	39.844464	-80.599233	1191.0	42.0	pass
4	ang20221024t174902				0.0	50.0	
4	ang20221009t181144				0.0	50.0	
4	GAO20210521t155242p0000	A	39.879266	-80.170721	377.0	103.0	pass
4	GAO20210515t144158p0000				0.0	50.0	
4	GAO20210514t132657p0000				0.0	50.0	
5	GAO20210813t141544p0000	A	39.76801	-80.375778	4308.0	1967.0	pass
5	GAO20210813t140412p0000	A	39.768	-80.3758	5052.0	1765.0	pass
5	GAO20210531t123731p0000	A	39.76806	-80.37585	2185.0	1670.0	pass
5	GAO20210521t135234p0000	3	39.768146	-80.375678	4774.0	1585.0	hide
5	GAO20210521t131640p0001	3	39.768006	-80.37576	6016.0	1945.0	pass

Continued on next page

Unit ID	Scene ID[1]	Plume[2]	Latitude[3] (°)	Longitude[4] (°)	Emission (kg h^{-1})[5]	Uncertainty (kg h^{-1})[5]	Quality[6]
6	ang202210242174902	A	39.773642	-80.215336	892.0	322.0	pass
6	ang202210092181144	C	39.773482	-80.215688	1168.0	349.0	pass
6	GAO20210813t141544p0000	B	39.773911	-80.215555	2426.0	898.0	pass
6	GAO20210813t140412p0000	B	39.77384	-80.215674	2724.0	433.0	pass
6	GAO20210521t151830p0000	2	39.773927	-80.215563	3496.0	636.0	pass
8	ang202211032161828				0.0	50.0	
8	GAO20210521t144353p0000	1	40.095516	-80.29758	839.0	261.0	pass
8	GAO20210521t142744p0000	1	40.095425	-80.297464	1495.0	522.0	hide
8	GAO20210515t140819p0000	1	40.095483	-80.297741	530.0	192.0	pass
8	GAO20210515t135940p0000	1	40.095568	-80.297824	532.0	361.0	pass
8	GAO20210513t152129p0000	2	40.095326	-80.297701	583.0	369.0	pass
8	GAO20210513t150800p0000	2	40.095272	-80.298046	1585.0	522.0	pass
9	ang202211032161828				0.0	50.0	
9	GAO20210521t142744p0000	A	40.061139	-80.314804	926.0	407.0	pass
9	GAO20210515t135940p0000	A	40.061393	-80.314837	187.0	63.0	pass
9	GAO20210513t150800p0000	3	40.061149	-80.314838	366.0	210.0	pass
10	ang202211032163129						
10	ang202210032175331						
10	GAO20210521t135234p0000				0.0	50.0	
10	GAO20210515t134113p0000				0.0	50.0	

Continued on next page

76

Unit ID	Scene ID[1]	Plume[2]	Latitude[3] (°)	Longitude[4] (°)	Emission (kg h^{-1})[5]	Uncertainty (kg h^{-1})[5]	Quality[6]
10	GAO20210513t143909p0000				0.0	50.0	
11	ang20221103t161828	A	40.034858	-80.326904	372.0	99.0	pass
11	ang20221103t161828	F	40.03501	-80.326954	374.0	114.0	pass
11	GAO20210521t142744p0000	2	40.03476	-80.327014	4144.0	2583.0	hide
11	GAO20210521t140904p0000	1	40.035	-80.327	6328.0	3009.0	pass
11	GAO20210515t135940p0000	2	40.034914	-80.327003	1116.0	529.0	hide
11	GAO20210515t135117p0000	1	40.035	-80.3271	2197.0	231.0	pass
11	GAO20210513t150800p0000	B	40.034994	-80.326819	1864.0	620.0	hide
11	GAO20210513t145258p0000	3	40.034756	-80.32719	2193.0	883.0	pass
12	ang20221024t182326	A	39.997661	-80.225097	3052.0	506.0	pass
12	ang20221009t184703	B	39.997528	-80.225972	4283.0	2304.0	pass
12	GAO20210521t151830p0000				0.0	50.0	
12	GAO20210515t142544p0000				0.0	50.0	
12	GAO20210514t125900p0000				0.0	50.0	
12	GAO20210513t155053p0000				0.0	50.0	
13	GAO20210521t144353p0000	2	40.021445	-80.274164	2148.0	323.0	pass
13	GAO20210515t140819p0000	2	40.021655	-80.273769	1364.0	306.0	pass
13	GAO20210513t152129p0000	3	40.021496	-80.273984	1233.0	906.0	pass
14	ang20221003t174156	A	39.813266	-80.517153	1924.0	905.0	pass
14	GAO20210813t143551p0000				0.0	50.0	

Unit ID	Scene ID[1]	Plume[2]	Latitude[3] (°)	Longitude[4] (°)	Emission (kg h^{-1})[5]	Uncertainty (kg h^{-1})[5]	Quality[6]
14	GAO20210813t142433p0000				0.0	50.0	
15	ang20221103t163129	B	39.898109	-80.432545	317.0	96.0	pass
15	ang20221003t175331	B	39.898095	-80.432551	558.0	209.0	pass
15	GAO20210813t144619p0000	A	39.898086	-80.432485	1633.0	390.0	pass
15	GAO20210521t131640p0000				0.0	50.0	
15	GAO20210515t132309p0000	B	39.897926	-80.432363	648.0	156.0	pass
15	GAO20210513t141020p0000	A	39.898078	-80.432529	274.0	60.0	pass
16	ang20221103t163129	A	39.872178	-80.44563	374.0	78.0	pass
16	ang20221103t153837	F	39.872109	-80.445754	358.0	91.0	pass
16	ang20221003t175331	C	39.872157	-80.445674	1856.0	894.0	pass
16	ang20221003t160932	D	39.872244	-80.445557	1439.0	487.0	pass
16	GAO20210813t144305p0000	B	39.872156	-80.445678	1455.0	370.0	pass
17	ang20221103t163129	D	39.860645	-80.42262	405.0	244.0	pass
17	ang20221103t153837	G	39.860644	-80.422522	218.0	103.0	pass
17	ang20221003t160932	H	39.860665	-80.422488	656.0	261.0	pass
17	GAO20210813t144305p0000	A	39.860511	-80.422565	648.0	468.0	hide
17	GAO20210813t143918p0000	D	39.860619	-80.422612	1186.0	525.0	pass
17	GAO20210521t131640p0000						
17	GAO20210515t132309p0000	2	39.860717	-80.422931	1048.0	331.0	hide
17	GAO20210513t141020p0000	3	39.8606	-80.4225	684.0	330.0	pass

Unit ID	Scene ID[1]	Plume[2]	Latitude[3] (°)	Longitude[4] (°)	Emission (kg h⁻¹)[5]	Uncertainty (kg h⁻¹)[5]	Quality[6]
18	ang20221103t161828	H	39.861627	-80.405707	843.0	360.0	hide
18	ang20221103t153837	N	39.861586	-80.405693	128.0	18.0	pass
18	ang20221003t160932	I	39.861613	-80.405673	755.0	152.0	pass
18	GAO20210813t144305p0000				0.0	50.0	
18	GAO20210813t143918p0000				0.0	50.0	
18	GAO20210521t131640p0001						
18	GAO20210521t131640p0000						
18	GAO20210515t132309p0000						
18	GAO20210513t141020p0000						
19	ang20221103t161828	B	39.859321	-80.400108	1365.0	665.0	pass
19	ang20221103t153837	H	39.859294	-80.400079	739.0	134.0	pass
19	ang20221103t153837	M	39.85918	-80.399982	705.0	69.0	pass
19	ang20221003t160932	F	39.859337	-80.399861	2898.0	406.0	pass
19	GAO20210813t143918p0000	A	39.859284	-80.400166	1896.0	702.0	pass
19	GAO20210521t131640p0000						
19	GAO20210521t131640p0001	2	39.859361	-80.400128	1440.0	623.0	pass
19	GAO20210515t133138p0000	4	39.85931	-80.400195	894.0	656.0	pass
19	GAO20210515t132309p0000	A	39.859273	-80.400393	637.0	193.0	hide
19	GAO20210513t142329p0000	3	39.8592	-80.4	2380.0	452.0	pass
19	GAO20210513t141020p0000	6	39.8592	-80.4002	1837.0	378.0	pass

Unit ID	Scene ID[1]	Plume[2]	Latitude[3] (°)	Longitude[4] (°)	Emission (kg h^{-1})[5]	Uncertainty (kg h^{-1})[5]	Quality[6]
20	ang20221103t155207	J	39.950496	-80.25505	486.0	92.0	pass
20	ang20221024t183453	H	39.950275	-80.254765	601.0	198.0	pass
20	ang20221024t182326	G	39.950276	-80.254739	488.0	45.0	pass
20	ang20221009t185838	C	39.950344	-80.254855	1433.0	149.0	pass
20	ang20221009t184703	I	39.950277	-80.254785	916.0	297.0	pass
20	GAO20210521t150211p0000				0.0	50.0	
20	GAO20210515t141643p0000				0.0	50.0	
20	GAO20210513t153658p0000				0.0	50.0	
21	GAO20210521t142744p0000	5	39.953811	-80.307148	648.0	358.0	pass
21	GAO20210515t135940p0000	5	39.953741	-80.307265	517.0	141.0	pass
21	GAO20210513t150800p0000	6	39.953897	-80.307549	823.0	410.0	pass
22	ang20221103t160514				0.0	50.0	
22	GAO20210521t142744p0000						
22	GAO20210521t140904p0000				0.0	50.0	
22	GAO20210515t135940p0000				0.0	50.0	
22	GAO20210515t135117p0000				0.0	50.0	
22	GAO20210513t150800p0000				0.0	50.0	
22	GAO20210513t145258p0000				0.0	50.0	
23	ang20221103t161828				0.0	50.0	
23	GAO20210521t135234p0000	2	39.964039	-80.363209	3842.0	1689.0	pass

Unit ID	Scene ID[1]	Plume[2]	Latitude[3] (°)	Longitude[4] (°)	Emission (kg h^{-1})[5]	Uncertainty (kg h^{-1})[5]	Quality[6]
23	GAO20210515t134113p0000	2	39.9643	-80.3631	1221.0	249.0	pass
23	GAO20210513t143909p0000	3	39.964346	-80.36317	3724.0	1583.0	pass
25	ang20221003t174156				0.0	50.0	
25	GAO20210521t131640p0001	1	40.096436	-80.396995	602.0	170.0	pass
25	GAO20210515t133138p0000	1	40.0963	-80.3971	240.0	36.0	pass
25	GAO20210513t142329p0000	2	40.0963	-80.3971	548.0	249.0	pass
26	ang20221103t155207				0.0	50.0	
26	ang20221024t183453	C	39.954189	-80.248373	2864.0	1095.0	hide
26	ang20221024t182326	B	39.954191	-80.248382	3363.0	455.0	pass
26	ang20221009t184703	A	39.954348	-80.248214	3523.0	1280.0	pass
26	GAO20210521t150211p0000	1	39.954233	-80.248388	1441.0	421.0	pass
26	GAO20210515t141643p0000	1	39.9543	-80.2482	1144.0	494.0	pass
26	GAO20210513t153658p0000	4	39.954369	-80.248318	1471.0	1386.0	pass
27	ang20221103t161828				0.0	50.0	
27	ang20221103t153837	L	39.856821	-80.408544	93.0	37.0	pass
27	ang20221003t160932				0.0	50.0	
27	GAO20210813t143918p0000	B	39.856645	-80.408475	778.0	193.0	pass
27	GAO20210521t131640p0000						
27	GAO20210515t132309p0000						
27	GAO20210513t141020p0000	5	39.8566	-80.4086	365.0	74.0	pass

Unit ID	Scene ID[1]	Plume[2]	Latitude[3] (°)	Longitude[4] (°)	Emission (kg h⁻¹)[5]	Uncertainty (kg h⁻¹)[5]	Quality[6]
28	ang20221003t174156				0.0	50.0	
28	GAO20210521t135234p0000	1	40.113929	-80.382583	605.0	246.0	pass
28	GAO20210521t131640p0001	A	40.114022	-80.382436	590.0	340.0	pass
28	GAO20210515t134113p0000	1	40.114215	-80.38264	192.0	88.0	pass
28	GAO20210515t133138p0000	2	40.114201	-80.382473	369.0	80.0	pass
28	GAO20210513t143909p0000	1	40.113869	-80.382433	614.0	194.0	pass
28	GAO20210513t142329p0000	1	40.113784	-80.382594	298.0	129.0	pass
29	ang20221103t164406	A	40.075452	-80.496208	192.0	121.0	hide
29	ang20221009t162340	A	40.075429	-80.496219	2086.0	407.0	pass
29	ang20221003t181100	B	40.075688	-80.496049	2494.0	574.0	pass
30	ang20221103t164406	B	40.089417	-80.489064	159.0	96.0	pass
30	ang20221009t162340	B	40.089367	-80.489318	905.0	181.0	pass
30	ang20221003t181100	A	40.089586	-80.489074	864.0	370.0	pass
31	ang20221024t180037				0.0	50.0	
31	ang20221009t182331				0.0	50.0	
31	GAO20210521t153629p0000				0.0	50.0	
31	GAO20210515t143339p0000						
31	GAO20210514t131258p0000				0.0	50.0	
31	GAO20210513t160410p0000						
33	ang20221024t180037	B	39.798945	-80.236252	504.0	106.0	pass

Unit ID	Scene ID[1]	Plume[2]	Latitude[3] (°)	Longitude[4] (°)	Emission (kg h⁻¹)[5]	Uncertainty (kg h⁻¹)[5]	Quality[6]
33	ang202210009t182331				0.0	50.0	
33	GAO20210813t142433p0000				0.0	50.0	
33	GAO20210813t141544p0000				0.0	50.0	
33	GAO20210521t150211p0000				0.0	50.0	
33	GAO20210515t141643p0000				0.0	50.0	
33	GAO20210513t153658p0000				0.0	50.0	
34	ang202210024t180037	D	39.795565	-80.245884	466.0	104.0	pass
34	ang202210009t182331	B	39.795092	-80.246	2042.0	242.0	pass
34	GAO20210813t142433p0000				0.0	50.0	
34	GAO20210813t141544p0000				0.0	50.0	
34	GAO20210521t150211p0000				0.0	50.0	
34	GAO20210515t141643p0000				0.0	50.0	
34	GAO20210513t153658p0000				0.0	50.0	
35	ang202210024t180037				0.0	50.0	
35	ang202210009t182331				0.0	50.0	
35	GAO20210813t141544p0000	C	39.792175	-80.245351	1037.0	177.0	pass
35	GAO20210521t150211p0000	A	39.792197	-80.245119	353.0	124.0	pass
35	GAO20210515t141643p0000	5	39.7923	-80.2451	509.0	127.0	pass
35	GAO20210513t153658p0000	8	39.79211	-80.244756	513.0	262.0	hide
36	ang202210024t182326	C	39.836043	-80.273769	5316.0	753.0	hide

Unit ID	Scene ID[1]	Plume[2]	Latitude[3] (°)	Longitude[4] (°)	Emission (kg h^{-1})[5]	Uncertainty (kg h^{-1})[5]	Quality[6]
36	ang20221024t181205	D	39.836035	-80.273759	5395.0	566.0	hide
36	ang20221009t184703	G	39.836162	-80.273603	5817.0	959.0	hide
36	ang20221009t183505	A	39.836204	-80.273628	5543.0	363.0	pass
36	GAO20210521t144353p0000	4	39.836024	-80.273818	3310.0	411.0	pass
36	GAO20210515t140819p0000	3	39.836069	-80.273759	688.0	192.0	pass
36	GAO20210513t152129p0000	6	39.836216	-80.273399	3331.0	582.0	pass
37	ang20221024t181205	C	39.842057	-80.262473	320.0	106.0	pass
37	ang20221009t183505						
37	GAO20210521t150211p0000				0.0	50.0	
37	GAO20210521t144353p0000				0.0	50.0	
37	GAO20210515t140819p0000				0.0	50.0	
37	GAO20210513t153658p0000				0.0	50.0	
37	GAO20210513t152129p0000				0.0	50.0	
38	ang20221024t173730	A	39.795838	-80.173356	353.0	236.0	pass
38	ang20221009t180013	B	39.79591	-80.173447	207.0	20.0	hide
38	GAO20210813t142433p0000						
38	GAO20210813t141544p0000	D	39.795822	-80.173581	984.0	127.0	pass
38	GAO20210521t155242p0000	1	39.795892	-80.173849	1535.0	468.0	hide
38	GAO20210521t153629p0000	2	39.795831	-80.173809	2304.0	854.0	hide
38	GAO20210513t160410p0000	A	39.79567	-80.173583	491.0	109.0	hide

Unit ID	Scene ID[1]	Plume[2]	Latitude[3] (°)	Longitude[4] (°)	Emission (kg h⁻¹)[5]	Uncertainty (kg h⁻¹)[5]	Quality[6]
42	ang20221103t155207	A	39.647991	-80.4188	2247.0	548.0	pass
42	ang20221024t183453	E	39.648008	-80.419098	2918.0	1158.0	hide
42	ang20221009t185838	A	39.647851	-80.419241	8320.0	714.0	pass
42	GAO20210521t131640p0000	2	39.648	-80.4191	2031.0	296.0	pass
47	ang20221024t181205	E	39.631976	-80.360043	650.0	195.0	pass
47	ang20221009t184703				0.0	50.0	
47	ang20221009t183505				0.0	50.0	
47	GAO20210521t131640p0000						
48	ang20221024t182326	D	39.651137	-80.360875	404.0	105.0	pass
48	ang20221009t184703	F	39.651034	-80.360717	997.0	452.0	pass
48	ang20221009t183505						
48	GAO20210521t135234p0000				0.0	50.0	
50	ang20221103t165729	D	39.80338	-80.662703	296.0	70.0	pass
51	ang20221003t172744	B	39.816174	-80.558875	2079.0	231.0	pass
52	ang20221003t172744	A	39.832944	-80.553294	7749.0	1129.0	pass
52	ang20221003t171601	E	39.833134	-80.553317	1584.0	1469.0	hide
53	ang20221103t164406				0.0	50.0	
53	ang20221009t162340	C	39.821169	-80.606542	1415.0	255.0	pass
53	ang20221003t181100	E	39.821103	-80.606307	1434.0	725.0	pass
54	ang20221103t165729	A	39.87261	-80.637089	986.0	423.0	pass

Unit ID	Scene ID[1]	Plume[2]	Latitude[3] (°)	Longitude[4] (°)	Emission (kg h⁻¹)[5]	Uncertainty (kg h⁻¹)[5]	Quality[6]
54	GAO20210813t153316p0000	C	39.872527	-80.637224	2457.0	935.0	pass
55	ang20221103t153837	D	39.88263	-80.555138	274.0	128.0	hide
55	ang20221009t162340				0.0	50.0	
55	ang20221003t181100	C	39.882747	-80.555257	1066.0	138.0	pass
55	ang20221003t171601	C	39.882841	-80.555155	751.0	394.0	pass
55	ang20221003t160932	C	39.882812	-80.555122	930.0	239.0	pass
55	GAO20210813t152451p0000				0.0	50.0	
56	ang20221103t153837	E	39.885965	-80.539047	709.0	261.0	pass
56	ang20221003t171601	B	39.885979	-80.538833	2120.0	679.0	pass
56	ang20221003t160932	B	39.885755	-80.538624	2694.0	795.0	pass
56	GAO20210813t152451p0000	D	39.886006	-80.538818	3799.0	1104.0	pass
57	ang20221003t171601	A	39.912904	-80.524949	2507.0	1309.0	pass
57	GAO20210813t153316p0000	A	39.912902	-80.524961	1700.0	519.0	pass
58	ang20221103t164406						
58	GAO20210813t154231p0000	B	39.929294	-80.56911	1523.0	625.0	pass
59	ang20221103t171109	C	39.962889	-80.612792	107.0	34.0	pass
59	ang20221103t165729						
60	ang20221103t165729	B	39.843599	-80.649619	320.0	165.0	pass
60	GAO20210813t152451p0000				0.0	50.0	
61	ang20221103t175310				0.0	50.0	

Unit ID	Scene ID[1]	Plume[2]	Latitude[3] (°)	Longitude[4] (°)	Emission (kg h⁻¹)[5]	Uncertainty (kg h⁻¹)[5]	Quality[6]
61	ang202210161165920				0.0	50.0	
62	ang20221103t183217	A	39.197904	-80.050788	788.0	328.0	pass
62	ang20221103t183217	C	39.19783	-80.050743	812.0	330.0	pass
67	ang20221103t175310	A	39.487605	-80.545579	2064.0	588.0	pass
67	ang202210161165920				0.0	50.0	
68	ang20221103t71109	B	40.112195	-80.542403	52.0	21.0	hide
68	ang20221103t165729				0.0	50.0	
69	ang20221024t174902	B	39.714377	-80.260785	457.0	232.0	pass
69	ang20221009t181144	B	39.714003	-80.260994	1403.0	131.0	pass
69	GAO20210813t150611p0000				0.0	50.0	
69	GAO20210813t135114p0000				0.0	50.0	
69	GAO20210521t144353p0000				0.0	50.0	
70	ang20221024t174902						
70	ang20221024t173730				0.0	50.0	
70	ang20221009t180013	A	39.7051	-80.2347	1873.0	1000.0	pass
70	GAO20210813t150611p0000	A	39.704993	-80.234638	2182.0	1540.0	hide
70	GAO20210813t145923p0000	A	39.704994	-80.234635	3094.0	945.0	pass
70	GAO20210813t135114p0000	A	39.704993	-80.234712	3302.0	610.0	pass
70	GAO20210813t134456p0000	A	39.704987	-80.234616	3206.0	602.0	pass
70	GAO20210521t150211p0000				0.0	50.0	

Unit ID	Scene ID[1]	Plume[2]	Latitude[3] (°)	Longitude[4] (°)	Emission (kg h^{-1})[5]	Uncertainty (kg h^{-1})[5]	Quality[6]
71	ang20221024t181205					50.0	
71	ang20221024t180037					50.0	
71	ang20221009t183505					50.0	
71	GAO20210813t151207p0000	A	39.749381	-80.286343	597.0	52.0	hide
71	GAO20210813t140412p0000					50.0	
71	GAO20210521t144353p0000					50.0	
71	GAO20210521t142744p0000	B	39.749355	-80.28619	318.0	78.0	pass
72	ang20221103t163129					50.0	
72	ang20221103t161828					50.0	
72	ang20221103t153837					50.0	
72	ang20221003t160932					50.0	
72	GAO20210813t143918p0000	C	39.85899	-80.416669	1648.0	217.0	pass
72	GAO20210521t131640p0000	1	39.85892	-80.41669	2247.0	1007.0	pass
72	GAO20210515t132309p0000					50.0	
72	GAO20210513t141020p0000	4	39.859	-80.4167	1266.0	275.0	pass
73	ang20221103t171109					50.0	
73	ang20221103t153837					50.0	
73	ang20221003t160932					50.0	
73	GAO20210813t154231p0000	A	39.890373	-80.648835	1029.0	356.0	pass
74	ang20221103t164406					50.0	

Continued on next page

Unit ID	Scene ID[1]	Plume[2]	Latitude[3] (°)	Longitude[4] (°)	Emission (kg h⁻¹)[5]	Uncertainty (kg h⁻¹)[5]	Quality[6]
74	ang20221103t153837				0.0	50.0	
74	GAO20210813t153316p0000	B	39.895032	-80.584188	912.0	19.0	pass
75	ang20221024t181205	B	39.844174	-80.250347	463.0	184.0	pass
75	ang20221009t183505	B	39.843955	-80.250696	1046.0	149.0	pass
75	GAO20210521t150211p0000				0.0	50.0	
75	GAO20210515t141643p0000				0.0	50.0	
75	GAO20210513t153658p0000				0.0	50.0	
76	ang20221024t182326				0.0	50.0	
76	ang20221024t181205				0.0	50.0	
76	ang20221009t184703				0.0	50.0	
76	ang20221009t183505				0.0	50.0	
76	GAO20210813t142433p0000				0.0	50.0	
76	GAO20210521t144353p0000				0.0	50.0	
76	GAO20210515t140819p0000	A	39.815819	-80.283478	223.0	75.0	hide
76	GAO20210513t152129p0000	9	39.8154	-80.2837	314.0	34.0	pass
76	GAO20210513t150800p0000	A	39.815365	-80.283782	248.0	101.0	pass
77	ang20221024t180037	A	39.827331	-80.235712	482.0	81.0	pass
77	ang20221009t182331	D	39.827344	-80.23566	1441.0	355.0	pass
77	GAO20210531t123731p0000						
77	GAO20210521t151830p0000						

Unit ID	Scene ID[1]	Plume[2]	Latitude[3] (°)	Longitude[4] (°)	Emission (kg h^{-1})[5]	Uncertainty (kg h^{-1})[5]	Quality[6]
77	GAO20210521t150211p0000	5	39.827355	-80.235697	1229.0	119.0	pass
77	GAO20210515t142544p0000						
77	GAO20210515t141643p0000	4	39.827725	-80.236354	732.0	324.0	pass
77	GAO20210514t125900p0000						
77	GAO20210513t153658p0000	7	39.827366	-80.236207	1652.0	686.0	pass
78	GAO20210521t144353p0000				0.0	50.0	
78	GAO20210515t140819p0000				0.0	50.0	
78	GAO20210513t152129p0000				0.0	50.0	
80	ang20221103t161828				0.0	50.0	
80	GAO20210521t142744p0000				0.0	50.0	
80	GAO20210521t140904p0000				0.0	50.0	
80	GAO20210515t135940p0000	4	40.0302	-80.3255	314.0	113.0	pass
80	GAO20210515t135117p0000	A	40.030115	-80.325588	202.0	28.0	hide
80	GAO20210513t150800p0000						
80	GAO20210513t145258p0000						
81	ang20221103t161828				0.0	50.0	
81	ang20221103t160514				0.0	50.0	
81	GAO20210521t142744p0000	3	40.0235	-80.3199	523.0	290.0	pass
81	GAO20210521t140904p0000	A	40.023446	-80.319963	537.0	125.0	pass
81	GAO20210515t135940p0000	3	40.0235	-80.3199	248.0	47.0	pass

Continued on next page

Unit ID	Scene ID[1]	Plume[2]	Latitude[3] (°)	Longitude[4] (°)	Emission (kg h⁻¹)[5]	Uncertainty (kg h⁻¹)[5]	Quality[6]
81	GAO20210513t150800p0000	4	40.0234	-80.32	433.0	219.0	pass
81	GAO20210513t145258p0000	4	40.023348	-80.320088	997.0	672.0	hide
82	ang20221103t160514				0.0	50.0	
82	GAO20210521t142744p0000	4	39.97341	-80.325521	1306.0	893.0	hide
82	GAO20210521t140904p0000	2	39.9735	-80.3252	1629.0	532.0	pass
82	GAO20210515t135940p0000						
82	GAO20210515t135117p0000	2	39.9735	-80.3254	589.0	212.0	pass
82	GAO20210513t150800p0000	5	39.973272	-80.324468	960.0	319.0	hide
82	GAO20210513t145258p0000	5	39.973745	-80.325062	1397.0	711.0	hide
87	ang20221024t181205				0.0	50.0	
87	ang20221009t183505				0.0	50.0	
87	GAO20210521t150211p0000	3	39.838635	-80.258797	1066.0	106.0	pass
87	GAO20210521t144353p0000				0.0	50.0	
87	GAO20210515t141643p0000	2	39.8387	-80.2587	191.0	138.0	pass
87	GAO20210515t140819p0000	5	39.8387	-80.2588	197.0	121.0	pass
87	GAO20210513t153658p0000	5	39.8386	-80.2587	1247.0	136.0	pass
87	GAO20210513t152129p0000	8	39.8386	-80.2588	678.0	150.0	pass
88	ang20221024t181205				0.0	50.0	
88	ang20221024t180037				0.0	50.0	
88	ang20221009t183505				0.0	50.0	

Unit ID	Scene ID[1]	Plume[2]	Latitude[3] (°)	Longitude[4] (°)	Emission (kg h^{-1})[5]	Uncertainty (kg h^{-1})[5]	Quality[6]
88	ang202210009t182331				0.0	50.0	
88	GAO20210521t150211p0000	4	39.833868	-80.246494	537.0	181.0	pass
88	GAO20210515t141643p0000	3	39.8339	-80.2465	467.0	446.0	pass
88	GAO20210513t153658p0000	6	39.833708	-80.246692	638.0	339.0	pass
89	ang202210024t173730	B	39.829573	-80.165832	244.0	80.0	pass
89	ang202210009t180013				0.0	50.0	
89	GAO20210521t155242p0000				0.0	50.0	
89	GAO20210515t144158p0000	1	39.8295	-80.1658	293.0	79.0	pass
89	GAO20210514t132657p0000	2	39.8295	-80.1666	269.0	151.0	pass
90	ang202211103t155207				0.0	50.0	
90	ang202210024t183453				0.0	50.0	
90	ang202210009t185838				0.0	50.0	
90	GAO20210813t151207p0000				0.0	50.0	
90	GAO20210521t135234p0000	4	39.746431	-80.359643	945.0	204.0	pass
90	GAO20210515t134113p0000	3	39.745543	-80.36067	565.0	77.0	pass
92	ang202210024t174902				0.0	50.0	
92	ang202210009t181144				0.0	50.0	
92	GAO20210813t141544p0000				0.0	50.0	
92	GAO20210813t140412p0000				0.0	50.0	
92	GAO20210521t151830p0000	3	39.7728	-80.2184	750.0	72.0	pass

Unit ID	Scene ID[1]	Plume[2]	Latitude[3] (°)	Longitude[4] (°)	Emission (kg h^{-1})[5]	Uncertainty (kg h^{-1})[5]	Quality[6]
94	ang20221024t182326	F	39.847678	-80.267888	700.0	252.0	pass
94	ang20221024t181205	A	39.847733	-80.267888	768.0	103.0	pass
94	ang20221009t184703	E	39.8477	-80.2677	761.0	278.0	pass
94	ang20221009t183505	C	39.847728	-80.267528	1396.0	303.0	pass
94	GAO20210521t144353p0000				0.0	50.0	
94	GAO20210515t140819p0000				0.0	50.0	
94	GAO20210513t152129p0000				0.0	50.0	
95	ang20221024t182326						
95	ang20221024t181205				0.0	50.0	
95	ang20221009t184703				0.0	50.0	
95	ang20221009t183505				0.0	50.0	
95	GAO20210521t144353p0000						
95	GAO20210515t140819p0000	4	39.8392	-80.2712	185.0	108.0	pass
95	GAO20210513t152129p0000						
96	ang20221024t182326				0.0	50.0	
96	ang20221024t181205				0.0	50.0	
96	ang20221009t184703				0.0	50.0	
96	ang20221009t183505				0.0	50.0	
96	GAO20210521t144353p0000						
96	GAO20210515t140819p0000	B	39.840947	-80.26969	218.0	92.0	pass

Unit ID	Scene ID[1]	Plume[2]	Latitude[3] (°)	Longitude[4] (°)	Emission (kg h^{-1})[5]	Uncertainty (kg h^{-1})[5]	Quality[6]
96	GAO20210513t152129p0000	7	39.841024	-80.269698	876.0	533.0	pass
97	ang20221103t163129				0.0	50.0	
97	ang20221103t153837	T	39.857731	-80.427415	147.0	45.0	pass
97	ang20221003t160932	E	39.857658	-80.427837	907.0	308.0	pass
97	GAO20210813t143918p0000				0.0	50.0	
97	GAO20210521t131640p0000				0.0	50.0	
97	GAO20210515t132309p0000				0.0	50.0	
97	GAO20210513t141020p0000				0.0	50.0	
98	ang20221103t155207				0.0	50.0	
98	ang20221024t183453						
98	ang20221024t182326	H	39.999953	-80.227215	658.0	99.0	pass
98	ang20221009t184703	C	39.999997	-80.227007	1194.0	363.0	pass
98	GAO20210521t151830p0000				0.0	50.0	
98	GAO20210515t142544p0000				0.0	50.0	
98	GAO20210514t125900p0000				0.0	50.0	
98	GAO20210513t155053p0000				0.0	50.0	
99	ang20221103t155207	I	39.957238	-80.275665	186.0	32.0	pass
99	ang20221024t183453	A	39.9571	-80.2757	702.0	211.0	pass
99	ang20221009t185838				0.0	50.0	
99	GAO20210521t144353p0000				0.0	50.0	

Unit ID	Scene ID[1]	Plume[2]	Latitude[3] (°)	Longitude[4] (°)	Emission (kg h^{-1})[5]	Uncertainty (kg h^{-1})[5]	Quality[6]
99	GAO20210515t140819p0000				0.0	50.0	
99	GAO20210513t152129p0000				0.0	50.0	
100	ang20221103t155207	G	39.953147	-80.263436	260.0	70.0	pass
100	ang20221024t183453	B	39.953216	-80.263359	366.0	115.0	pass
100	ang20221009t185838	D	39.952989	-80.263446	963.0	221.0	pass
100	GAO20210521t150211p0000				0.0	50.0	
100	GAO20210521t144353p0000				0.0	50.0	
100	GAO20210515t141643p0000				0.0	50.0	
100	GAO20210515t140819p0000				0.0	50.0	
100	GAO20210513t153658p0000				0.0	50.0	
100	GAO20210513t152129p0000				0.0	50.0	
101	ang20221103t161828	G	39.84819	-80.415845	461.0	184.0	pass
101	ang20221103t153837	R	39.848172	-80.416757	487.0	190.0	pass
101	ang20221003t160932						
101	GAO20210813t143918p0000				0.0	50.0	
101	GAO20210521t131640p0000				0.0	50.0	
101	GAO20210515t132309p0000				0.0	50.0	
101	GAO20210513t141020p0000				0.0	50.0	
102	ang20221103t161828	D	39.851634	-80.408745	314.0	95.0	pass
102	ang20221103t153837	O	39.8517	-80.4088	336.0	38.0	pass

95

Unit ID	Scene ID[1]	Plume[2]	Latitude[3] (°)	Longitude[4] (°)	Emission (kg h^{-1})[5]	Uncertainty (kg h^{-1})[5]	Quality[6]
102	ang202211003t160932	G	39.851682	-80.408706	1416.0	230.0	pass
102	GAO20210813t143918p0000				0.0	50.0	
102	GAO20210521t131640p0000				0.0	50.0	
102	GAO20210515t132309p0000				0.0	50.0	
102	GAO20210513t141020p0000				0.0	50.0	
105	ang202211103t155207	K	39.958354	-80.26284	336.0	57.0	pass
105	ang202211024t183453	G	39.958339	-80.262987	183.0	51.0	pass
105	ang202211009t185838	B	39.958324	-80.262918	1048.0	393.0	pass
105	GAO20210521t150211p0000				0.0	50.0	
105	GAO20210521t144353p0000				0.0	50.0	
105	GAO20210515t141643p0000				0.0	50.0	
105	GAO20210515t140819p0000				0.0	50.0	
105	GAO20210513t153658p0000				0.0	50.0	
105	GAO20210513t152129p0000				0.0	50.0	
108	ang202211103t160514				0.0	50.0	
108	GAO20210521t142744p0000				0.0	50.0	
108	GAO20210515t135940p0000				0.0	50.0	
108	GAO20210513t150800p0000				0.0	50.0	
113	GAO20220923t174201p0000	B	33.5106	-87.2877	282.0	125.0	hide
113	GAO20220923t173123p0000	B	33.510618	-87.287549	277.0	134.0	hide

Continued on next page

96

Unit ID	Scene ID[1]	Plume[2]	Latitude[3] (°)	Longitude[4] (°)	Emission (kg h⁻¹)[5]	Uncertainty (kg h⁻¹)[5]	Quality[6]
113	GAO20220428t164817p0000	A	33.510686	-87.287732	734.0	161.0	pass
113	GAO20220428t164102p0000	A	33.5107	-87.2876	478.0	169.0	hide
113	GAO20220422t164212p0000	B	33.51065	-87.287628	448.0	190.0	pass
113	GAO20220422t162854p0000	A	33.510622	-87.287687	370.0	197.0	hide
113	GAO20220419t170408p0000	A	33.510758	-87.287721	698.0	126.0	pass
113	GAO20220419t165329p0000	B	33.510588	-87.287615	415.0	78.0	hide
114	GAO20220923t162942p0000				0.0	50.0	
114	GAO20220428t154635p0000	A	33.486778	-87.094031	653.0	310.0	pass
114	GAO20220422t150848p0000	A	33.486647	-87.094427	932.0	190.0	pass
114	GAO20220419t152826p0000	A	33.486635	-87.094305	2008.0	1632.0	hide
115	GAO20220923t164450p0000	B	33.453576	-87.138962	963.0	669.0	pass
115	GAO20220923t163623p0000						
115	GAO20220428t160140p0000				0.0	50.0	
115	GAO20220428t155431p0000						
115	GAO20220422t153007p0000				0.0	50.0	
115	GAO20220419t155053p0000				0.0	50.0	
115	GAO20220419t154146p0000				0.0	50.0	
118	GAO20220923t165226p0000				0.0	50.0	
118	GAO20220923t164450p0000				0.0	50.0	
118	GAO20220428t160924p0000				0.0	50.0	

Unit ID	Scene ID[1]	Plume[2]	Latitude[3] (°)	Longitude[4] (°)	Emission (kg h^{-1})[5]	Uncertainty (kg h^{-1})[5]	Quality[6]
118	GAO20220428t160140p0000				0.0	50.0	
118	GAO20220423t172858p0000				0.0	50.0	
118	GAO20220422t154027p0000				0.0	50.0	
118	GAO20220422t153007p0000				0.0	50.0	
118	GAO20220419t160705p0000				0.0	50.0	
118	GAO20220419t155053p0000				0.0	50.0	
118	GAO20220923t164450p0000				0.0	50.0	
119	GAO20220923t163623p0000						
119	GAO20220428t160140p0000				0.0	50.0	
119	GAO20220422t153007p0000	C	33.4406	-87.1401	1009.0	239.0	pass
119	GAO20220419t155053p0000				0.0	50.0	
119	GAO20220419t154146p0000						
120	GAO20220923t170108p0000	A	33.403069	-87.199343	2250.0	1228.0	pass
120	GAO20220428t161644p0000	A	33.403089	-87.199106	1122.0	380.0	pass
120	GAO20220423t173858p0000	A	33.403175	-87.199424	2043.0	1305.0	pass
120	GAO20220422t155137p0000	A	33.4032	-87.199193	2155.0	463.0	pass
120	GAO20220419t161635p0000	A	33.402986	-87.199224	2536.0	1393.0	pass
121	GAO20220923t172122p0000	B	33.421547	-87.239888	1453.0	687.0	pass
121	GAO20220923t171045p0000	B	33.421448	-87.239739	2549.0	1144.0	pass
121	GAO20220428t163239p0000	A	33.421375	-87.239944	1508.0	338.0	pass

98

Unit ID	Scene ID[1]	Plume[2]	Latitude[3] (°)	Longitude[4] (°)	Emission (kg h^{-1})[5]	Uncertainty (kg h^{-1})[5]	Quality[6]
121	GAO20220428t162445p0000	C	33.421522	-87.239706	1330.0	281.0	pass
121	GAO20220422t161650p0000	A	33.421531	-87.239826	1145.0	184.0	pass
121	GAO20220422t160323p0000	B	33.42154	-87.239717	974.0	161.0	hide
121	GAO20220419t163855p0000	A	33.421041	-87.239701	1645.0	944.0	pass
121	GAO20220419t162841p0000	A	33.4214	-87.2399	1297.0	425.0	pass
122	GAO20220923t172122p0000	A	33.3781	-87.2331	1409.0	762.0	pass
122	GAO20220923t171045p0000	C	33.378133	-87.233107	1346.0	752.0	pass
122	GAO20220428t162445p0000	A	33.378102	-87.23301	1261.0	545.0	pass
122	GAO20220422t161650p0000	B	33.378245	-87.23292	2970.0	674.0	pass
122	GAO20220422t160323p0000	A	33.378224	-87.233155	2160.0	1118.0	pass
122	GAO20220419t162841p0000	B	33.378026	-87.232962	2425.0	2104.0	pass
123	GAO20220923t171045p0000	A	33.37042	-87.218198	1097.0	635.0	hide
123	GAO20220428t162445p0000	B	33.370368	-87.21825	588.0	126.0	pass
123	GAO20220422t160323p0000				0.0	50.0	
123	GAO20220419t162841p0000				0.0	50.0	
124	GAO20220923t172122p0000				0.0	50.0	
124	GAO20220428t163239p0000	E	33.376974	-87.251949	573.0	109.0	pass
124	GAO20220422t161650p0000				0.0	50.0	
124	GAO20220419t163855p0000	C	33.3769	-87.2519	328.0	66.0	pass
125	GAO20220923t173123p0000	A	33.39427	-87.26538	734.0	287.0	pass

Unit ID	Scene ID[1]	Plume[2]	Latitude[3] (°)	Longitude[4] (°)	Emission (kg h⁻¹)[5]	Uncertainty (kg h⁻¹)[5]	Quality[6]
125	GAO20220923t172122p0000	D	33.394237	-87.265574	1215.0	684.0	hide
125	GAO20220428t164102p0000	B	33.394217	-87.265468	953.0	220.0	pass
125	GAO20220428t163239p0000	B	33.394408	-87.265568	765.0	276.0	pass
125	GAO20220422t162854p0000	B	33.394383	-87.265558	1647.0	396.0	pass
125	GAO20220422t161650p0000	C	33.394296	-87.265518	1240.0	466.0	hide
125	GAO20220419t165329p0000	A	33.394182	-87.265674	1617.0	848.0	pass
125	GAO20220419t163855p0000	B	33.394264	-87.265529	1226.0	471.0	pass
126	GAO20220923t175137p0000	A	33.366291	-87.335066	333.0	118.0	pass
126	GAO20220428t165558p0000	C	33.366042	-87.335058	981.0	150.0	pass
126	GAO20220422t165446p0000	D	33.366034	-87.335054	957.0	154.0	pass
126	GAO20220419t171816p0000	E	33.366351	-87.335051	354.0	102.0	pass
127	GAO20220923t180207p0000	A	33.407722	-87.336393	2636.0	941.0	hide
127	GAO20220923t175137p0000	B	33.407725	-87.336394	3130.0	1173.0	pass
127	GAO20220428t165558p0000	A	33.407757	-87.336679	1720.0	389.0	pass
127	GAO20220422t170740p0000	A	33.407885	-87.336495	1424.0	388.0	pass
127	GAO20220422t165446p0000	B	33.407979	-87.336632	1625.0	312.0	pass
127	GAO20220419t171816p0000	B	33.407845	-87.336542	2326.0	958.0	pass
131	GAO20220923t175137p0000				0.0	50.0	
131	GAO20220428t165558p0000				0.0	50.0	
131	GAO20220422t165446p0000				0.0	50.0	

Continued on next page

100

Unit ID	Scene ID[1]	Plume[2]	Latitude[3] (°)	Longitude[4] (°)	Emission (kg h^{-1})[5]	Uncertainty (kg h^{-1})[5]	Quality[6]
131	GAO20220419t171816p0000				0.0	50.0	
132	GAO20220923t172122p0000	C	33.321798	-87.242005	225.0	105.0	pass
132	GAO20220428t163239p0000	F	33.321773	-87.24205	186.0	34.0	pass
132	GAO20220428t162445p0000				0.0	50.0	
132	GAO20220422t161650p0000				0.0	50.0	
132	GAO20220419t163855p0000				0.0	50.0	
133	GAO20220923t174201p0000				0.0	50.0	
133	GAO20220428t164817p0000				0.0	50.0	
133	GAO20220422t164212p0000				0.0	50.0	
133	GAO20220419t170408p0000				0.0	50.0	
135	GAO20220923t175137p0000				0.0	50.0	
135	GAO20220428t165558p0000				0.0	50.0	
135	GAO20220422t165446p0000				0.0	50.0	
135	GAO20220419t171816p0000				0.0	50.0	
137	GAO20220923t181220p0000				0.0	50.0	
137	GAO20220428t171036p0000				0.0	50.0	
137	GAO20220422t171936p0000				0.0	50.0	
137	GAO20220419t174335p0000				0.0	50.0	
140	GAO20220923t181220p0000				0.0	50.0	
140	GAO20220428t171036p0000				0.0	50.0	

Unit ID	Scene ID[1]	Plume[2]	Latitude[3] (°)	Longitude[4] (°)	Emission (kg h⁻¹)[5]	Uncertainty (kg h⁻¹)[5]	Quality[6]
140	GAO20220422t171936p0000					0.0	50.0
140	GAO20220419t174335p0000					0.0	50.0
142	GAO20220923t180207p0000					0.0	50.0
142	GAO20220923t175137p0000					0.0	50.0
142	GAO20220428t170258p0000					0.0	50.0
142	GAO20220428t165558p0000					0.0	50.0
142	GAO20220422t170740p0000					0.0	50.0
142	GAO20220422t165446p0000					0.0	50.0
142	GAO20220419t172848p0000					0.0	50.0
142	GAO20220419t171816p0000					0.0	50.0
144	GAO20220923t173123p0000					0.0	50.0
144	GAO20220428t164102p0000					0.0	50.0
144	GAO20220422t162854p0000					0.0	50.0
144	GAO20220419t165329p0000					0.0	50.0
145	GAO20220923t164450p0000					0.0	50.0
145	GAO20220428t160140p0000	A	33.481502	-87.141448	330.0	128.0	pass
145	GAO20220422t153007p0000					0.0	50.0
145	GAO20220419t155053p0000					0.0	50.0
146	GAO20220923t163623p0000						
146	GAO20220923t162942p0000					0.0	50.0

Unit ID	Scene ID[1]	Plume[2]	Latitude[3] (°)	Longitude[4] (°)	Emission (kg h^{-1})[5]	Uncertainty (kg h^{-1})[5]	Quality[6]
146	GAO20220428t154635p0000					50.0	
146	GAO20220422t151917p0000				0.0	50.0	
146	GAO20220422t150848p0000				0.0	50.0	
146	GAO20220419t152826p0000				0.0	50.0	
147	GAO20220923t162942p0000				0.0	50.0	
147	GAO20220428t154635p0000				0.0	50.0	
147	GAO20220422t151917p0000						
147	GAO20220422t150848p0000				0.0	50.0	
147	GAO20220419t152826p0000				0.0	50.0	
148	GAO20220923t162942p0000				0.0	50.0	
148	GAO20220428t154635p0000				0.0	50.0	
148	GAO20220422t150848p0000				0.0	50.0	
148	GAO20220419t152826p0000				0.0	50.0	
149	GAO20220923t164450p0000				0.0	50.0	
149	GAO20220923t163623p0000				0.0	50.0	
149	GAO20220428t160140p0000				0.0	50.0	
149	GAO20220428t155431p0000				0.0	50.0	
149	GAO20220422t153007p0000				0.0	50.0	
149	GAO20220422t151917p0000				0.0	50.0	
149	GAO20220419t155053p0000				0.0	50.0	

Unit ID	Scene ID[1]	Plume[2]	Latitude[3] (°)	Longitude[4] (°)	Emission (kg h^{-1})[5]	Uncertainty (kg h^{-1})[5]	Quality[6]
149	GAO20220419t154146p0000				0.0	50.0	
151	GAO20220923t163623p0000				0.0	50.0	
151	GAO20220923t162942p0000				0.0	50.0	
151	GAO20220428t155431p0000				0.0	50.0	
151	GAO20220428t154635p0000				0.0	50.0	
151	GAO20220422t151917p0000				0.0	50.0	
151	GAO20220422t150848p0000				0.0	50.0	
151	GAO20220419t154146p0000						
151	GAO20220419t152826p0000				0.0	50.0	
152	GAO20220923t163623p0000				0.0	50.0	
152	GAO20220923t162942p0000				0.0	50.0	
152	GAO20220428t155431p0000				0.0	50.0	
152	GAO20220428t154635p0000				0.0	50.0	
152	GAO20220422t151917p0000				0.0	50.0	
152	GAO20220422t150848p0000				0.0	50.0	
152	GAO20220419t154146p0000				0.0	50.0	
152	GAO20220419t152826p0000				0.0	50.0	
153	GAO20220923t163623p0000				0.0	50.0	
153	GAO20220923t162942p0000				0.0	50.0	
153	GAO20220428t155431p0000				0.0	50.0	

Unit ID	Scene ID[1]	Plume[2]	Latitude[3] (°)	Longitude[4] (°)	Emission (kg h^{-1})[5]	Uncertainty (kg h^{-1})[5]	Quality[6]
153	GAO20220428t154635p0000				0.0	50.0	
153	GAO20220422t151917p0000				0.0	50.0	
153	GAO20220422t150848p0000				0.0	50.0	
153	GAO20220419t154146p0000						
153	GAO20220419t152826p0000				0.0	50.0	
154	GAO20220923t165226p0000				0.0	50.0	
154	GAO20220923t164450p0000				0.0	50.0	
154	GAO20220428t160924p0000				0.0	50.0	
154	GAO20220428t160140p0000				0.0	50.0	
154	GAO20220423t172858p0000				0.0	50.0	
154	GAO20220422t154027p0000				0.0	50.0	
154	GAO20220419t160705p0000				0.0	50.0	
154	GAO20220419t155053p0000				0.0	50.0	
155	GAO20220923t165226p0000				0.0	50.0	
155	GAO20220428t160924p0000				0.0	50.0	
155	GAO20220423t172858p0000				0.0	50.0	
155	GAO20220422t154027p0000				0.0	50.0	
155	GAO20220419t160705p0000				0.0	50.0	
156	GAO20220923t164450p0000				0.0	50.0	
156	GAO20220428t160140p0000				0.0	50.0	

Unit ID	Scene ID[1]	Plume[2]	Latitude[3] (°)	Longitude[4] (°)	Emission (kg h⁻¹)[5]	Uncertainty (kg h⁻¹)[5]	Quality[6]
156	GAO20220422t153007p0000					50.0	
156	GAO20220419t155053p0000					50.0	
157	GAO20220923t164450p0000	A	33.457	-87.1418	1063.0	708.0	hide
157	GAO20220428t160140p0000				0.0	50.0	
157	GAO20220422t153007p0000				0.0	50.0	
157	GAO20220419t155053p0000				0.0	50.0	
158	GAO20220923t164450p0000	C	33.457357	-87.140998	736.0	610.0	pass
158	GAO20220428t160140p0000				0.0	50.0	
158	GAO20220422t153007p0000				0.0	50.0	
158	GAO20220419t155053p0000				0.0	50.0	
159	GAO20220923t164450p0000				0.0	50.0	
159	GAO20220923t163623p0000				0.0	50.0	
159	GAO20220428t160140p0000				0.0	50.0	
159	GAO20220428t155431p0000				0.0	50.0	
159	GAO20220422t153007p0000				0.0	50.0	
159	GAO20220422t151917p0000						
159	GAO20220419t155053p0000				0.0	50.0	
159	GAO20220419t154146p0000				0.0	50.0	
161	GAO20220923t174201p0000	A	33.54414	-87.308289	825.0	244.0	pass
161	GAO20220428t164817p0000				0.0	50.0	

Continued on next page

106

Unit ID	Scene ID[1]	Plume[2]	Latitude[3] (°)	Longitude[4] (°)	Emission (kg h⁻¹)[5]	Uncertainty (kg h⁻¹)[5]	Quality[6]
161	GAO20220422t165446p0000	A	33.54399	-87.308298	999.0	202.0	pass
161	GAO20220422t164212p0000	A	33.543988	-87.308238	846.0	230.0	pass
161	GAO20220419t170408p0000				0.0	50.0	
162	GAO20220923t175137p0000				0.0	50.0	
162	GAO20220428t165558p0000				0.0	50.0	
162	GAO20220422t170740p0000				0.0	50.0	
162	GAO20220422t165446p0000				0.0	50.0	
162	GAO20220419t171816p0000				0.0	50.0	
189	ang20221014t183849	A	37.250679	-81.89834	1907.0	378.0	hide
189	ang20221014t182827	A	37.25064	-81.898263	1693.0	937.0	hide
189	ang20221014t182827	B	37.250533	-81.898305	1637.0	813.0	pass
190	ang20221014t185154	B	37.233743	-81.850938	7576.0	1120.0	pass
190	ang20220929t194238	A	37.23381	-81.850894	10061.0	3736.0	hide
191	ang20220929t175528	B	37.175002	-81.927865	3550.0	485.0	hide
192	ang20220929t175528	A	37.174294	-81.879163	4785.0	1409.0	pass
193	ang20221014t185154				0.0	50.0	
193	ang20220929t194238				0.0	50.0	
195	ang20220929t182318				0.0	50.0	
195	ang20220929t175528				0.0	50.0	
196	ang20221014t185154				0.0	50.0	

Unit ID	Scene ID[1]	Plume[2]	Latitude[3] (°)	Longitude[4] (°)	Emission (kg h⁻¹)[5]	Uncertainty (kg h⁻¹)[5]	Quality[6]
196	ang20220929t194238					50.0	
196	ang20220929t180755					50.0	
198	ang20220929t174215					50.0	
200	ang20221014t165055	A	37.551402	-82.410826	1538.0	625.0	pass
200	ang20221014t164433					50.0	
204	GAO20221020t202758p0000	A	38.880552	-107.462574	1417.0	246.0	pass
204	GAO20221019t205436p0000	A	38.88061	-107.462533	746.0	357.0	pass
204	GAO20221018t203814p0000	A	38.880605	-107.462572	1082.0	338.0	pass
204	GAO20200805t170114p0000	A	38.880634	-107.462604	1628.0	688.0	pass
204	GAO20200731t183752p0000	A	38.880611	-107.462613	1817.0	755.0	pass
205	GAO20200731t174219p0000	A	39.6827	-110.5453	459.0	23.0	pass
207	ang20220502t170537	A	36.792583	-108.388953	1031.0	98.0	pass
207	ang20220501t163231	A	36.792667	-108.389029	3210.0	2153.0	pass
207	ang20220325t173925	A	36.793308	-108.389105	1105.0	472.0	pass
207	ang20220325t172449	A	36.792941	-108.389076	523.0	218.0	hide
207	ang20220323t190401	A	36.792945	-108.388937	853.0	152.0	pass
207	ang20220323t184723	A	36.792961	-108.389035	836.0	162.0	pass
207	GAO20200804t171401p0000	A	36.792565	-108.388968	592.0	330.0	pass
207	ang20190621t195346				0.0	50.0	
207	ang20150420t181345				0.0	50.0	

108

Unit ID	Scene ID[1]	Plume[2]	Latitude[3] (°)	Longitude[4] (°)	Emission (kg h^{-1})[5]	Uncertainty (kg h^{-1})[5]	Quality[6]
210	ang20221016t172356				0.0	50.0	
210	ang20221011t160929				0.0	50.0	
210	ang20221003t155912				0.0	50.0	
211	ang20221024t174902				0.0	50.0	
211	ang20221009t181144				0.0	50.0	
211	GAO20210521t155242p0000				0.0	50.0	
211	GAO20210515t144158p0000	A	39.878195	-80.170593	601.0	265.0	pass
211	GAO20210514t132657p0000	1	39.8782	-80.1707	151.0	99.0	pass

---

[1]Scene ID in Carbon Mapper's data portal (https://data.carbonmapper.org/). Each scene ID corresponds to a single aircraft track.

[2]Plume label used in Carbon Mapper's data portal. A full Plume ID is the scene ID followed by a plume label, e.g. GAO20210515t144158p0000-A.

[3]Latitude of plume origin.

[4]Longitude of plume origin.

[5]Emission rate and uncertainty are calculated for this paper following the updated approach used for EMIT in Ayasse et al. (2024) adapted for aircraft data, and are not the same as the emission rates in the Carbon Mapper portal.

[6]"Pass" indicates a plume meets Carbon Mapper's quality control requirements (Cusworth et al., 2025). "Hide" indicates plume did not meet Carbon Mapper's quality control requirements and is excluded from analysis.